Search for diboson resonance production at $\sqrt{s} = 8$ TeV with the ATLAS detector

Stephen Marsden
Particle Physics Group
School of Physics and Astronomy

A thesis submitted to the University of Manchester
for the degree of Doctor of Philosophy
in the Faculty of Engineering and Physical Sciences

2015

Contents

Word count: 36,072

List of Figures

List of Tables

Abstract

A search for heavy exotic diboson resonances decaying to $\ell\ell qq$ final states is presented using pp collision data collected with the ATLAS detector at the Large Hadron Collider. The analysis uses a data sample corresponding to an integrated luminosity of 20.3 fb^{-1} at $\sqrt{s} = 8$ TeV collected between April and December 2012. No significant excess of data events over the predicted Standard Model background is observed and 95% confidence level upper limits are set on the product of the production cross-section and the branching ratio for spin-2 Kaluza-Klein gravitons predicted by the bulk Randall-Sundrum model and for Extended Gauge Model W' bosons. These results are subsequently combined with limits obtained from searches using the $\ell\nu\ell'\ell'$, $\ell\nu qq$ and $qqqq$ final states, and new mass limits are set on both signal models.

Declaration

No portion of the work referred to in the thesis has been submitted in support of an application for another degree or qualification of this or any other university or other institute of learning.

Copyright

Acknowledgements

I wish to thank the entirety of the Particle Physics Group at The University of Manchester. In particular Alex Oh and Stefan Söldner-Rembold for their supervision and guidance through my PhD. Thanks to Fred Loebinger, whose uncontrollable enthusiasm for physics convinced me to study in Manchester, and to Terry Wyatt, whose supervision during my masters year lead me to particle physics.

To all the physicists ATLAS comprises, thank you for sharing expertise and maintaining my motivation. In particular thanks to the many people I collaborated with directly, whose hard work made these analyses possible. Thank you to all the people that were there at the start of my study for getting me going and helping the annoying first year who didn't know where to start.

To Heather, whose love, and ability to provide pizza at a moment's notice, helped me through the challenges of the past few years.

Finally, a special thanks to my family. To my father, Brian, for proof reading and helping me with all the tedious things. To my mother, Mandy, who even though she moved away was still there to offer support and advice whenever is was needed. To my grandparents, who despite not understanding what I do, were always eager to help. I would not be where I am today without the love and support they have provided.

Preface

From 2011 to present the author has been a member of the High Energy Physics Group at The University of Manchester, and a member of The ATLAS Collaboration. During this time the author contributed to the development and validation of electron triggers applied to the Inner Detector and worked on a number of exotic analyses specialising on the implementation of the statistical interpretation.

A search for resonant $ZZ \to \ell\ell qq$ was performed using a partial 8 TeV dataset collected by the ATLAS detector. The results of this analysis were published in the form of a conference note [1].

A larger updated dataset was used to perform a similar analysis in the $\ell\ell qq$ channel, searching for resonant ZZ and WZ production. The results of this analysis were published in The European Physical Journal C [2]. This analysis is described in detail in section 5.

A combination of this latter analysis was performed with similar searches in the $qqqq$, $\ell\nu qq$ and $\ell\nu\ell'\ell'$ final states using the same dataset. Preliminary results of this combination were published in a conference note [3], and updated results are due to be submitted to a peer reviewed journal in the immediate future. Details of this combination are given in section 6.

1

Introduction

The Standard Model of particle physics is incomplete, and many possible extensions to the model predict the existence of new particles. This thesis describes the search for both charged and neutral resonances at the TeV scale that decay into vector boson pairs. The large resonance masses probed result in highly boosted topologies, and new boson tagging techniques are employed. The dataset used for the analyses presented here corresponds to an integrated luminosity of 20.3 fb^{-1} and was collected using the ATLAS detector at the Large Hadron Collider at a centre of mass energy of $\sqrt{s} = 8$ TeV.

The contents of this thesis are arranged in the following manner. Section 2 presents a brief overview of the Standard Model and of the exotic extensions that are used as benchmark models. The designs of the Large Hadron Collider and the ATLAS detector are described in section 3. Section 4 describes the reconstruction of signals recorded by the detector into physics objects used in the analyses. The search performed for resonant $VZ \to \ell\ell qq$ production, where V represents either a W or Z boson, is presented in detail in section 5. Similar diboson resonance searches were performed by the ATLAS collaboration in the $\ell\nu\ell'\ell'$, $\ell\nu qq$ and $qqqq$ final states. The combination of these with the $\ell\ell qq$ analysis is presented in section 6. Finally in section 7 a summary is given of the work contained within

this thesis.

2

The Standard Model and Beyond

2.1 Overview of the Standard Model

The Standard Model (SM) is currently the best framework for modelling the properties and interactions of fundamental particles and is one of the most rigorously tested theories in physics [4]. There are four fundamental forces, electromagnetism (EM), weak interaction, strong interaction and gravitation, of which the SM describes the interactions of the first three.

For the three forces described in the SM, interactions between particles are mediated by integer spin particles (bosons). The photon, γ, is responsible for electromagnetic (EM) interactions, the W and Z bosons mediate the weak force, and gluons, g, mediate the strong force. Particles that constitute matter have half integer spin (fermions). Fermions are subdivided into the categories of quarks and leptons. Quarks interact via the strong, weak and EM forces, whereas leptons only interact via the weak and EM force. Leptons are further subdivided into the electrically charged leptons and the neutral neutrinos. All fermions have associated anti-particles that have the same properties, and have opposite charges. Whether the neutrinos are their own antiparticles has yet to be determined and is a topic of current research. Particles obtain mass through interactions with a

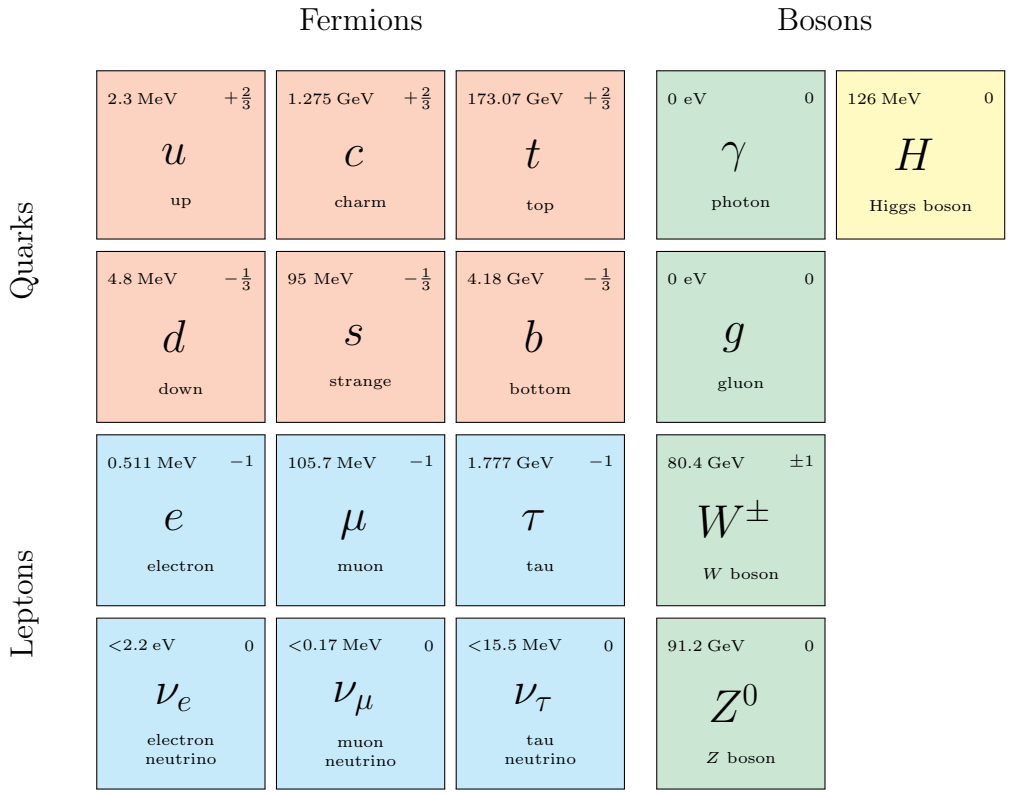

Figure 2.1: The particles of the Standard Model. The mass and electric charge of each particle is given in the top left and right corners of each tile, respectively [4].

spin-0 Higgs field. The particles of the SM are summarised in figure 2.1.

The SM is a Quantum Field Theory (QFT) which is gauge invariant under local transformations defined by the $\mathrm{SU(3)}_c \times \mathrm{SU(2)}_L \times \mathrm{U(1)}_Y$ group [5]. In order to preserve the symmetry under these transformations, spin-1 fields must be introduced to the Lagrangian, which give rise to associated vector bosons. The $\mathrm{SU(3)}_c$ component describes Quantum Chromodynamics (QCD), which is the theory of the strong force and requires eight gluons. The remaining $\mathrm{SU(2)}_L \times \mathrm{U(1)}_Y$ components together describe the electroweak force, and require a total of four vector fields, which give rise to the γ, $W^{\pm}$ and Z boson fields after electroweak symmetry breaking.

2.2 Success and Failure of the Standard Model

The SM has been very successful in describing a wide range of observed phenomena to high precision as shown in figure 2.2. Despite this success, there are a number of known failings that require the introduction of new physics.

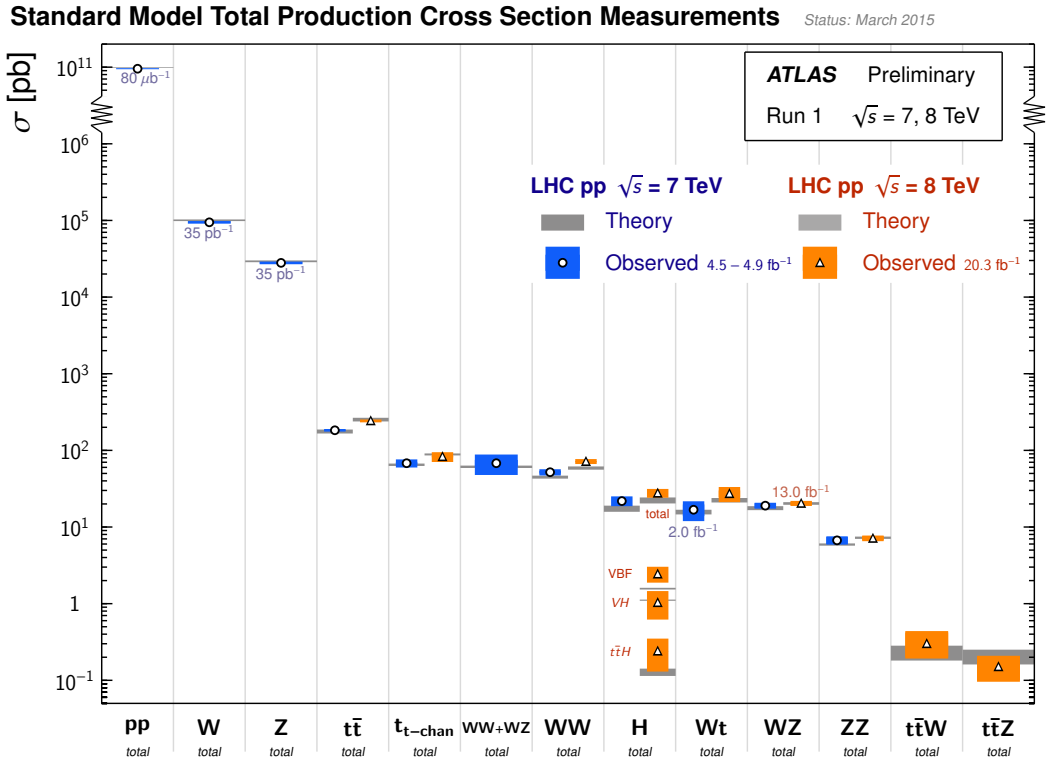

Figure 2.2: A comparison of the production cross-sections measured by the ATLAS collaboration compared with the predictions of the SM [6].

The SM is incapable of describing gravitational interactions. In a vast majority of situations where the SM is applied the masses involved are sufficiently small that the effect of gravity is negligible. In the very early universe, particles had sufficient energy to cause gravity to no longer be negligible. To accurately describe the evolution of the universe under these conditions, a new theory is required.

Cosmological observations have shown that approximately 69% of the universe comprises dark energy, and 26% comprises dark matter, which are absent from

the SM [7]. This matter is assumed to only interact weakly with the known fundamental particles. There are a number of extensions to the SM which introduce new particles that could be dark matter candidates.

An additional question that remains unanswered in the SM is the hierarchy problem. Since the Higgs boson mass is close to the electroweak scale of ≈ 100 GeV, contributions to its mass due to loop corrections from massive particles should lead to the Higgs boson having a mass close to the Planck scale of 10^{18} GeV. One way to resolve this is by fine tuning the coupling parameters of the Higgs boson to the SM particles, such that the contributions which have values close to the Planck scale cancel. The extremely high level of precision required for this cancelling is considered to be unnatural. There are numerous extensions to the SM that introduce new physics at the TeV scale such as SUper SYmmetry (SUSY) [4], which lead to detectable signatures in the Large Hadron Collider (LHC).

2.3 Beyond the Standard Model

There are a large number of proposed extensions to the SM, each potentially having a large number of tunable parameters leading to an extremely large theory space. Searches for new physics are performed using benchmark models, and the results applied to a broad theory parameter space. The benchmark models which are considered here are the bulk Randall-Sundrum (RS) model, and the Extended Gauge Model (EGM).

2.3.1 Bulk Randall-Sundrum Graviton

A possibility for new physics resides in the production of a bulk RS graviton, which is a massless spin-2 boson that mediates gravity [8, 9, 10, 11]. The RS formulation of a graviton introduces a higher dimensional mechanism that offers

a possible solution to the hierarchy problem. The bulk consists of the three observable spacial dimensions, one temporal dimension, and a single extra spacial dimension. The metric for this extra spatial dimension is multiplied by a warp factor which is a rapidly changing function of position in the extra dimension. Subspaces of the bulk consisting of the three observable spacial dimensions and the temporal dimension are referred to as a 3-brane.

The Planck brane is the location in the extra dimension where the massless graviton is localised. In the RS1 model [12], the SM fields are confined to a single 3-brane, called the TeV brane, and are incapable of propagating through the extra dimension. In contrast, the bulk RS model allows the SM fields to propagate through the bulk, and are each localised to a different 3-brane. The relative couplings of the fields are determined by the overlap of the wave functions. By tuning the overlap of the lepton and quark wave functions with the Higgs field, the hierarchical nature of the masses of the three families can be accounted for. In keeping with the nomenclature of the RS1 model, the collection of 3-branes on which the SM fields are localised are often referred to singularly as the TeV brane. In both the RS1 and bulk RS models, the observed large hierarchy is generated due to the separation of the TeV brane and the Planck brane in the presence of the exponential warp factor.

If the extra dimension is warped, the graviton is a bound state, and a Kaluza-Klein (KK) ladder of excited graviton states G^*, would be observed, with the lightest excited state having a mass close to the TeV scale. The geometry of the extra dimensions results in the couplings between the SM fields and the excited graviton states being a factor of 10^{15} stronger than to the ground state graviton, which permits the production and detection of these excitations within the LHC. Since the extra dimension is warped and the positions of the SM fields within the bulk differ, the couplings of excited state gravitons and fermions is heavily suppressed.

The governing parameter of this model is the curvature of the extra dimension, k, divided by the reduced 4-dimensional Planck scale $\bar{M}_{\mathrm{Pl}}$ given by,

$$\bar{M}_{\mathrm{Pl}}^2 = \frac{M_5^2}{k}\left(1 - e^{-2kr_c\pi}\right), \tag{2.1}$$

where M_5 is the 5-dimensional Planck scale. The product of the energy scale of the theory, k, and the radius of curvature of the extra dimension, r_c, is ≈ 11. The suppression of the couplings of the excited gravitons to fermions increases with $k/\bar{M}_{\mathrm{Pl}}$. For this reason searches including leptonic final states typically concentrate on the scenario $k/\bar{M}_{\mathrm{Pl}} \approx 0.1$, whereas gauge boson final states are sensitive to $k/\bar{M}_{\mathrm{Pl}} \approx 1$. This case is considered within the analyses presented in this thesis.

As the couplings between the graviton and fermions are suppressed, and gluon distribution functions dominate over quark distribution functions at the LHC, the dominant production channel for this model is gluon-gluon fusion. The large coupling to gauge bosons leads to the $G^* \to WW$ and $G^* \to ZZ$ decay channels being dominant, as shown in figure 2.3. For excited graviton states with masses between 0.5 TeV and 2.5 TeV, the resonance width ranges from 3.7% to 6.2% of the pole mass, where the pole mass of a particle is defined as the position of the singularity in the propagator of the particle in perturbation theory.

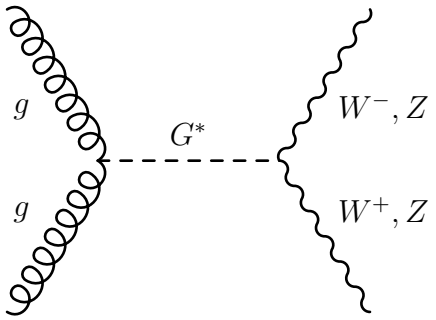

Figure 2.3: Feynman diagram of the production and decay of a KK excitation of the bulk RS graviton.

2.3.2 Extended Gauge Model

The Sequential Standard Model (SSM) is a proposed extension to the SM, which introduces additional heavy gauge bosons in a simple explorative manner [13]. The predicted charged and neutral bosons share similar properties to the SM W and Z bosons, and so are referred to as W' and Z' bosons respectively.

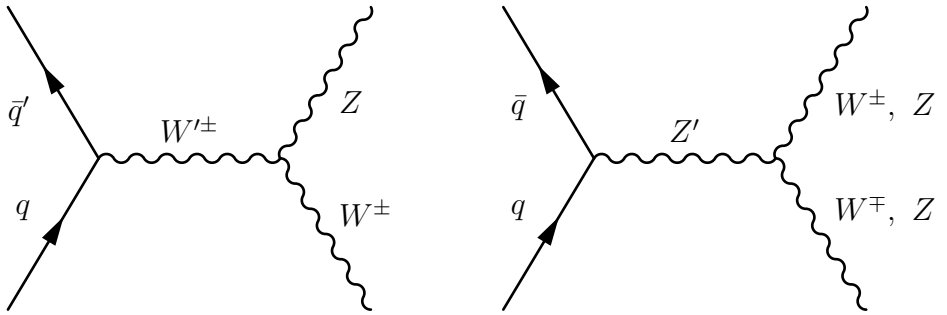

Figure 2.4: Feynman diagrams of the production and decay of the EGM W' boson (left) and Z' boson (right).

The SSM bosons share the same relative couplings to SM fields as their SM equivalents. For SSM bosons that are lighter than twice the mass of the SM W boson, the dominant decay is into fermions. Once the mass of the new boson $m_{V'}$ is sufficiently large that decaying into two gauge bosons is no longer forbidden, the diboson branching ratios increase rapidly as $m_{V'}^5$. The dependence of the diboson branching ratio on $m_{V'}$ is reduced to being linear by the introduction of a mixing factor between the SSM bosons and the SM equivalents of

$$\zeta = c\left(\frac{m_V}{m_{V'}}\right)^2. \tag{2.2}$$

The tunable coupling constant c is taken to be equal to 1 in the EGM case. At the LHC the dominant production mechanism is through quark-antiquark annihilation as shown in figure 2.4. For a W' boson with a mass above 0.5 TeV, the resonance width is approximately 3.6% of the pole mass.

2.4 Monte Carlo Event Modelling

Monte Carlo (MC) event generators are used to simulate particle interactions [14]. In a hadron collider, a simulated event can be broken down into multiple distinct processes.

The hard scatter process characterises an event, and is where the largest momentum transfer occurs. The momenta of the partons inbound to this event are described by a Parton Distribution Function (PDF), and perturbation theory gives a probabilistic distribution of the momenta of the outgoing particles.

In the parton shower phase, partons that are outbound from the hard interaction repeatedly radiate additional colour charged particles. These particles in turn radiate. As a particle continues to radiate, the momentum scale reduces until perturbation theory is no longer valid.

In a proton-proton interaction alongside the hard process there are typically multiple soft interactions. These lead to the production of parton showers in addition to those originating from the hard scatter event.

Hadronisation occurs at low momentum scales, when partons produced in showers can form bound states. Non-perturbative hadronisation models calculate the formation of these bound states.

During the hadronisation process, heavy unstable resonances can be formed. It is then necessary to model the decay of these unstable secondary particles.

To compare the simulated event to data, it is necessary to model the interaction of the generated outbound particles with the material of the detector. This is typically performed using Geant4 [15]. The event is then subject to a digitisation procedure that models the detector response, providing a digital readout from the simulated detector channels. The event now resembles data, and the same reconstruction techniques can be applied.

3

ATLAS and the LHC

3.1 The Large Hadron Collider

The LHC [16, 17] operates at high energy and high luminosity, with proton-proton collisions occurring at a centre of mass energy of $\sqrt{s} = 8$ TeV. Located at the European Organization for Nuclear Research (CERN), on the Franco-Swiss boarder near Geneva, the LHC is contained within a 26.7 km circumference tunnel ≈ 100 m underground, which formerly held the Large Electron-Positron (LEP) experiment, between 1989 and 2000.

3.1.1 LHC Timeline

The initial concept of the LHC dates back to 1984, four years prior to the completion of the LEP tunnel. Construction was approved by the CERN Council 10 years later in December 1994 and construction ran between 1998 and 2008. The two general-purpose detectors, CMS (The Compact Muon Spectrometer) [18] and ATLAS (A Toroidal LHC ApparatuS), which were designed to probe a wide range of new physics that may be present up to the TeV scale, were granted approval in January 1997. The following month saw approval granted to ALICE (A Large Ion Collider Experiment) [19], a more specialised detector to study

the strong interaction in the quark-gluon plasma created in heavy ion collisions. In September of the following year a fourth experiment, LHCb (Large Hadron Collider beauty) [20], a single arm forward spectrometer to study heavy flavour physics and the matter-antimatter asymmetry, was approved.

Construction of the LHC was completed in October 2008, and the first protons successfully circulated the following month [21]. In November 2009 the LHC exceeded the Tevatron's beam energy record and commenced a two week period of data collection at a centre of mass energy of 2.36 TeV. After a brief technical stop the main research programme began. The Run 1 data collection period commenced in 2010 with two years of data taking with a collision energy of 7 TeV and a bunch spacing of 50 ns. The run continued through 2012, with an increased collision energy of 8 TeV.

In 2013 the LHC entered its first Long Shutdown (LS), during which time it was refitted in order to be capable of ultimately reaching a collision energy of 14 TeV. Beam tests commenced in March 2015 at a beam energy of 6.5 TeV, with the first 13 TeV collisions occurring in May. The taking of data as part of Run 2 began in June with a collision energy of 13 TeV with an initial bunch spacing of 50 ns. The bunch spacing was subsequently reduced to 25 ns in August. Run 2 is planned to continue until the end of 2018, during which time the centre of mass energy increased to 14 TeV and is planned to deliver an integrated luminosity of ≈ 100 fb^{-1}.

The second long shutdown will follow Run 2, during which time the LHC will be refitted in order to achieve its ultimate design luminosity. Run 3 is scheduled to commence in 2021 and continue until the end of 2023, with a centre of mass energy of 14 TeV and a bunch spacing of 25 ns throughout. During Run 3 an integrated luminosity of ≈ 350 fb^{-1} is expected. The current proposed future is to greatly increase the luminosity during a third long shutdown, which will require almost three years starting at the end 2023. The resulting machine, the

High Luminosity LHC (HL-LHC), would continue the pattern of long shutdown followed by a physics run with Run 4 (2025), LS4 (2029), Run 5 (2030), LS5 (2032) and Run 6 (2034) [22, 23]. During these three runs, the HL-LHC is planned to reach a peak luminosity of $\approx 5 \times 10^{34}$ cm^{-2} s^{-1}, and deliver an integrated luminosity of ≈ 3000 fb^{-1}.

3.1.2 Design of the CERN Accelerator Complex

The design and operation of the CERN accelerator complex, including the LHC is here described. The analyses described in this thesis utilise data collected during Run 2. For this reason, where details vary between runs, the specifications for Run 2 are given.

The protons are accelerated through a complex of incremental accelerators prior to being injected into the the LHC [24], as seen in figure 3.1. Initially the protons are accelerated from an ion source, through the Linear Accelerator 2 (LINAC 2) up to an energy of 50 MeV and injected into the Booster. The Booster is the first of three synchrotrons [25] accelerating protons prior to injection into the LHC, and it has a radius of 25 m. Once the protons have reached a beam energy of 1.4 GeV they are fed into the Proton Synchrotron (PS), which further accelerates them up to an energy of 26 GeV. Once at this energy, the protons enter the Super Proton Synchrotron (SPS), which accelerates them to 450 GeV prior to injection into the LHC [26].

The SPS injects protons into the LHC via TI2 and TI8, allowing the proton beams to travel around the LHC clockwise and anticlockwise, respectively, in two separate beam pipes. It takes approximately eight minutes to fill both beams, after which the LHC continues to accelerate the beams using the superconducting Radio-Frequency (RF) cavities. During Run 1, a period of 20 minutes was required to reach the maximum beam energy of 4 TeV.

The LHC comprises eight identical arcs that are approximately 3 km long, sep-

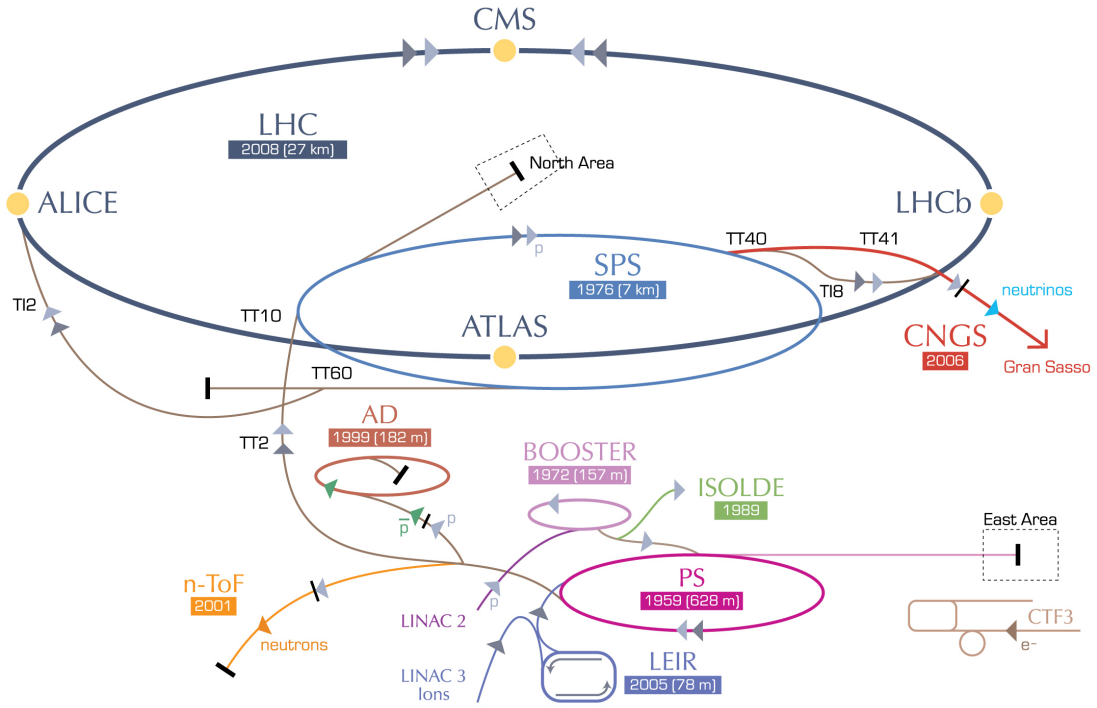

Figure 3.1: The CERN accelerator complex and the layout of the experiments [27].

arated by long straight sections. Each of the four collider experiments, ATLAS, CMS, LHCb and ALICE resides along one of the long straight sections, where the counter-rotating beams cross and the protons can be collided. The proton beams are made to follow the curvature of the arc sections by a dipole magnetic field generated by a total of 1232 superconducting niobium-titanium (NbTi) magnets. As the LHC accelerates the beams, the dipole magnets must be simultaneously ramped from 0.53 T at injection to a maximum of 4 T for 4 TeV beams, and intend to reach 8.6 T for 7 TeV beams.

Each of the two beams in the LHC consists of 1380 bunches of around 10^{11} protons, with a 50 ns bunch spacing for 8 TeV. This is due to increase to 2808 bunches separated by 25 ns when running with a beam energy of 14 TeV. The RF cavities are located at Point 4, between ALICE and CMS, and have a frequency of 400 MHz and an electric field gradient of 5 MV m^{-1}. Once the beams have reached peak energy, the RF cavities continue to provide approximately 10 keV

per proton each turn to account for losses through synchrotron radiation. In this state, the beams are made to cross within the four main experiments and can remain circulating for several hours.

3.2 The ATLAS Detector

The ATLAS detector is a general purpose particle physics detector intended for the study of a wide range of potential new physics that may exist at the TeV scale as well as for performing precision measurements of known phenomena [28, 29, 30, 31]. In order to facilitate this task the detector is required to be capable of:

- Tracking charged particles with a high precision and efficiency.
- Accurately measuring the energy of electrons, photons and hadrons.
- Precisely measuring the momenta of high energy muons.

The detector is constructed from three main subdetectors, the inner detector, the calorimeter system and the muon spectrometer, which address these requirements. To achieve a high acceptance in both pseudorapidity and azimuthal angle, these subdetectors are arranged within a barrel of concentric cylinders with disk shaped end-caps as shown in figure 3.2. The unprecedented high collision energy leads to the presence of high energy radiation. The high luminosity results in this radiation having a high intensity. The detector is required to be capable of operating in this environment.

3.2.1 Coordinate System

The ATLAS detector makes use of a right handed coordinate system with its origin at the nominal Interaction Point (IP). The z-axis is defined along the anti-clockwise beam direction and points towards what is referred to as the A-side, and

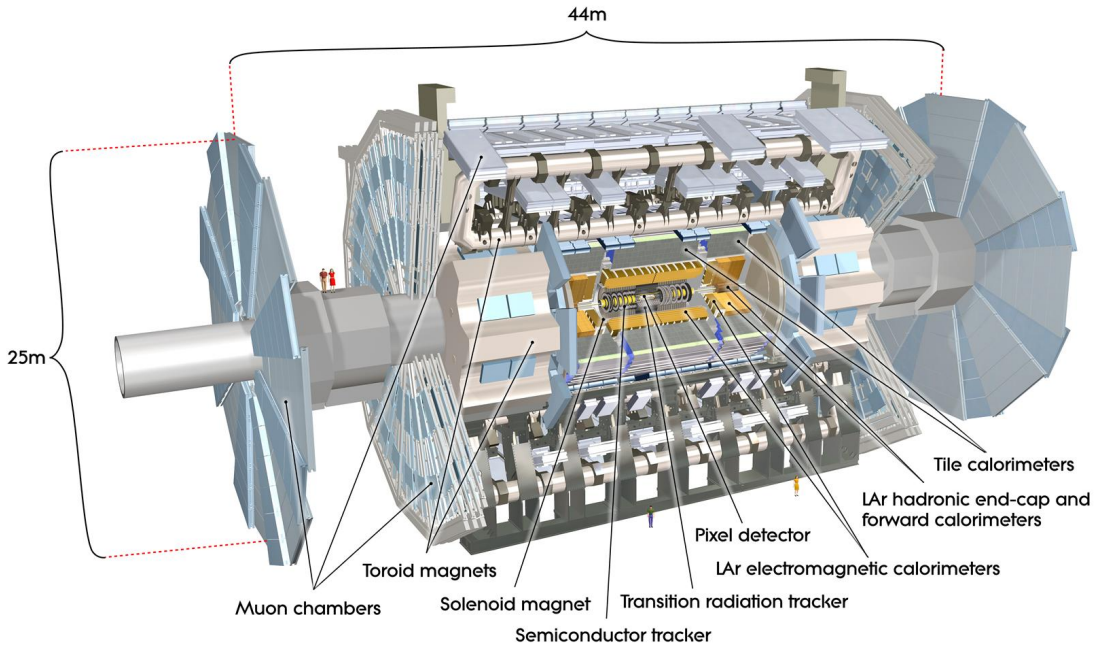

Figure 3.2: A cut-away schematic of the ATLAS detector [28].

away from the C-side. The x-axis points towards the centre of the LHC ring. The y-axis points upwards, however due to the inclination of the x-z plane of the LHC compared with the ground, the y-axis makes an angle of 0.704° with the vertical. The x-y plane is often referred to as the transverse plane, through which the azimuthal angle ϕ is measured, with $\phi = 0$ falling parallel to the positive x-axis in the range $0 \leqslant \phi < 2\pi$. The polar angle θ is defined as the angle from the beam direction such that $\theta = 0$ is parallel to the z-axis, and with $0 \leqslant \theta \leqslant \pi$. Particle trajectories are defined in terms of the polar angle θ and the pseudorapidity η, which is defined as

$$\eta = -\ln\left(\tan\left(\frac{\theta}{2}\right)\right). \tag{3.1}$$

Hence, $\eta = 0$ lies in the transverse plane, and $\eta = \infty$ ($\eta = -\infty$) points along the positive (negative) z-axis. When the mass of the particle cannot be neglected, the rapidity y, given by

$$y = \frac{1}{2} \cdot \ln\left(\frac{E + p_z}{E - p_z}\right), \tag{3.2}$$

is used. These are useful measures as the difference between two rapidities or pseudorapidities are invariant under Lorentz transformations along the z-axis. The distance ΔR in η-ϕ space is given by

$$\Delta R = \sqrt{(\Delta\eta)^2 + (\Delta\phi)^2}. \tag{3.3}$$

Hard scatter events within the detector have minimal momentum in the transverse plane, but in general have significant momentum along the z-axis. It is therefore useful to use properties calculated in the transverse plane. The component of a particle's momentum in the transverse plane can be calculated using the relation

$$p_T = |\mathbf{p}| \sin\theta. \tag{3.4}$$

Similar to this transverse momentum, the transverse energy is defined as

$$E_T = E \sin\theta. \tag{3.5}$$

Particles produced outside of the acceptance of the detector, or which do not interact in the case of neutrinos, can result in an imbalance in the total transverse energy, which is denoted as E_T^{miss}. In the instance of a two-body decay, where one of the decay products cannot be reconstructed, the invariant mass of the incident particle cannot be reconstructed. If it is assumed that the missed decay product is massless, then it is possible to use E_T^{miss} to calculate the transverse mass m_T using

$$m_T = \sqrt{2E_T E_T^{\text{miss}}(1 - \cos(\phi - \phi^{\text{miss}}))}, \tag{3.6}$$

where ϕ and E_T correspond to the azimuthal angle and transverse energy of the measurable decay product.

3.2.2 Magnet System

The ATLAS magnet system consists of four superconducting magnets; one solenoid and three toroids as shown in figure 3.3. The barrel solenoid, with its axis parallel to the beamline produces a 2 T magnetic field within the Inner Detector. The barrel and end-cap toroids maintain 0.5 T and 1 T fields respectively, which are required for the muon spectrometers.

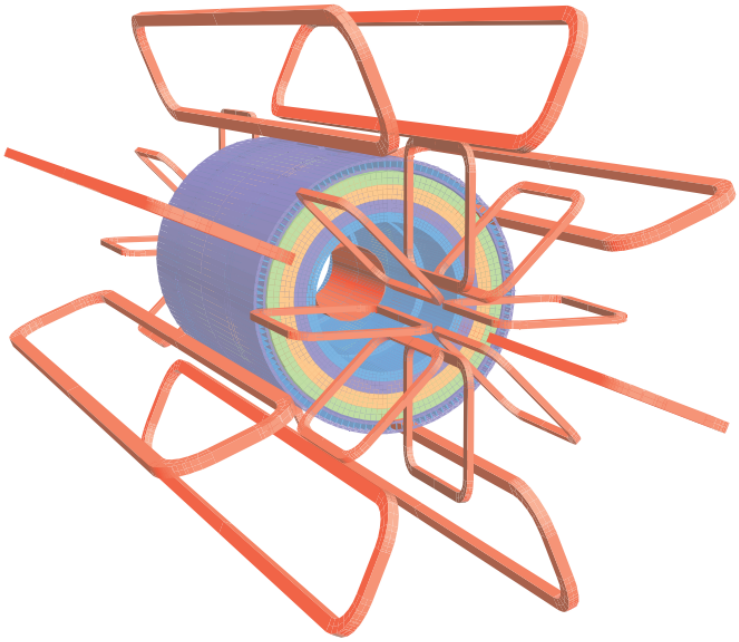

Figure 3.3: Layout of the ATLAS magnet system, including the magnet windings and tile calorimeter steel. The solenoid lies at the centre of the barrel surrounded by the calorimeter and return yoke. The remaining coils outside of the calorimeter comprise the barrel and end cap toroids [28].

3.2.2.1 Solenoid

The barrel solenoid, under nominal operating conditions, creates a field of 1.998 T at its centre [28]. The design is optimised to minimise the quantity of mass placed in front of the calorimeters, and in total contributes approximately 0.66 radiation lengths. This was in part achieved by containing the solenoid within the same vacuum vessel as the calorimeter and thus removing the need for separating

vacuum walls. The superconducting single layer coil contains 1154 turns of an aluminium stabilised NbTi conductor and is contained within a 12 mm thick aluminium alloy support structure. A layer of 2 mm thick aluminium panels is required as a heat shield between the solenoid and the Liquid Argon (LAr) cryostat. The solenoid has an axial length of 5.8 m, inner radius of 1.23 m and a thickness of 5 cm. The mass of the coil is 5.4 tonnes and the stored energy is 40 MJ.

3.2.2.2 Toroids

The barrel toroid is constructed from eight coils, each is contained within an individual stainless steel vacuum vessel, and has a mass of 45 tonnes. The toroid surrounds the calorimeter with inner and outer radii of 4.7 m and 10.1 m, and a length of 25.3 m along the z-axis. The field within the toroid ranges between 0.2 T and 2.5 T, storing a total energy of 1.1 GJ.

The end-cap toroids, similar to the barrel toroid, each consist of eight coils. Slotting between the coils of the barrel toroid, the end-cap toroids have inner and outer radii of 0.83 m and 5.4 m respectively, and each measures 5.0 m along the z-axis. Each toroid stores 250 MJ, with a field ranging between 0.2 T and 3.5 T.

3.2.3 Inner Detector

Located within the barrel solenoid, the Inner Detector (ID) is responsible for tracking charged particles created in events, measuring their momenta and calculating the location of vertices. The ID is constructed from the Pixel Detector, the Semiconductor Tracker (SCT), and the Transition Radiation Tracker (TRT). The layout is shown in figure 3.4. All three systems are split into two regions. Within the barrel region they are located on concentric cylinders, while in the end-cap region they are arranged into wheels perpendicular to the z-axis.

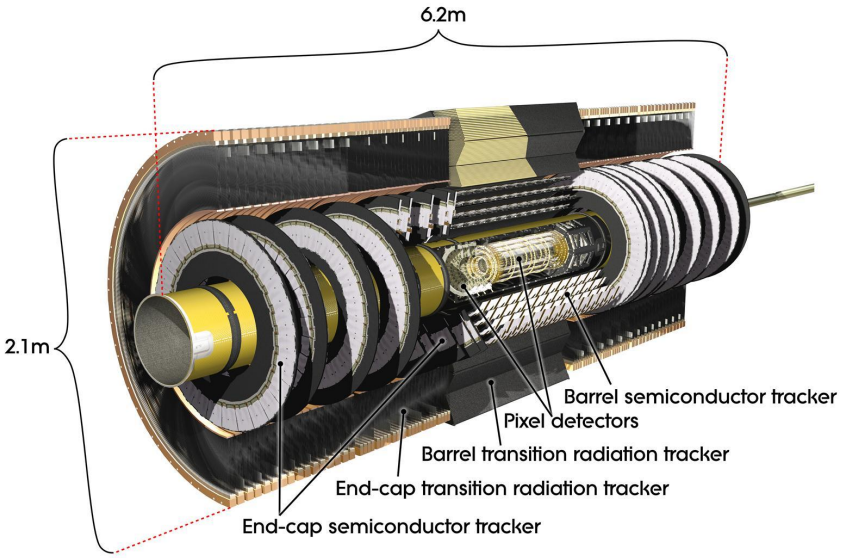

Figure 3.4: Cut-away view of the Inner Detector [32].

3.2.3.1 Pixel Detector

It is important to have a detector close to the interaction point that is capable of tracking charged particles to a high precision in order to calculate the position of both primary and displaced vertices, the latter being important for the identification of b-hadrons and tau leptons. This role is performed by the Pixel Detector. Due to the requirement for a high granularity around the vertex region, the Pixel Detector utilises 80 million readout channels, which is about half that of the whole of ATLAS [33, 34].

The Pixel Detector is composed of silicon detector modules divided into 50 µm by 400 µm pixels. The barrel section contains three cylindrical layers, the innermost layer of which is located 5 cm from the IP and is often referred to as the b-layer. The end-cap regions each have three disks and together with the barrel region allow track reconstruction in the region $|\eta| < 2.5$.

3.2.3.2 Semiconductor Tracker

Surrounding the Pixel Detector and of similar design is the SCT. The requirements for high resolution in this region of the detector is lower than in the Pixel Detector, so the geometry has been optimised to reduce cost while using the same silicon semiconductor technology. The SCT contains four cylindrical layers in the barrel and nine disks in each end-cap achieving coverage within $|\eta| < 2.5$

Each layer of the SCT has two strip layers, where a strip measures 6.4 cm by 80 µm. These layers are offset by 40 mrad in order to resolve ϕ and z (r and ϕ) in the barrel (end-cap), with one of the strip layers arranged parallel (perpendicular) to the beamline. The results of the strip geometry are that the SCT has a position resolution in the barrel (end-cap) in the ϕ and z (r and ϕ) plane of 17 µm by 580 µm and requires a total of 6.3 million readout channels.

3.2.3.3 Transition Radiation Tracker

The TRT is the outermost layer of the ID and provides r-ϕ and ϕ-z information in the barrel and end-cap regions up to $|\eta| < 2.0$. Constructed from over 350,000 drift tubes, also known as straw tubes, it is designed to a lower cost and has a lower material budget than both of the silicon detectors.

The straws are arranged parallel to the beam axis in the barrel region and perpendicular in the end-caps. The straws have a 2 mm radius and are up to 144 cm long in the barrel region, and 27 cm long in the end-caps. They are maintained at a temperature of 20°C by a flow of CO_2 around the TRT envelope. The 31 µm gold-plated tungsten anode is kept at ground potential, and the wall of the tube with thickness of 35 µm operates at a voltage of -1.530 kV. The volume of the straw is filled with a gas mixture of 70% Xe, 27% CO_2 and 3% O_2 which becomes ionised when particles pass through it. The electric field causes the electrons to drift to the anode, with a maximum collection time of 48 ns. The closest approach of a track to the anode can be calculated from the drift time

with a resolution of 130 μm. Despite the straws having a much lower resolution in comparison to the other ID subsystems, the TRT still significantly improves the overall position resolution of the ID due to tracks typically crossing 35-40 straws.

3.2.4 Calorimeters

The calorimetry system provides energy and position measurements of particles [35]. The calorimeters are capable of measuring the energy of all SM particles except neutrinos, which traverse the detector without interacting, and muons, which typically do not radiate a significant amount in the calorimeter. The calorimeter is subdivided into the EM and hadronic calorimeters, which are arranged as shown in figure 3.5, extending to $|\eta| = 3.2$ and $|\eta| = 4.9$ in the barrel and forward regions respectively. Both EM and hadronic calorimeters are constructed from alternating layers of absorbing materials that initiate particle showers, and sampling materials that perform the measurement of the showers. The sum of energy deposited from a shower can then be used to infer the energy of the incident particles. In order for the calorimeters to perform a measurement affectively, it is necessary for all the energy of the incident particle to be absorbed and to minimise punch-through into the Muon Spectrometer. Conversely to the ID, the calorimeter system therefore benefits from containing a large amount of material.

3.2.4.1 EM Calorimeter

The Electromagnetic Calorimeter (ECAL) measures the energy of electrons and photons in the energy range 5 GeV to 5 TeV. It is divided into the barrel ($|\eta| < 1.475$) and end-cap ($1.375 < |\eta| < 3.2$) regions, with the end-cap calorimeter subdivided into two coaxial wheels covering ranges of $1.373 < |\eta| < 2.5$ and $2.5 < |\eta| < 3.2$. Precision measurement is restricted to the region $|\eta| < 2.5$.

Layers of LAr sampler are sandwiched between the lead absorber in an accordion-like pattern as seen in figure 3.6. The accordion shape allows for full ϕ coverage

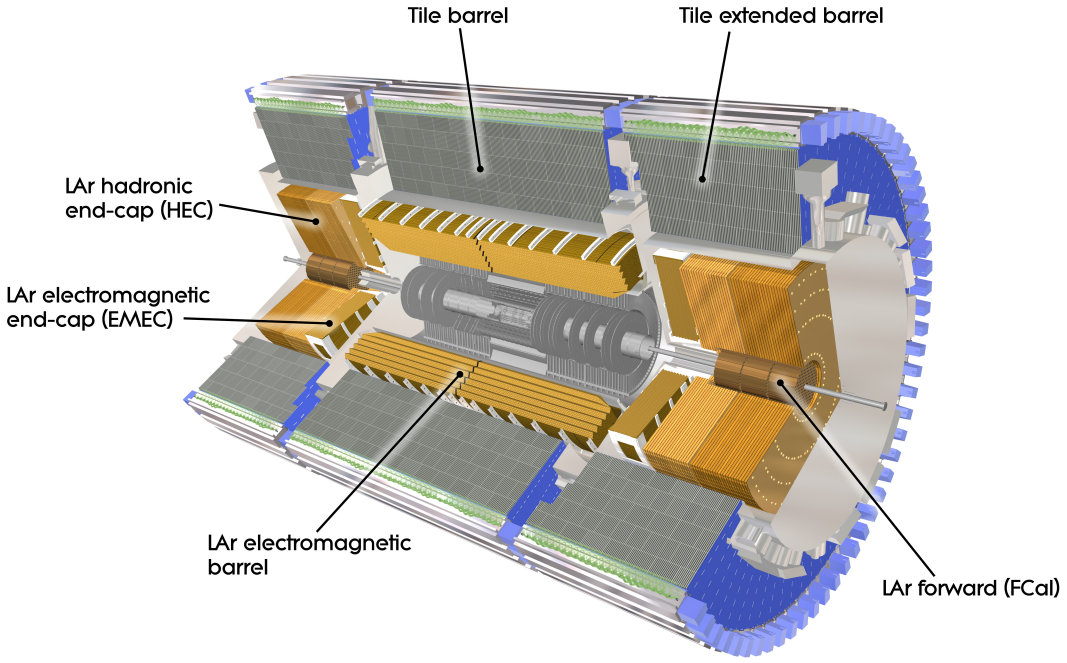

Figure 3.5: Cut-away view of the hadronic, electromagnetic and forward calorimeter systems [36].

to be obtained without azimuthal gaps as well as ensuring that particles traverse approximately the same amount of material independent of angle. The barrel region has a thickness greater than 22 X_0, and the end-cap has a thickness greater than 24 X_0, where X_0 is the radiation length.

The absorber causes incident electrons and photons to initiate electromagnetic showers, a process in which electrons radiate photons, and photons pair produce electrons. These shower constituents cause ions to be formed within the LAr. The electrons from these ionisation events drift towards the kapton electrodes which are held at 2000 V. The drift time is 450 ns, and thus spans the time of several bunch crossings. This leads to the possibility that an event may have an out of time pileup created by other bunch crossings. After noise has been accounted for,

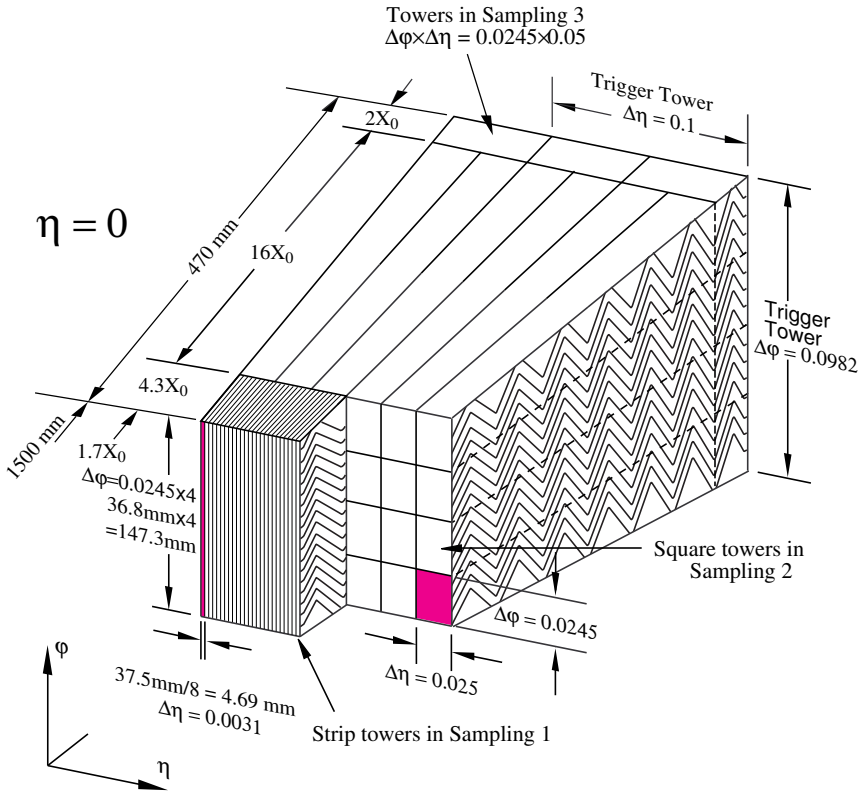

Figure 3.6: Diagram of the layered accordion structure of the ECAL, giving the granularities for each layer [37]. The trigger towers are also shown, which comprise the cells in windows of $\Delta\eta \times \Delta\phi$ space, and are used to identify activity in the ECAL as part of the Level 1 trigger.

the energy resolution of the ECAL is described by

$$\frac{\sigma_E}{E} = \frac{A}{\sqrt{E}} \oplus B, \tag{3.7}$$

where A, the stochastic sampling term, is 0.1 $\text{GeV}^{\frac{1}{2}}$, and the constant B, which describes cell level miscalibrations, is 0.007 [38].

For the precision region $|\eta| < 2.5$, the ECAL is segmented into three sections in depth numbered from 1 to 3, and named front, middle, and back, moving outwards from the beam axis. The granularities of the cells in these layers in $\Delta\eta \times \Delta\phi$ space are 0.1×0.0031 for Layer 1, 0.025×0.025 for Layer 2, and 0.050×0.025 for Layer 3. The maximum of a shower typically occurs within the middle layer,

covering the area of approximately 20 cells.

The particles must pass through the ID before reaching the ECAL, which accounts for between 0.5 and 2 radiation lengths. In order to accommodate the energy loss due to upstream interactions, a 1.1 cm (0.5 cm) LAr pre-sampler layer, located before the first layer of the barrel (end-cap), measures the position and energy of the shower prior to entering the ECAL within $|\eta| < 1.8$.

3.2.4.2 Hadronic Calorimeter

The central most part of the hadronic calorimeter is the Tile Calorimeter (TileCal), which is split into the barrel ($|\eta| < 1.0$) and extended barrel ($0.8 < |\eta| < 1.7$) regions, both of which occupy the region 2.28 m to 4.25 m radially from the beam axis. Both the barrel and extended barrel are subdivided into three layers of steel absorber and scintillating tiles, which are divided azimuthally into 64 modules. Compared to the interaction length λ, the three layers have a thickness of 1.5 λ, 4.1 λ and 1.8 λ in the barrel, and 1.5 λ, 2.6 λ and 3.3 λ in the extended barrel. The granularity of the tiles in $\Delta\eta \times \Delta\phi$ space is 0.1×0.1 in the first two layers, and 0.2×0.1 in the outermost layer, for both the barrel and extended barrel.

Wavelength shifting fibres read out from each side of each tile into two photomultiplier tubes. A trigger tower is used for triggering at Level-1, whereby a sum of E_T deposited in each layer of the ECAL and TileCal within a window in $\Delta\eta \times \Delta\phi$ space of 0.1×0.1 is calculated.

The Hadronic End-cap Calorimeter (HEC) is located in both end-caps behind the ECAL in the region $1.5 < |\eta| < 3.2$. There exists an overlap with both the TileCal and the Forward Calorimeter (FCal). It uses the same LAr technology as the ECAL, however, copper is used as the absorber. Each end-cap contains two wheels, each wheel containing two layers split into 32 wedges each. The HEC has a minimum of 0.372 m from the beam line, and a maximum radius of 2.03 m. The granularity of the HEC in $\Delta\eta \times \Delta\phi$ space is 0.1×0.1 for $|\eta| < 2.5$, and 0.2×0.2

for $|\eta| > 2.5$

The FCal located in the far forward region ($3.1 < |\eta| < 4.9$) of both end-caps is recessed 1.2 m from the ECAL front face to reduce neutron albedo in the ID cavity. This limits the overall size and necessitates a high density design. In each end-cap the FCal is 10 λ long, split into three modules. The first module utilises a copper absorber, and is optimised for EM calorimetry. The remaining two modules are optimised for hadronic calorimetry, using a tungsten absorber. Each module has regularly spaced channels passing through parallel to the beam axis. These contain electrodes surrounded by LAr, with channels in the first layer being as small as 0.25 mm to avoid ion build-up. The FCal has a granularity in $\Delta\eta \times \Delta\phi$ space of 0.2×0.2.

The energy resolution for the hadronic calorimeters is described by equation 3.7, with $A = 0.5$ GeV$^{\frac{1}{2}}$ and $B = 0.03$ for both the TileCal and HEC [39, 40], and $A = 1$ GeV$^{\frac{1}{2}}$ and $B = 0.1$ for the FCal [41].

3.2.5 Muon System

Muons traverse the ID and calorimeters without depositing a significant portion of their energy [42]. The Muon Spectrometer (MS) allows for the identification of muons, and measures the deflection of muons through the toroidal magnets. The momentum of muons is calculated from the combination of track information from ID and MS. The MS does not require the mass between it and the beamline to be minimised, as muons do not readily deposit energy and have a long lifetime in comparison to the time taken to traverse the detector. For this reason the MS forms the outermost layers of the detector, as shown in figure 3.7.

The magnetic field through which the muons are tracked is provided by the barrel toroid for $|\eta| < 1.4$, and the end-cap toroids for $1.6 < |\eta| < 2.7$. The transition region, $1.4 < |\eta| < 1.6$, between the toroids has a field provided by a combination of the two toroid systems. Approximately 1800 Hall sensors are used

to accurately monitor the field within the spectrometer. The MS comprises four types of chamber, each arranged in layers of three, parallel to the beam axis in the barrel region, and perpendicular in the transition and end-cap regions.

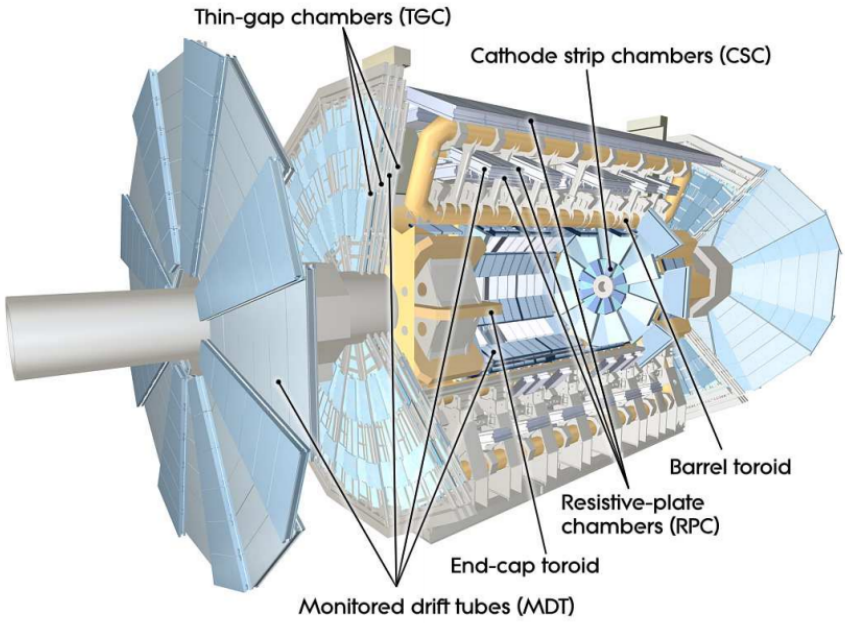

Figure 3.7: Cut-away of the ATLAS muon spectrometer [28].

The Monitored Drift Tubes (MDT) provide precision track measurement in the region $|\eta| < 2.7$. They have a relative alignment precision of 30 µm, both within the chamber towers and between adjacent towers. This alignment is monitored by 12000 optical alignment sensors.

The Cathode Strip Chambers (CSC) provide precision muon tracking within $2.0 < |\eta| < 2.7$, though with a higher granularity than the MDT. They are multi-wire proportional chambers in which the cathodes are segmented into strips. This design is capable of withstanding the higher rate and background conditions present in the end-caps [28].

The trigger system comprises Resistive Plate Chambers (RPC) for $|\eta| < 1.05$, and Thin Gap Chambers (TGC) for $1.05 < |\eta| < 2.7$. These chambers provide a second coordinate for the muons, orthogonal to the precision tracking, and provide a definite transverse momentum threshold necessary for effective triggering.

The momentum resolution of the MS has its minimum value of $< 4\%$ for muons with $p_T \approx 30$ GeV, and $> 12\%$ for muons with $p_T > 1$ GeV.

3.2.6 Forward Detectors

Measurement of the rate of elastic proton-proton scattering in the forward region allows for the total interaction rate, and so luminosity, to be calculated [43]. To perform this task two forward detectors are primarily used.

One of these is the LUminosity measurement using Cherenkov Integrating Detector (LUCID) [44] comprises two modules, 17 m either side of the IP, covering the pseudorapidity range $5.4 < |\eta| < 6.1$. The modules contain 200 Cherenkov counters each, and are capable of measuring luminosities up to 4×10^{33} cm^{-2} s^{-1}.

The Absolute Luminosity For ATLAS (ALFA) [45] detector, which consists of scintillating fibre trackers, is located ± 240 m from the IP, as close as 1 mm to the beam axis in Roman Pot units. These measure the trajectories of protons that have been elastically scattered through micro-radian angles in the Coulomb-Nuclear interference region [46].

3.2.7 Trigger and Data Acquisition

The maximum bunch crossing rate the LHC is capable of delivering is 40 MHz, with a total interaction cross-section of approximately 100 mb for a collision energy of 8 TeV. It is only possible to record events at 300 Hz, and interactions of interest have cross-sections around 1 pb. It is therefore necessary for each event to quickly decide whether or not to record the data. This selection is performed by the Trigger and Data AcQuisition (TDAQ) system, which comprises three consecutive levels; Level-1 (L1), Level-2 (L2) and Event Filter (EF) as depicted in figure 3.8.

The L1 trigger [47] is responsible for stepping the rate down from 40 MHz to

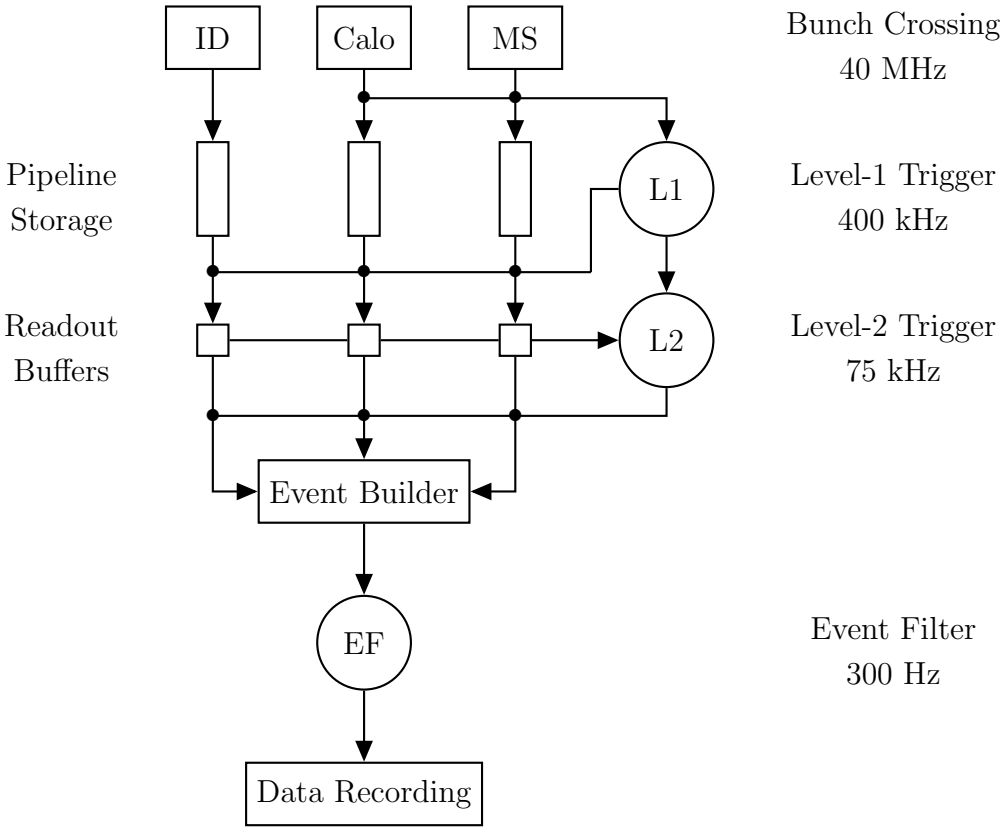

Figure 3.8: Schematic of the ATLAS TDAQ systems.

400 kHz. This is performed by providing limited information from the calorimeter, muon and forward detectors to the Central Trigger Processor (CTP) in order to identify electron, photon, jet and muon candidates, as well as specific event features such as missing transverse energy [48]. The CTP outputs a single bit Level-1 Accept (L1A), which triggers the event to be read from the pipelines of the front end electronics. The pipeline storage holds the information for 2 μs, after which a decision must have been received. The maximum time of flight for a particle within ATLAS is 0.75 μs, and the maximum cable distance from a detector to the dedicated L1 computing cluster is 80 m, resulting in 0.4 μs taken for the information to reach the CTP, and a further 0.4 μs for the decision to be transmitted back. This means that approximately 0.5 μs processing time is available before the pipeline storage overflows [49].

If an event passes the L1 trigger, the detector readout is passed to the High

Level Trigger (HLT), which comprises the two remaining TDAQ levels; L2 and EF [50]. The L2 trigger receives the detector readout, along with information from the L1 trigger defining Regions of Interest (RoIs), which contain the coordinates and the nature of the interesting candidate or features which led to the selection decision. From this information the L2 trigger takes approximately 40 µs on average to process an event, which reduces the rate from 400 kHz to 75 kHz.

Events passing the L2 trigger are transferred to an event building system. The EF then uses information from the entire detector, taking on average 4 s to process each event in a large computing farm. The final readout rate is approximately 300 Hz, requiring 1.3 MB per event.

3.3 Luminosity

The expected rate R of events resulting from a process with a cross-section σ, given the instantaneous luminosity $\mathcal{L}$, is

$$R = \mathcal{L}\sigma. \tag{3.8}$$

The instantaneous luminosity is given by

$$\mathcal{L} = \frac{nN_b^2 f_r}{4\pi\sigma_x\sigma_y}, \tag{3.9}$$

where n is the number of bunches per beam, N_b is the number of protons per bunch, f_r is the revolution frequency of the bunches, and σ_x and σ_y describe the transverse beam size. To maximise luminosity, the bunches are compressed in the transverse plane to 16 µm at the IP. For a beam energy of 4 TeV both ATLAS and CMS achieved a luminosity of order 10^{34} cm^{-2} s^{-1}, LHCb achieved 10^{32} cm^{-2} s^{-1}, and ALICE 10^{30} cm^{-2} s^{-1}.

The LHC commenced proton-proton collisions at a centre of mass energy of

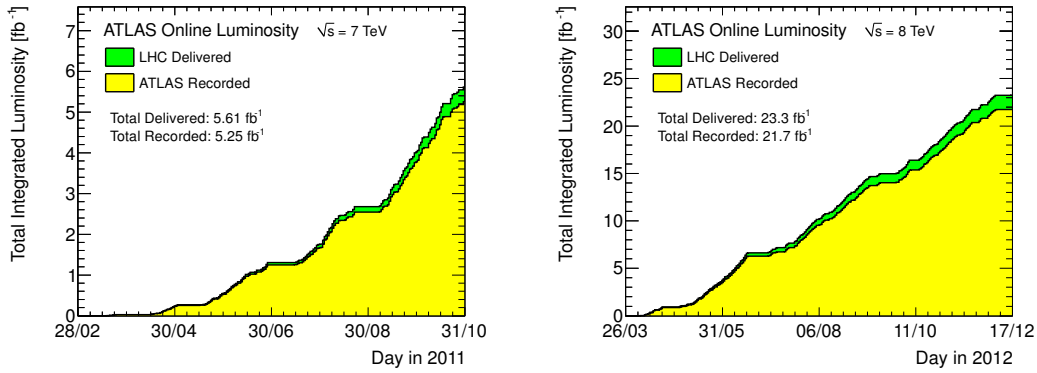

Figure 3.9: Cumulative luminosity collected with the ATLAS detector for proton-proton collisions for a centre of mass energy of 7 TeV (left) and 8 TeV (right). [51].

7 TeV on 30th March 2010. During the run from March to November 2011, ATLAS was capable of recording 5.25 fb^{-1} of the 5.61 fb^{-1} delivered integrated luminosity, with a peak luminosity of 3.65×10^{33} cm^{-2} s^{-1}

The centre of mass energy was increased to 8 TeV for the 2012 run, with proton-proton collisions taking place from April to December. During this period 21.7 fb^{-1} of integrated luminosity was recorded by ATLAS of the 23.3 fb^{-1} delivered, with a peak luminosity of 7.73×10^{33} cm^{-2} s^{-1}. The evolution of the data collection for both the 2011 and 2012 runs is shown in figure 3.9.

4

Object Reconstruction

The charged particle hits and energy depositions in ATLAS are reconstructed into physics objects which are used in analyses. Interactions between the incident particles and the ATLAS detector are simulated in MC using Geant4. The entire detector is modelled, allowing for local anomalies such as detector alignment or local inefficiencies to be accounted for. Figure 4.1 shows a depiction of the tracks and showers recorded by ATLAS due to interactions with various particles.

4.1 Inner Detector Tracks

The trajectories of charged particles are reconstructed as tracks within the ID, $|\eta| < 2.5$ using the TRT, the SCT and the Pixel Detectors. These tracks are parametrised by

$$\tau = (d_0, z_0, \phi_0, \theta_0, q/p)\,, \tag{4.1}$$

where the transverse impact parameter, d_0, and longitudinal impact parameter, z_0, are the coordinates of the perigee to the beamline. The ratio of the charge of the track to its momentum is given by q/p, and the azimuthal and polar angles, ϕ_0 and θ_0, are the direction of the track at the perigee.

Tracks are reconstructed from recorded space points of hits within the silicon

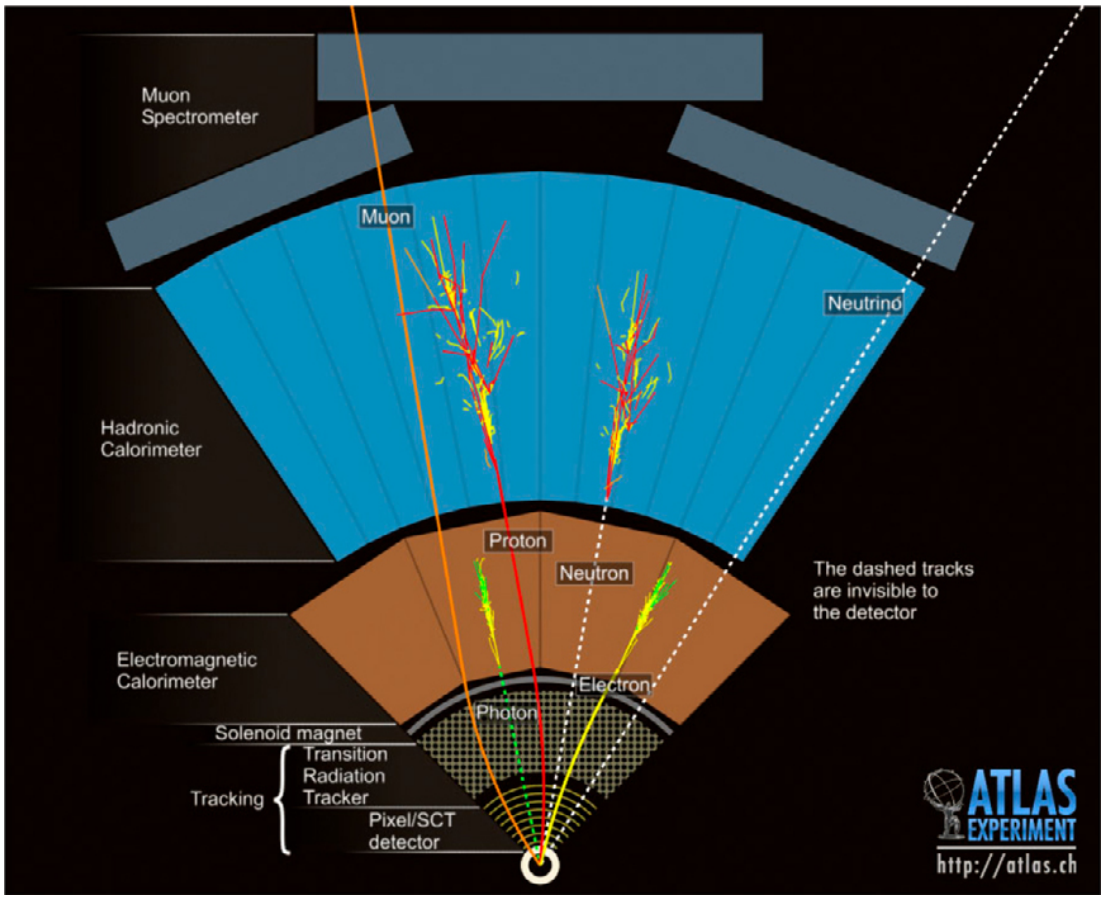

Figure 4.1: Cross-sectional representation of the ATLAS detector with examples of typical tracks and showers that lead to their identification [52]. Charged particles leave tracks in the ID, electrons, photons and hadronic jets deposit energy in the calorimeters, and muons leave tracks in the MS. Neutrinos propagate through the detector without interacting.

detector [53]. Space points can be constructed from a cluster of hits within the Pixel Detector within r-η-ϕ space, or the intersection of two back-to-back SCT module hits.

From three hits within the silicon detector, which are consistent with a particle with $p_T > 500$ MeV, a combinatorial Kalman filter is used to predict and add space points to the track moving from the beamline outwards [33]. This inside-out method resolves ambiguities by assigning tracks a score based on how likely the track is to originate from a real particle trajectory. Hits that are used in

the reconstruction of multiple tracks are then removed from all but the highest scoring track. The tracks are then extended through the TRT, refit, and the track score recalculated. If the extended track score is lower than the silicon only track score, the TRT information is ignored.

An outside-in method is also used, starting from hits recorded within the TRT and extending back through the silicon layers towards the beamline. This method is effective at identifying tracks originating from displaced vertices resulting from photon conversion and other neutral particle decays that may be overlooked by the inside-out method. Tracks reconstructed from the outside-in method, but without complementary hits in the silicon detector, are referred to as TRT-standalone tracks.

4.2 Primary Vertices

Proton-proton collisions occur within the beam spot, which extends for approximately 5 cm along the beamline and 15 μm perpendicular to it. Within this region for each bunch crossing there are approximately 20 primary vertices (PV). Reconstructed tracks are used to reconstruct a PV along the beamline, using the longitudinal impact parameter of a track to seed an iterative χ^2 fit of nearby tracks [54, 55]. The PVs are required to have a minimum of two tracks, but often have in excess of 20. Tracks that do not align with the PV by more than 7 σ are used to seed additional PVs.

4.3 Electrons

4.3.1 Reconstruction

Within the central region, electron objects are constructed from information recorded in the ID and ECAL [56, 57]. The central region of these subdetec-

tors extend to $|\eta| = 2.5$, however to ensure that the entire shower of an electron is contained within the ECAL, electron candidates are reconstructed only within $|\eta| < 2.47$.

Initial Cluster Reconstruction: Energy deposits within the ECAL are identified using a sliding-window algorithm and are used to initiate the electron reconstruction. A window size of 3×5 units is used, where one unit is 0.025×0.025 in η-ϕ space. The efficiency of this initial cluster is 97% for electrons with $E_T = 7$ GeV, increasing to almost 100% for $E_T > 20$ GeV.

Track Association: Tracks reconstructed within the ID with $p_T > 0.5$ GeV are extrapolated, with the impact point defined as the intersection of the track with the middle layer of the ECAL. Tracks are considered matched to an initial cluster if the distance from the impact point to the cluster position is within $|\Delta\eta| < 0.05$ and $|\Delta\phi| < 0.1$. In the instance that multiple tracks are associated to a cluster, priority is given to tracks that registered hits within the Pixel Detector and SCT. Finally, the track with the smallest ΔR between the impact point and cluster position is selected. If the matched track is one of two originating from a displaced vertex, then the cluster is tagged as a converted photon. If no track is matched, then the cluster is tagged as an unconverted photon.

Reconstructed Candidate: Once an initial cluster has an associated track, the electron inherits its position in η-ϕ space from its matched track at the primary vertex. Using the same unit size of 0.025×0.025 in η-ϕ space, the cluster size is increased from the initial 3×5 units to 3×7 units in the barrel, and 5×5 units in the end-caps. The total transverse energy of the electron is calculated from the sum of the estimated energy lost prior to the ECAL, the energy deposit in the cluster, and the lateral and longitudinal leakage. The estimated energy lost traversing the region prior to the ECAL is calculated using the pre-sampler. Lateral leakage is the energy deposited in the ECAL but outside of the cluster, and longitudinal leakage is the energy deposited beyond the ECAL. Corrections

are calculated from MC simulations for the lateral and longitudinal leakage and the cluster deposit sampling fraction of the calorimeter.

The absolute energy scale is calibrated to observations of $Z \to ee$, $J/\Psi \to ee$, and $W \to e\nu$ decays. The position of the ECAL relative to the ID is calibrated by comparing the impact point of the extrapolated track with the cluster position for electrons with $E_T > 20$ GeV, originating from a W or Z boson.

In the forward region $2.5 < |\eta| < 4.9$, no tracking is available, and so no distinction between electrons and photons is possible. Due to the reduced detector information, electron candidates reconstructed within this region are not considered in the analyses presented here.

4.3.2 Identification

The electron candidates in the central region are required to pass identification criteria in order to distinguish them from non-isolated electron background, and misidentified hadronic activity. To satisfy the requirements of the range of analyses performed within ATLAS, there are tiers of criteria ranging in efficiency and background rejection. Three such sets of criteria shall be described; *Loose++*, *Medium++* and *Tight++*. The requirements placed on shower shape variables are applied as functions of $|\eta|$ and E_T in order to optimise the identification criteria for the detector geometry and a large range of energy [58]. For each identification criterion, the efficiency to reconstruct an electron shown is calculated through the tag and probe method using the decays of Z bosons [57].

Loose++ has an efficiency of 95%. It places requirements on shower shape variables in the first two layers of the ECAL and the longitudinal leakage. It also requires track quality hits in the Pixel Detector and SCT, and requires track-cluster matching of $|\Delta\eta| < 0.015$.

Medium++ has an efficiency of 85%. Compared with Loose++, it places tighter requirements on shower shape variables, requires more hits within the

Pixel Detector and B-Layer, and introduces a criteria based on the TRT H_T fraction, where H_T is the scalar sum of the transverse energies in the cluster. A track-cluster matching of $|\Delta\eta| < 0.005$ and transverse impact parameter $d_0 < 5$ mm are required.

Tight++ has an efficiency of 78%. The shower shape requirements are the same or tighter than Medium++, and the transverse impact parameter of $d_0 < 1$ mm is required. Criteria are added to the ratio of cluster energy over track momentum, and on the $\Delta\phi$ between the matched track and cluster.

4.4 Muons

Muon candidates are reconstructed in the central region using both the ID, within $|\eta| < 2.5$, and MS, within $|\eta| < 2.7$. There are two main methods used for reconstructing muon tracks, Muid and Staco [59]. The Muid method is not detailed here as only the Staco method is used in the analyses described. Though the methods utilise different reconstruction and matching techniques they have comparable resolution and efficiency.

Dependent on where the muon track is first identified, or what part of the detector registers the track, the muon candidate falls into one of three categories, Muonboy, Staco Combined, or MuTag.

Muonboy: This method is required to extrapolate muon tracks between the various types of chamber, extrapolating the reconstructed track to the beam spot. The large distances between the muon chambers in the inhomogeneous magnetic field can lead to large extrapolation uncertainties. The algorithm is initiated on the Region of Activity (ROA), where a TGC or RPC is triggered. The ROA is approximately 0.4×0.4 in η-ϕ space, centred on the triggering hit, and all of the chambers which intersect this window are used to reconstruct track segments. Adjacent MDTs are sufficiently close that a straight line can be used

to approximate the track segment. These segments are required to extrapolate approximately to the beam spot. Due to the geometry of the drift tubes, there are four possible trajectories which could result in the recorded MDT hits. All four of these solutions are extrapolated through the remaining tubes within the MDT chamber, and are only considered valid if their quality factor, which is based on the χ^2 of their hits, is sufficiently high. The momentum of the valid track segments is estimated from their direction and extrapolated accounting for the magnetic field to the adjacent segments of the MS. If the track segment is matched, the momentum is recalculated and the extrapolation procedure continued. A track is considered valid if it is matched to at least one additional segment.

Staco Combined: By combining the Muonboy and ID tracks, the momentum resolution can be improved. The momentum measurement of the Staco Combined candidates is dominated by the MS for $p_T > 200$ GeV, and the ID for $p_T < 30$ GeV, and benefits over the Muonboy candidates for 6 GeV $< p_T <$ 200 GeV. The inclusion of track information from the ID also allows for the identification of muons that originate from displaced vertices.

MuTag: This method is initiated from ID tracks which are extrapolated and matched to track segments not associated to valid Staco tracks. This is particularly effective at identifying low-p_T muons, but is also capable of increasing the efficiency over the full momentum range.

The muon candidates are considered to be of different qualities depending on which method is used to reconstruct them [60]. Staco Combined muons are always considered Tight. A MuTag muon is considered Tight if it has at least three TGC ϕ hits in tagging segments, or is matched in at least two segments. MuTag candidates with $|\eta| > 1.05$, which are matched to only one tagging segment and no TGC ϕ hits in that segment, are considered Loose. The remaining MuTag and Muonboy candidates have a Medium quality.

4.5 Jets

Particles that develop parton showers within the calorimeters deposit energy in a large numbers of cells. The energy deposited is reconstructed using topological clusters. These clusters are then merged using a combination algorithm to reconstruct jets.

4.5.1 Topological Clustering

Topological clusters are reconstructed from groups of nearby calorimeter cells with significant energy deposits. These do not have a fixed size, but can vary depending on the energy deposition [61]. Each cell has noise associated to it, which consists of the quadrature sum of the RMS of the electrical noise and the expected pile-up. The noise varies from cell to cell and spans orders of magnitude. Pile-up contributions originate from additional vertices in the event, as well as neighbouring bunch crossings, due to the response time of the calorimeter exceeding the spacing between said bunches. The topological clustering is performed using a multi-stage algorithm.

Seed finding: Proto-clusters are initiated from cells that have a ratio of the deposited energy signal to noise exceeding t_{seed}.

Merging neighbours: A cell is classed as a neighbour if it has a signal to noise ratio exceeding $t_{\text{neighbour}}$ and is adjacent to the proto-cluster. Neighbours are iteratively added to the proto-cluster until all adjoining cells have a signal to noise ratio less than $t_{\text{neighbour}}$. If a cell is a neighbour to more than one proto-cluster then the two clusters are merged.

Additional cells: Cells which are adjacent to a neighbour cell are merged if their signal to noise ratio exceeds t_{cell}. If a cell adjoins multiple neighbours from different proto-clusters, the cell is merged with the neighbour which has the higher signal to noise ratio. This final process is not iterative, and cells that are adjacent

to a proto-cluster only after the inclusion of additional cells remain apart.

The standard parameters for topological clustering used in ATLAS are $t_{\text{seed}} = 4$, $t_{\text{neighbour}} = 2$, and $t_{\text{cell}} = 0$.

4.5.2 Jet Recombination Algorithms

Sequential recombination algorithms are used to combine the topological clusters and combine them into jets in a manner that is collinear and infra-red safe, meaning that the jet objects produced are stable under collinear splitting in the shower and the presence of additional soft radiation. The algorithms use the constituent-beam distance, d_{iB}, and the constituent-constituent distance, d_{ij}, given by

$$d_{iB} = {p_T}_i^{2n}, \tag{4.2}$$

$$d_{ij} = \min\left({p_T}_i^{2n}, {p_T}_j^{2n}\right) \frac{\Delta R_{ij}^2}{R^2}, \tag{4.3}$$

where R governs the radius of the reconstructed jets, and n governs the behaviour of the algorithm.

To iteratively combine the constituents, the algorithm first calculates the values of d_{ij} for all constituent pairings. The smallest value of d_{ij} is found. If this minimum value is less than d_{iB}, the constituents i and j are combined by summing their four-vectors. Otherwise, constituent i is classified as a jet and removed from the list of constituents. This process is repeated until there are no remaining constituents.

The parameter n changes the order in which the algorithm chooses to combine the constituents. The standard value used in ATLAS is $n = -1$, and this is referred to as anti-k_T [62]. The behaviour of the algorithm is similar for all negative values of n. Setting $n = 0$ removes the algorithm's dependence on momentum, and is called the Cambridge-Aachen (C/A) method [63]. A third method, which is not used in the analyses detailed here, is the k_T method, for

which $n = 1$ [64]. The behaviour of the algorithm is similar to k_T for all positive values of n. The shape of the jets reconstructed with the anti-k_T and C/A methods are shown in figure 4.2.

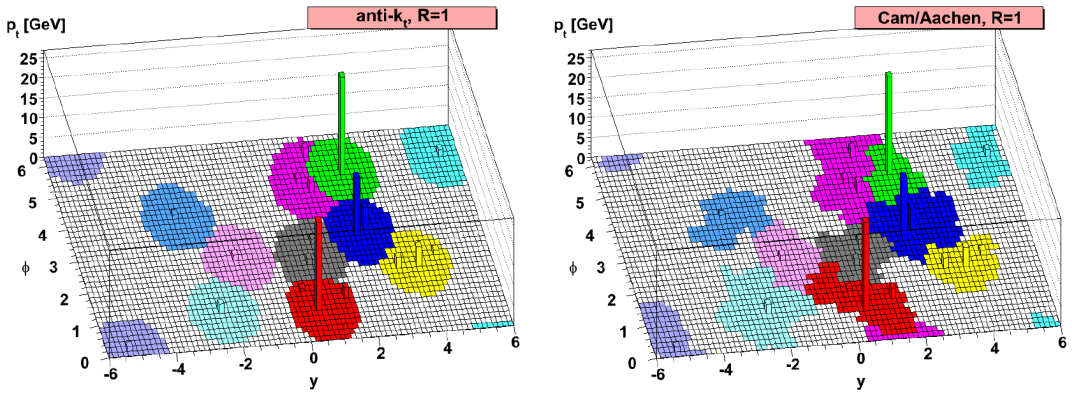

Figure 4.2: Comparison of the anti-k_T (left) and C/A (right) jet reconstruction algorithms applied to the same multi-jet event in η-ϕ space [62].

The behaviour of the anti-k_T method ensures that the distance between two soft constituents is much larger than the distance between the constituents of a hard-soft pair. This ensures that hard-soft clustering happens before soft-soft clustering is possible. This results in the jets having a uniform conical shape, with soft radiation having only a small effect on the jet boundary. If there are two hard constituents, a and b, such that $R < \Delta R(a, b) < 2R$, and $p_{Ta} \gg p_{Tb}$, then jet a maintains its conical shape, and jet b is cropped from the overlap region, as seen with the green and magenta jets in figure 4.2. If however $p_{Ta} \approx p_{Tb}$, both jets are cropped, with the border between them dependent of their relative p_T, as in the case of the red and grey jets. If there is a severe overlap, such that $\Delta R_{ab} < R$, then the two jets are combined into a single jet which typically has an irregular border, as seen with the magenta jet.

The C/A method initially combines constituents which are in close proximity regardless of p_T. The intention is to reconstruct the jet by reversing the order of the shower and hadronisation, under the assumption the parton splitting occurring at larger r will be closer in η-ϕ space. This physically motivated ordering

allows the jet to be decomposed and the substructure to be probed to determine the interaction which generated the jet.

4.5.3 Merged Jets

The high centre of mass energy in the LHC allows for W and Z bosons to be produced with very high momenta in excess of 1 TeV. As the momentum of a boson increases, the separation of the decay products obeys

$$\Delta R \approx \frac{2M}{|\mathbf{p}|}, \tag{4.4}$$

where M and $\mathbf{p}$ are the mass and momentum of the incident boson. The standard jet collection used within ATLAS applies the anti-k_T method with $R = 0.4$. For these parameters, the jets resulting from the decay begin to overlap when the momentum of the boson exceeds $\approx$ 250 GeV, and become merged when the momentum is twice this value. This means that reconstruction of the event becomes increasingly difficult when highly boosted vector bosons are present. In these instances it is advantageous to reconstruct the sum of the decay products of the boson into a single merged jet utilising a larger jet radius.

A jet that is due to a hadronic background process typically has a single hard core, with an even energy deposit in the surrounding cone, whereas a jet originating from a boosted boson has two hard cores in close proximity. The BDRS-A method discriminates between these two types of jet by analysing the substructure of C/A jets with a radius parameter of $R = 1.2$. The jet is reconstructed into smaller subjets and a mass drop filter technique applied [65].

The jet is initially decomposed by reversing the order of the initial C/A cluster algorithm by one step, forming two subjets. The momentum balance of the

subjets is defined as

$$y_f = \frac{\min\left(p_{T1}^2, p_{T2}^2\right)}{m_0^2}\Delta R_{12}^2 \approx \frac{\min\left(p_{T1}, p_{T2}\right)}{\max\left(p_{T1}, p_{T2}\right)}, \tag{4.5}$$

where m_0 is the mass of the parent jet, p_{T1} and p_{T2} are the transverse momenta of the subjets, and ΔR_{12} is the distance between the subjets. In the case that the two subjets share the momentum equally $y_f = 1$, and where one subjet contains all of the momentum of the parent jet $y_f = 0$. If $\sqrt{y_f} < 0.2$, then the subjet with the smaller mass is discarded, and the filter process repeated on the remaining subjet. Once the momentum balance criterion is satisfied the remaining constituents, which were not discarded during the filtering, are re-clustered using C/A with a radius parameter of $R = 0.3$, and the leading three jets are kept. After the filtering process the re-clustered subjets are used to recalculate the momentum of the initial merged jet. Performing this grooming and re-clustering improves the resolution of the energy and mass of the jet.

4.6 Missing Transverse Energy

The missing transverse energy, E_T^{miss}, is calculated from energy depositions in the calorimeter systems, and hits in the MS. The total missing transverse energy is calculated in the x and y directions, and combined using

$$E_T^{\text{miss}} = \sqrt{\left(E_x^{\text{miss}}\right)^2 + \left(E_y^{\text{miss}}\right)^2}. \tag{4.6}$$

The components E_α, with $\alpha = x, y$, are sums of contributions originating from the range of reconstructed physics objects.

$$\begin{aligned} E_\alpha^{\text{miss}} = {} & E_\alpha^{\text{miss},e} + E_\alpha^{\text{miss},\gamma} + E_\alpha^{\text{miss},\tau} + E_\alpha^{\text{miss,hard jets}} + E_\alpha^{\text{miss,soft jets}} \\ & + E_\alpha^{\text{miss,cell}} + E_\alpha^{\text{miss,calo }\mu} + E_\alpha^{\text{miss},\mu}, \end{aligned} \tag{4.7}$$

where the first five components account for reconstructed electrons, photons, hadronically decaying tau leptons, hard jets and soft jets respectively [66, 67]. The cell component accounts for calorimeter energy deposits that were not matched to ID tracks. The final two components account for reconstructed muons, where the 'calo μ' term considers calorimeter cells that reconstructed muons have passed through.

5

Diboson Resonance Search in the $\ell\ell qq$ Final State

5.1 Introduction

The naturalness problem suggests that a modification or extension to the SM may be required. A consequence of this extension would be the existence of new particles and interactions at the TeV scale. Detailed here is a search in the semileptonic decay channel $WV \to \ell\ell qq$, where V stands for a W or Z boson, and ℓ for either an electron or muon.

The two benchmark models used in this search to probe for new physics are the bulk RS gravitons G^*, with $k/\bar{M}_{\rm Pl} = 1$, and the EGM W' boson with $c = 1$, as described in section 2. Both signal models predict large branching ratios to vector boson pairs.

The semileptonic final state achieves a greater suppression of background events than the fully hadronic final state due to the requirement of two leptons. Compared with the fully leptonic final state, the $\ell\ell qq$ channel benefits from the larger branching ratio of vector bosons to hadrons. In addition, the absence of neutrinos in the final state allows the invariant mass of the diboson system to

be reconstructed.

Frequentist methods are used to quantify the agreement between the data and the background only hypothesis, and limits are set at the 95% Confidence Level (CL) on the product of the production cross-section and branching ratio for the two benchmark models.

Previous searches for graviton models and W' bosons have been performed using $p\bar{p}$ collisions at $\sqrt{s} = 1.96$ TeV at the Tevatron. The D0 Collaboration performed searches for resonant WW and WZ production, excluding the RS1 graviton between 300 GeV and 754 GeV, and the SSM W' boson between 180 GeV and 690 GeV, at the 95% CL [68, 69]. The CDF Collaboration performed searches for resonant ZZ production in the $\ell\ell\ell'\ell'$, $\ell\ell\nu\nu$ and $\ell\ell qq$ decay channels, which excluded the RS1 graviton between 300 GeV and 1000 GeV at the 95% CL [70].

Searches performed by ATLAS and CMS have excluded production of the EGM W' boson at the 95% CL. Using the $\ell\nu\ell'\ell'$ final state, both ATLAS and CMS collaborations excluded production below 1.52 TeV [71] and 1.55 TeV [72] respectively. Production was also excluded by the ATLAS collaboration below 1.49 TeV [73] using the $\ell\nu qq$ final state. Fully hadronic final states were used by the ATLAS collaboration to exclude production between 1.3 TeV and 1.5 TeV [74], as well as by the CMS collaboration to exclude production below 1.7 TeV [75].

The ATLAS collaboration has excluded at the 95% CL the production of bulk RS gravitons below 760 GeV using the $\ell\nu qq$ channel [73]. The CMS collaboration, using the fully hadronic channel, has excluded $G^* \to WW$ and $G^* \to ZZ$ production below a mass of 1.2 TeV [75].

5.2 Data Samples

The data used in the analysis were collected with the ATLAS detector during the 2012 proton-proton run. The centre of mass energy is 8 TeV, and there is an average of 21 interactions per bunch crossing. During 2012, ATLAS recorded an integrated luminosity of 21.7 fb^{-1}. Portions of this dataset were removed due to data corruption and offline subdetectors. A final dataset with an integrated luminosity of 20.3 fb^{-1} is used.

5.3 Trigger

The trigger criteria used to select candidate events are based on the identification of the leptons resulting from a Z boson decay. Separate chains are used for events containing electrons and muons.

For events containing electrons, a sliding window algorithm is used in the L1 trigger. Showers within the ECAL are selected if the total energy contained is above a noise threshold. The Regions of Interest (RoI) are passed to the L2 trigger, which uses information from the ID to ensure that the cluster has an associated track. The EF then imposes criteria on the quality of the electron object [57]. Events are selected if they pass at least one of the following sets of requirements:

`EF_e60_medium1`: At least one electron with $E_T > 60$ GeV that passes a medium quality criteria.

`EF_e24vhi_medium1`: At least one isolated electron with $E_T > 24$ GeV that passes a medium quality criteria

`EF_2e12Tvh_loose1`: At least two electrons which each have $E_T > 12$ GeV, passing a loose quality criteria.

In the case that events contain muons, the L1 trigger identifies coinciding hits in the MS and uses dedicated hardware to calculate the momentum of the muon candidate [76]. The L2 and EF levels proceed similarly to the electron case, with events being selected if they pass one of the following requirements:

`EF_mu36_tight`: At least one muon with $p_T > 36$ GeV that passes a tight quality criteria.

`EF_mu24i_tight`: At least one isolated muon with $p_T > 24$ GeV that passes a tight quality criteria.

`EF_mu18_tight_mu8_EFFS`: A pair of muons, one with $p_T > 18$ GeV, and one with $p_T > 8$ GeV, both passing a tight quality criteria.

For a given analysis the chosen trigger criteria should result in a looser set of criteria than the final selection. A measure of this is the trigger efficiency, defined as the ratio of the number of events that pass the trigger and the offline selection, over the number of events that pass the offline selection regardless of the trigger. The trigger efficiency is 99% (92%) for the electron (muon) events, for all signal masses, and independent of lepton p_T. The reduced efficiency in the muon channel is due to the geometric acceptance of the L1 trigger caused by services for the ID and ECAL.

5.4 Object Selection

Detailed here are the requirements used for selecting physics objects to be used in the analysis. The signal hypothesis is simultaneously searched for in alternative final states with the intention of combining the results. To facilitate this combination, a second category of leptons is defined that is common to each analysis, with a looser selection than the signal leptons. Each analysis requires events to

have the exact number of signal leptons, with no additional veto leptons to ensure the use of statistically independent datasets.

5.4.1 Electrons

Electron candidates that are reconstructed within the ID but not the calorimeter are rejected. The electrons are required to pass the Medium++ electron identity requirements and are vetoed if the cluster is categorised as bad quality.

To ensure that the electron candidate originates from the interaction region, the longitudinal impact parameter $|z_0 \sin\theta|$ from the PV must be less than 0.5 mm, and the transverse impact parameter $|d_0|$, divided by its uncertainty $\sigma(d_0)$, must be less than six.

The electron transverse energy is required to be > 25 GeV to guarantee a high trigger efficiency, and the pseudorapidity is required to be in the range $|\eta| < 1.37$ or $1.52 < |\eta| < 2.47$ to ensure that the shower is entirely within the acceptance of the ECAL and avoids the transition region between the barrel and end-cap.

Isolation requirements are applied to the track p_T and calorimeter E_T surrounding the electron candidate after corrections have been applied to account for the p_T and energy leakage from the electron core, and the number of PVs in the event. Details on the application of the isolation requirements are given in section 5.4.3.

The looser veto electrons share many of the selection criteria of the signal electrons, and only differ in the following manner. There is no requirement placed on the cluster quality, and the minimum transverse energy requirement is reduced to 20 GeV. The longitudinal impact parameter $|z_0 \sin\theta|$ is required to be < 2.0 mm, and the calorimeter isolation is not applied.

5.4.2 Muons

The Staco Combined muon collection is used, as described in section 4.4. Requirements are made of the track quality in order to remove events which would otherwise contain 'fake'muons, and to ensure that the positions and momenta of the muons are well measured. A hit is required in the inner most layer of the ID if one is expected from the overall track fit. The sum of the number of hits in the Pixel Detector and the number of dead pixels traversed is required to be $\geqslant 1$. The sum of the number of SCT hits and the number of dead SCT sensors traversed is required to be $\geqslant 5$. The sum of pixel and SCT track holes must be < 3.

A high quality TRT track is required if the muon track is within the η acceptance of the TRT. Defining N_{TRT} as the sum of the number of TRT track hits, and N_{outliers} as the number of track hit outliers, muon tracks in the region $0.1 < |\eta| < 1.9$ are required to have $N_{\mathrm{TRT}} > 5$. Muon tracks in all parts of the TRT are required to have $N_{\mathrm{outliers}} < 0.9\ N_{\mathrm{TRT}}$ if $N_{\mathrm{TRT}} > 5$.

A good agreement between the measurements from the ID and MS is ensured by requiring that the charge over momentum measurements, q/p, satisfy $|(q/p)_{\mathrm{ID}} - (q/p)_{\mathrm{MS}}| < 5\ \sigma_C$, where σ_C is the combined q/p uncertainty.

To ensure that the muon candidate originates from the interaction region, the longitudinal impact parameter $|z_0 \sin\theta|$ from the PV must be less than 0.5 mm, and the transverse impact parameter $|d_0|$, divided by its uncertainty $\sigma(d_0)$, must be < 3.5.

The muon is required to have $p_T > 25$ GeV to ensure a high trigger efficiency, and $|\eta| < 2.5$ to ensure that the candidate is within the ID acceptance. Isolation requirements are applied to the track p_T and calorimeter E_T surrounding the muon candidate after pile-up corrections are applied by a muon isolation correction tool [77]. Details on the application of the isolation requirements are given in section 5.4.3.

The looser veto muons share many of the selection criteria of the signal muons, and only differ in the following manner. The transverse momentum is required to be > 20 GeV, and the longitudinal impact parameter $|z_0 \sin\theta|$ is required to be < 2.0 mm. No calorimeter isolation is applied.

It is possible that a muon with high p_T could radiate a photon within the detector volume, which could subsequently be reconstructed as an electron. For this reason any electron candidates within $R = 0.1$ of a selected muon are removed. This removal is applied equally to electron and veto electron candidates.

5.4.3 Lepton Isolation

For the leptons to be well measured, there must be minimal detector activity in the region surrounding the candidate. This isolation is required separately in the tracking and calorimetry subsystems.

The standard track isolation parameter used in ATLAS, $\text{Isolation}_{\text{track}}(R)$, is the sum of the transverse momenta of tracks with $p_T > 1$ GeV within R of the candidate lepton's track, excluding the lepton itself. The calorimeter isolation parameter $\text{Isolation}_{\text{calo}}(R)$ is defined as the sum of transverse energy in calorimeter cells within R of the candidate lepton, excluding the lepton itself.

Lepton candidates are required to have a track isolation of $\text{Isolation}_{\text{track}}(0.2) < 0.15\ p_T^l$, where p_T^l is the transverse momentum of the lepton candidate. The calorimeter isolation parameter $\text{Isolation}_{\text{calo}}(0.2)$ must be less than $0.3\ E_T^l$ ($0.3\ p_T^l$) of the electron (muon) candidates.

The decay products of boosted bosons become increasingly close as the boson momentum increases. As the boson p_T exceeds approximately 1 TeV, the distance between the decay products reduces to within $R = 0.2$. Subsequently, the isolation cone contains contributions from multiple leptons, causing signal events to fail the lepton isolation criteria. To accommodate this, a modified dilepton isolation variable is used, where a correction is made for the presence of a second

lepton candidate, l_2, such that

$$\text{Isolation}_{\text{track}}^{\text{Dilepton}}(R) = \text{Isolation}_{\text{track}}(R) - p_T^{l_2}. \tag{5.1}$$

Three scenarios are defined upon which the isolation criteria are dependent.

Standard Isolation: When $\Delta R(l,l) > 0.25$, the core of each lepton is completely removed from the isolation cone of its counterpart. Standard track isolation criteria are applied to electron and muon candidates, with $\text{Isolation}_{\text{track}}(0.2) < 0.15\, p_T^l$. Standard calorimeter isolation criteria are implemented for electrons with $\text{Isolation}_{\text{calo}}(0.2) < 0.3\ E_T^l$, and for muons with $\text{Isolation}_{\text{calo}}(0.2) < 0.3\ p_T^l$.

Overlap Region: When $0.2 < \Delta R(l,l) < 0.25$, the track of the second lepton candidate is outside the isolation cone of the first, so the standard track isolation is applied, $\text{Isolation}_{\text{track}}(0.2) < 0.15\, p_T^l$. The calorimeter cluster of the counterpart signal lepton will partially overlap, so no calorimeter isolation is applied.

Dilepton Isolation: Once $\Delta R(l,l) < 0.2$, the isolation cone around the lepton candidate contains the track of the second lepton, so the dilepton isolation criterion, $\text{Isolation}_{\text{track}}^{\text{Dilepton}}(0.2) < 0.15\ p_T^l$ is required. As with the overlap region, no calorimeter isolation is applied.

The effect of these modified dilepton isolation criteria is demonstrated in figure 5.1 on a graviton MC sample with a pole mass of 2 TeV. In this case the $\text{Isolation}_{\text{track}}$ criteria results in a very low acceptance for $R(l,l) < 0.2$. In contrast, the dilepton isolation for the same sample achieves a much higher acceptance for both lepton flavours.

A comparison of the acceptance of the nominal and dilepton isolation criteria as a function of the bulk RS graviton pole mass is shown in figure 5.2. The standard isolation criteria are shown to lose efficiency above approximately 1.5 TeV, rejecting a significant percentage of signal events for the highest mass signal samples. In contrast, the dilepton isolation criteria maintain a high signal efficiency

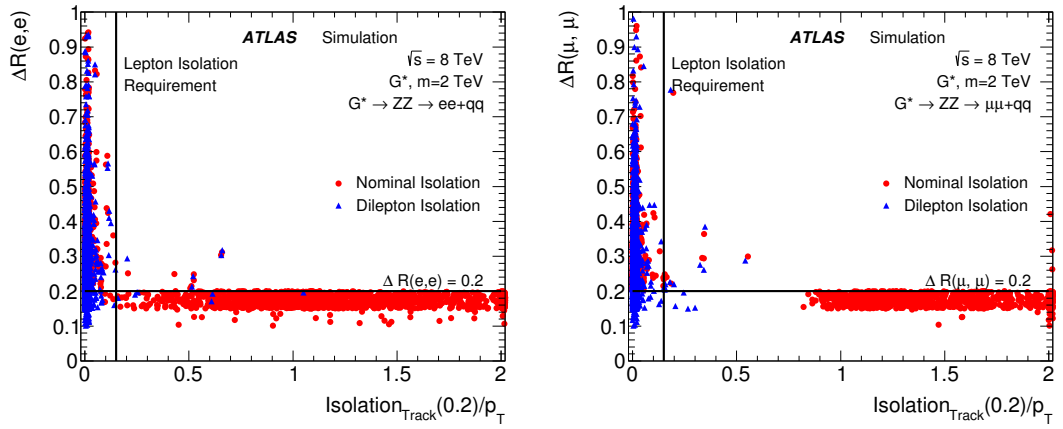

Figure 5.1: A comparison of the nominal single lepton (red circles) and dilepton (blue triangles) track based p_T isolation with a cone size of $R = 0.2$ against $\Delta R(l, l)$, between the two leptons resulting from a simulated 2 TeV bulk RS graviton decaying through two Z bosons into e^+e^-qq (left) and $\mu^+\mu^-qq$ (right). The horizontal lines correspond to $\Delta R(l, l) = 0.2$, where the dilepton isolation is applied, and the vertical lines correspond to the applied isolation criteria.

through the complete range of signal pole masses.

5.4.4 Jets

Two different jet collections are used in this analysis to facilitate the optimisation to a wide range of resonant signal masses. The low mass jets, referred to as small-R jets or j, use the anti-k_T algorithm with a radius parameter of 0.4. For resonant masses above approximately 1 TeV, C/A jets are used with a radius parameter of 1.2, referred to as large-R jets or J.

The small-R jets are required to have $|\eta_{\text{EM}}| < 2.1$, where η_{EM} is the defined as the pseudorapidity as measured by the ECAL prior to applications of any energy corrections. After the full Local Cluster Weighting Jet Energy Scale (LCW+JES) calibration is applied [78, 79], the jets are required to have $p_T > 30$ GeV. The jets are also required to satisfy a set of jet quality criteria which reject jets with calorimeter noise [80]. The Jet Vertex Fraction (JVF) of jets with $p_T > 50$ GeV

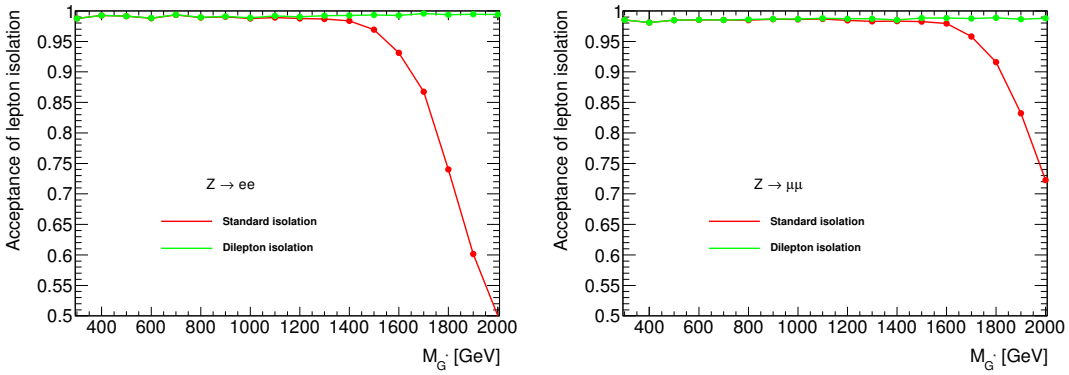

Figure 5.2: Comparison of the total signal acceptance of the nominal and dilepton isolation, against the bulk RS graviton pole mass for the e^+e^-qq (left) and $\mu^+\mu^-qq$ (right) selection regions.

is required to be greater than 0.5, where JVF is defined as the ratio of the scalar sum of p_T of tracks associated to the jet and originate from the PV, over the scalar sum of p_T of all tracks associated with the jet.

The large-R jets are subject to the BDRS-A filtering described in section 4.5.3, and are representative of hadronically decaying vector bosons. The highest p_T jet in this collection is required to have $\sqrt{y_f} > 0.45$, and a mass m_J, satisfying 70 GeV $< m_J <$ 110 GeV. This window is sufficiently wide as to accept jets originating from both W or Z bosons.

The jet reconstruction algorithm does not distinguish between calorimeter deposits originating from electrons or hadrons, and so electrons are also reconstructed as jets. Small-R (large-R) jets which have an electron reconstructed within a cone of 0.3 (0.8) are removed.

5.5 Event Selections

This analysis selects a final state with two high p_T electrons or muons originating from a Z boson, and at least one reconstructed jet from a W or Z boson decay. To optimise the acceptance over the large range of signal masses, three regions,

the low-p_T resolved region (LR), high-p_T resolved region (HR), and merged region (MR), are defined. Both the LR and HR require at least two small-R jets to be reconstructed. At least one large-R jet is required in the MR.

For all three of these regions, at least one PV is required, and the vertex with the highest $\sum p_T^2$ of associated tracks is required to have at least three tracks associated with it. The event must not have a data quality flag indicating the presence of noise in the LAr calorimeter, and no jets with calibrated $p_T > 20$ GeV must have 'looser bad' jet quality [80]. There must either be exactly two electrons, or exactly two opposite charge muons, such that the dilepton mass m_{ll}, satisfies 66 GeV $< m_{ll} <$ 116 GeV. In both cases there must be no additional veto leptons of either flavour. At least one of the selected leptons must have $p_T > 25$ GeV, and match the trigger object.

The additional criteria specific to each of the three signal region selections are as follows:

Low-p_T resolved region: The transverse momentum of the dilepton system is required to satisfy, $p_T^{ll} > 100$ GeV. The two jets with the highest transverse momenta are used to reconstruct the hadronically decaying boson candidate. The dijet transverse momentum must satisfy, $p_T^{jj} > 100$ GeV. The dijet mass is required to be within the window, 70 GeV $< m_{jj} <$ 110 GeV. The distribution of the dilepton transverse moment after the selection of two muons and two small-R jets, and the associated Receiver Operating Characteristic (ROC) are shown in figure 5.3. The dijet transverse momentum distribution for the LR after the dilepton p_T requirement is applied is shown in figure 5.4, with the associated ROC.

High-p_T resolved region: Compared with the LR, the HR has higher dilepton and dijet p_T requirements. The transverse momentum of the dilepton system is required to satisfy, $p_T^{ll} > 250$ GeV. The dijet transverse momentum must satisfy, $p_T^{jj} > 250$ GeV. The dijet mass must be within the window, 70 GeV $< m_{jj} <$

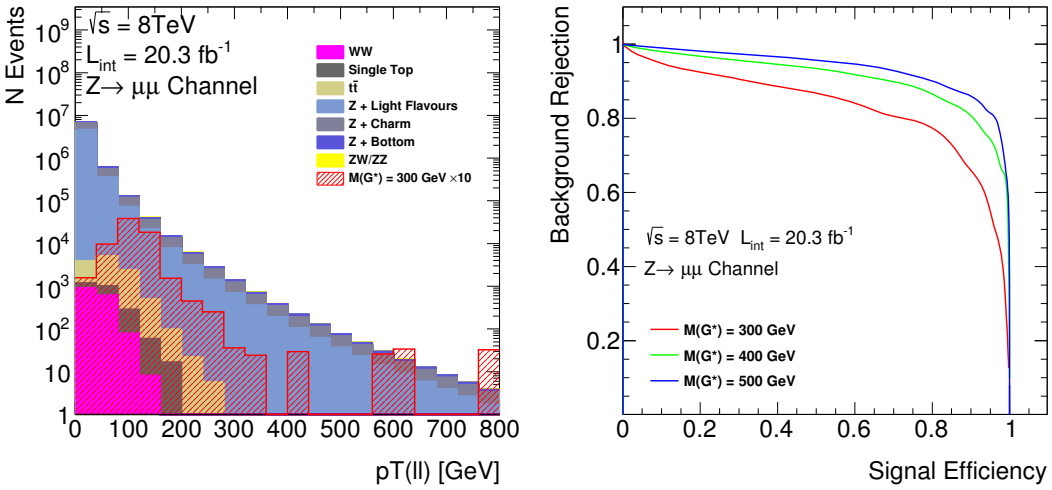

Figure 5.3: The di-muon p_T distribution for the LR (left), and the associated ROC curves (right).

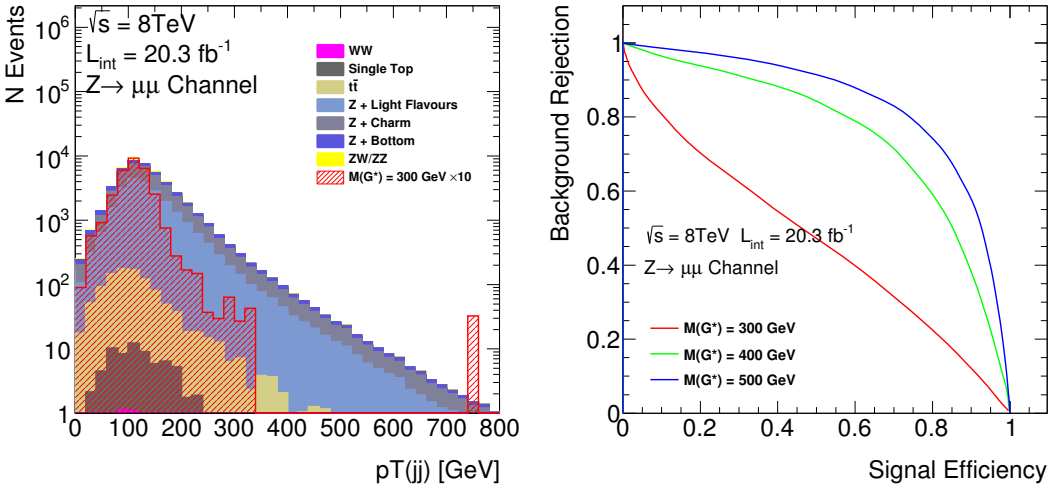

Figure 5.4: The dijet p_T distribution for the muon LR (left), and the associated ROC curves (right), after the p_T^{ll} requirement is applied.

110 GeV. As with the LR, the dijet mass is required to be within the window, 70 GeV $< m_{jj} <$ 110 GeV. The dijet transverse momentum distribution for the HR after the dilepton p_T requirement is applied is shown in figure 5.5, with the associated ROC.

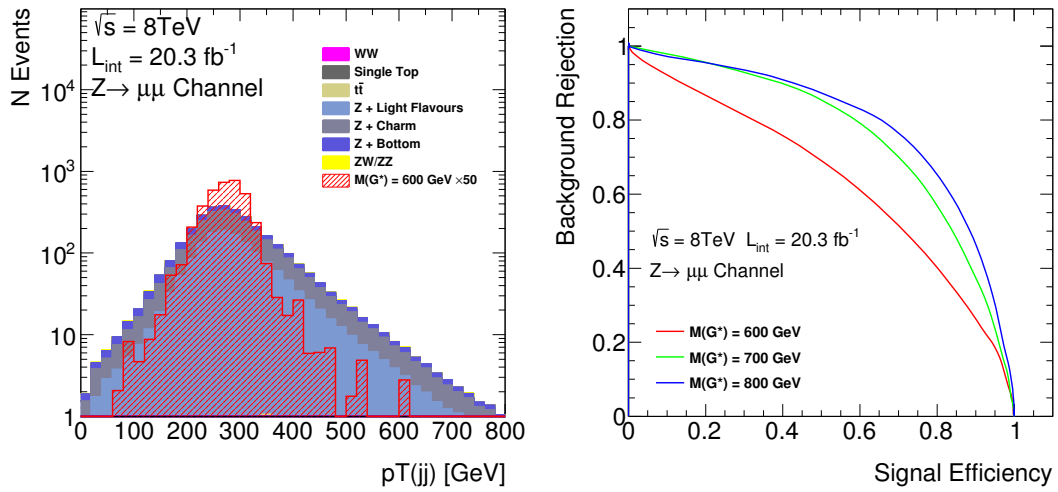

Figure 5.5: The dijet p_T distribution for the muon HR (left), and the associated ROC curves (right), after the p_T^{ll} requirement is applied.

Merged region: The transverse momentum of the dilepton system must satisfy, $p_T^{ll} > 400$ GeV. The large-R jet with the highest transverse momentum is required to satisfy, $p_T^J > 400$ GeV. The mass of the large-R jet must be within the window, 70 GeV $< m_J <$ 110 GeV, and the momentum balance must satisfy, $\sqrt{y_f} > 0.45$. The distribution of the dilepton transverse momentum in the MR is shown with the associated ROC in figure 5.6.

In order to maintain statistical independence between the selection regions, an event is only considered for the HR selection if it has first failed the MR selection criteria. Similarly the event is only considered for the LR selection if it has failed both the MR and HR selection criteria. The sensitivity of each signal region after all selection criteria are applied is summarised in figure 5.7. The ratios S/B and $S/\sqrt{B}$ are shown, where S is the number of signal events, and B is the number of background events. The signal regions are optimised to have good sensitivity

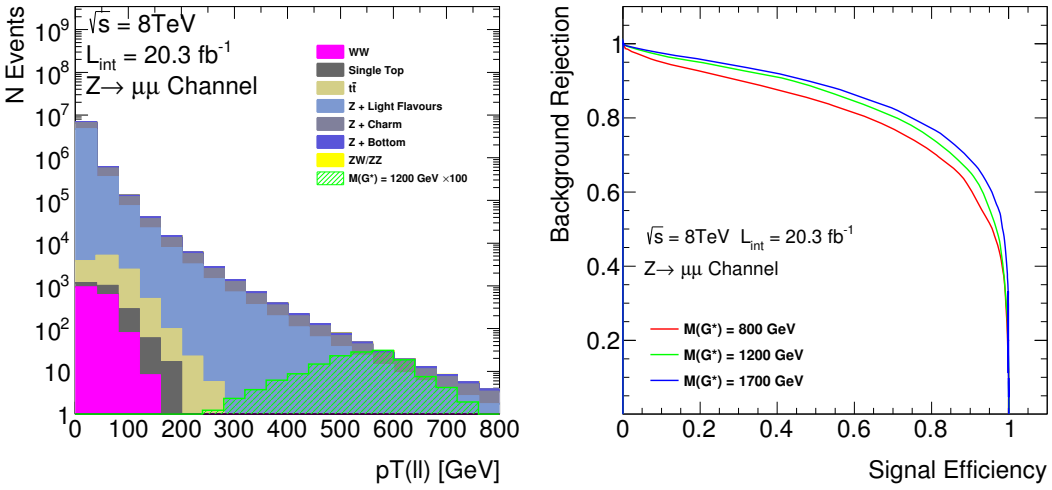

Figure 5.6: The di-muon p_T distribution for the MR (left), and the associated ROC curves (right).

across a large range of signal masses. The LR is the most sensitive region for a signal mass below 500 GeV and the MR is the most sensitive region for signal mass above 800 GeV. The HR is the most sensitive region for intermediate signal masses. The acceptance of the three selection regions and their union is shown in figure 5.8 for both the electron and muon channels. A high acceptance is achieved for signal masses above ≈ 600 GeV, and is maintained to high signal masses.

5.6 Signal Samples

Signal samples for both the bulk RS graviton and EGM W' boson are composed of events generated through the Monte Carlo (MC) method. These are generated for signal pole masses between 300 GeV and 2000 GeV.

The bulk RS graviton samples are generated using CalcHEP3.2 [81], with the `CTEQ6L1` PDF set. The decay of the graviton into two Z bosons is performed by CalcHEP, keeping all spin information. The subsequent parton showering and hadronisation are performed by Pythia8 [82]. Between 300 GeV and 1000 GeV, samples are produced with 50 GeV mass steps. A mass step of 100 GeV is used

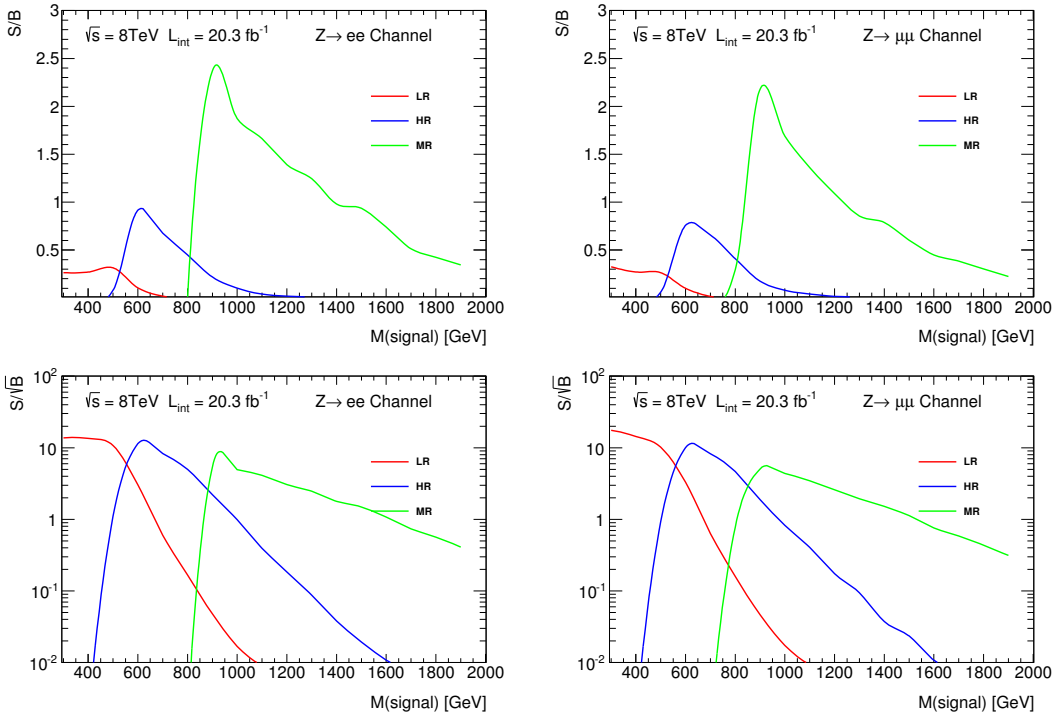

Figure 5.7: The S/B (top), and $S/\sqrt{B}$ (bottom), for the EGM W' boson in the electron (left) and muon (right) channels.

for samples produced between 1000 GeV and 2000 GeV.

The EGM W' boson samples are generated using PYTHIA8, including the parton shower and hadronisation, with the `MSTW20080LO` PDF set. Samples are generated through the entire 300 GeV to 2000 GeV range with 100 GeV mass steps. The production is performed at Leading Order (LO), and an NNLO k-factor is applied. The k-factor was originally derived for the $W' \to l\nu$ process and was adapted to $W' \to WZ$ by the $\ell\nu\ell'\ell'$ channel [83]. The effect of the k-factor on the signal acceptance for the $\ell\ell qq$ channel is negligible. Though the k-factor is a function of resonance mass, the variation is sufficiently small to allow the application of a single k-factor to the each signal distribution, rather than applying the factor on an event by event case.

For both the bulk RS graviton and EGM W' boson samples, the factorisation and renormalisation scales are set to the generated resonance mass. A summary

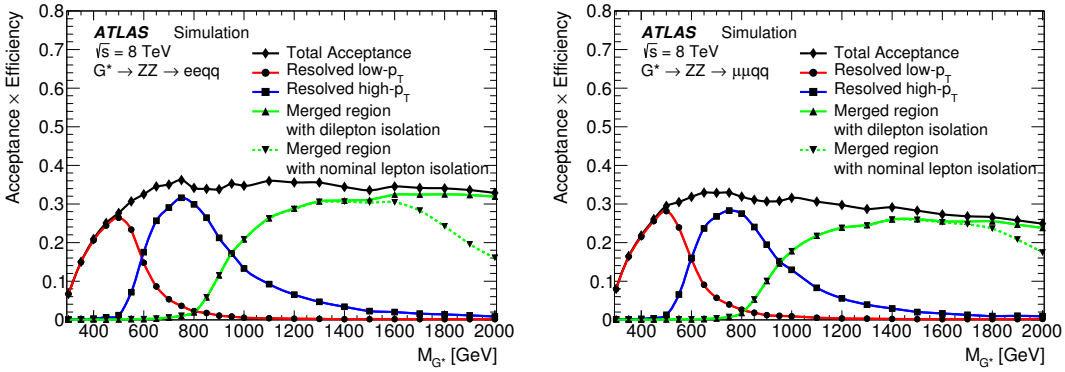

Figure 5.8: Bulk RS graviton acceptance times efficiency for the LR, HR and MR for the electron (left) and muon (right) channels. The MR is shown for both the nominal and dilepton isolation criteria, showing an improvement for signal masses above 1.5 TeV.

of the generated signal cross-sections is given in table 5.1.

Table 5.1: A summary of the cross-sections for the bulk RS graviton and the EGM W' boson, along with the NNLO k-factors applied to the EGM samples.

Mass [GeV]	Graviton $\sigma \times B$ [pb]	W' $\sigma_{\mathrm{LO}} \times B$ [pb]	W' NNLO k-factor
300	1.34E+01	2.42E+01	1.31
400	2.56E+00	8.02E+00	1.31
500	5.40E-01	3.20E+00	1.30
600	1.57E-01	1.48E+00	1.29
700	5.62E-02	7.61E-01	1.28
800	2.31E-02	4.22E-01	1.27
900	1.04E-02	2.47E-01	1.26
1000	5.07E-03	1.51E-01	1.25
1100	2.60E-03	9.50E-02	1.24
1200	1.39E-03	6.14E-02	1.23
1300	7.72E-04	4.06E-02	1.23
1400	4.40E-04	2.72E-02	1.22
1500	2.57E-04	1.85E-02	1.21
1600	1.53E-04	1.27E-02	1.21
1700	9.32E-05	8.86E-03	1.20
1800	5.75E-05	6.22E-03	1.19
1900	3.59E-05	4.41E-03	1.18
2000	2.27E-05	3.14E-03	1.18

5.7 Background Estimation

The background is dominated by Z+jets events. There are additional contributions from diboson and top quark production, with top quark backgrounds becoming negligible at high mass. Contributions from W+jets and QCD multi-jet backgrounds are shown to be negligible. All of the background samples are generated using MC simulation, except for the QCD multi-jet sample, which uses data driven methods. The MC samples are generated using ATLAS approved generator settings, and the dominant Z+jets background is validated through comparison to control regions.

The Z+jets background is simulated using the multi-leg LO perturbative QCD matrix element generator, SHERPA [84] with the `CT10` PDF set. This background is further subdivided into events containing Z bosons and either light flavour, charm or bottom quarks. These samples are simulated independently, but are collectively referred to as the Z+jets sample. To reduce the processing time for producing the Z+jets background, generator criteria are imposed, which suppress the production of events with $m_{ll} < 40$ GeV as this region is not used in the analysis. The $t\bar{t}$, Wt, and s-channel single top quark background processes are generated using MC@NLO [85], with the `CT10` PDF set. The subsequent hadronisation is performed by HERWIG [86], and the underlying events by JIMMY [87]. For t-channel single top quark production, ACERMC [88] with the `CTEQ6L1` PDF set is used to generate the event, and PYTHIA performs the hadronisation. Diboson events are simulated using HERWIG with the `CTEQ6L1` PDF set, and W+jets events are simulated using SHERPA. A summary of the generators and cross-sections used for the MC backgrounds is given in table 5.2.

The QCD multi-jet background is generated using a combination of MC and data driven techniques. For the electron channels, the multi-jet control sample is obtained from data by requiring two electrons that pass the Medium++ but

Table 5.2: A short summary of the cross-sections and event generators employed for each of the background processes. Single top quark samples resulting from s-channel (t-channel) production are denoted as tb (tqb).

Process	Generator	Cross Section
W+jets	SHERPA	11.9 nb
Z+jets	SHERPA	1.21 nb
$t\bar{t}$	MC@NLO	253 pb [89]
Single top (tqb, tW)	MC@NLO	1.83, 22.4 pb [89]
Single top (tb)	ACERMC	28.4 pb
Diboson (WW, WZ, ZZ)	HERWIG	20.6, 4.71, 2.24 pb

fail the Tight++ quality criteria. The multi-jet control sample for the muon channel is obtained by inverting the requirement placed on the transverse impact parameter. The MC background samples described above are used to verify that the contributions of real leptons to these regions are small. These small contributions are subtracted from the multi-jet samples.

The normalisation of the multi-jet control sample is obtained by performing a Maximum Likelihood (ML) fit. The MC background and the multi-jet control sample are fitted over the dilepton mass spectrum for 40 GeV $< m_{ll} <$ 200 GeV. The results of the fits, shown in figure 5.9, estimate the multi-jet background within the dilepton mass region 66 GeV $< m_{ll} <$ 116 GeV, to be much less than 1% for both lepton channels. The deficit in simulated events below 40 GeV is the result of the criteria placed on Z+jet events to optimise processor time. The sub-optimal residuals observed in the dilepton mass spectra are attributed to the modelling of the Z+jets background. A correction is applied to the Z+jets background, as described in section 5.9.1.

5.8 Background Validation

Control regions are defined for the purpose of validating the background estimation. These are defined in order to duplicate the signal region kinematics as closely

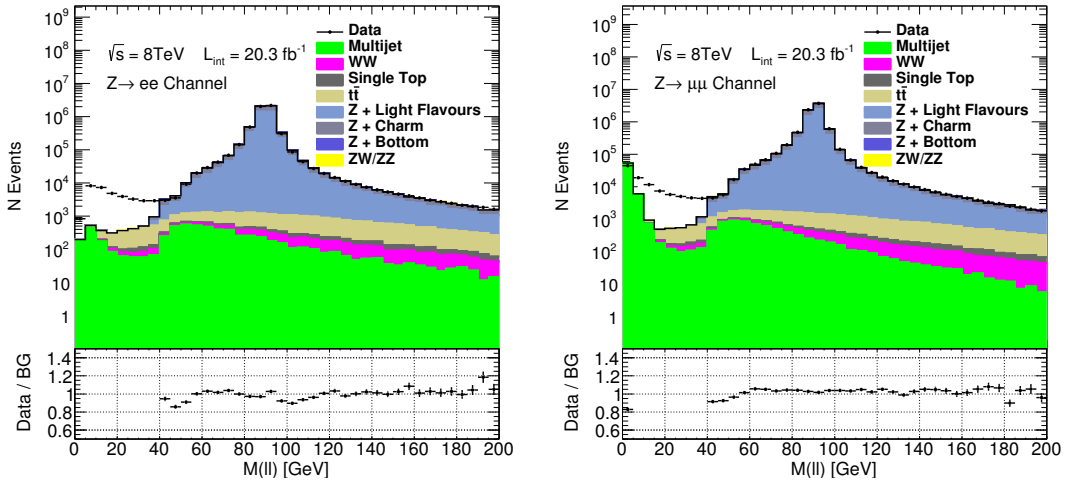

Figure 5.9: The dilepton mass distributions of all background samples for the electron (left) and muon (right) selections. The backgrounds are fit to data for the purpose of determining the normalisation of the multi-jet background.

as possible, while removing any signal contamination. This is performed by inverting the mass windows on the hadronically decaying boson, thus creating two side band regions for each signal region, the high control region ($m_{jj} > 110$ GeV or $m_J > 110$ GeV) and the low control region ($m_{jj} < 70$ GeV or $m_J < 70$ GeV). Given the three selection regions, and the two lepton flavours, there are a total of 12 control regions.

The control region for the reconstructed 3-body (MR), and 4-body (LR and HR) mass spectra are compared in figure 5.10, where the high and low sideband regions and the lepton flavours have been combined. The simulated background models the data well; however, there are small disagreements in both normalisation and shape. Corrections are applied to the Z+jets backgrounds to account for these discrepancies as described in section 5.9.1.

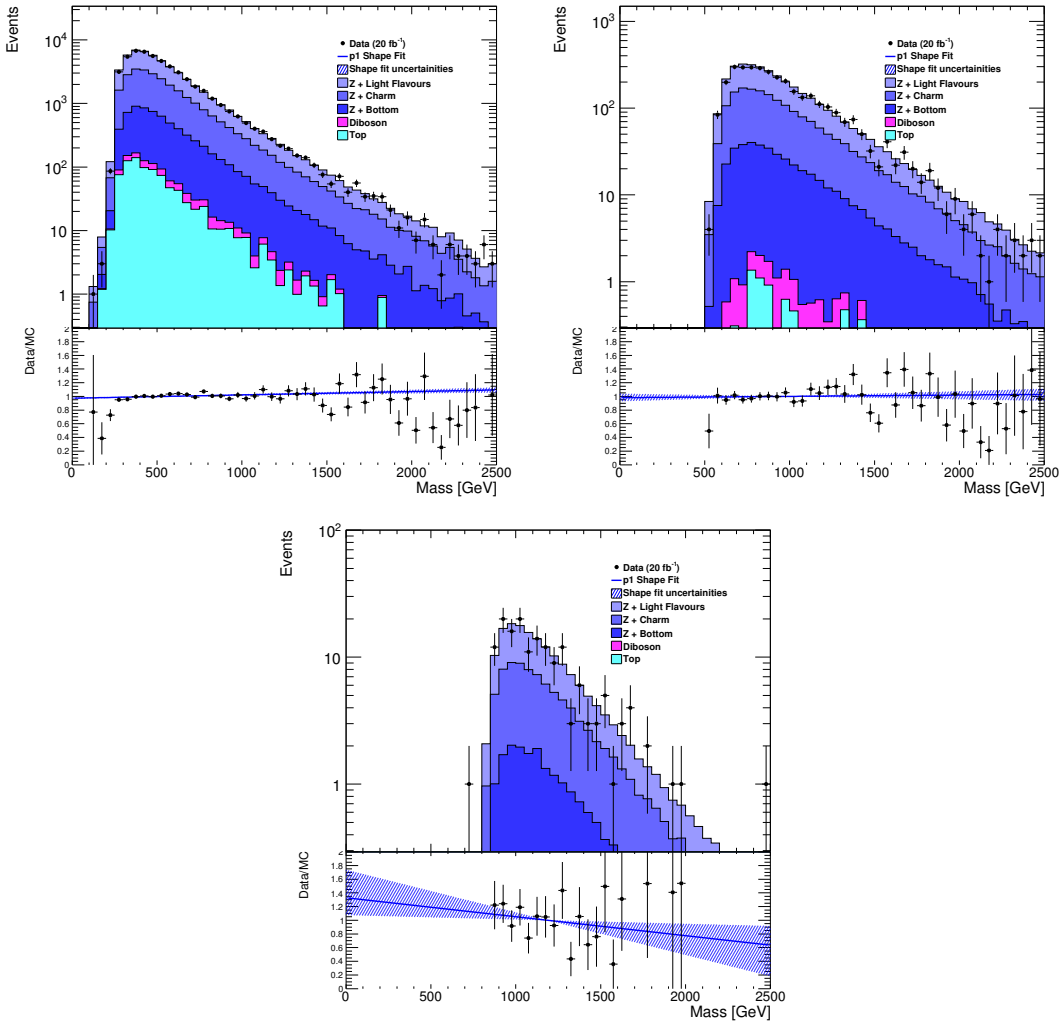

Figure 5.10: The 4-body mass m_{lljj} for the LR (top left), HR (top right) and the 3-body mass m_{llJ} for the MR (bottom) distributions for the m_{jj} and m_J side band control regions. The bottom part of each plot shows the ratio of data to background. The results of the linear fits applied to the Z+jets samples are shown as blue lines, and the fit uncertainties as hatched areas.

5.9 Systematic Uncertainty Estimations

Limited knowledge of both theoretical and experimental factors that affect the differential distributions of final state objects and normalisations are accounted for by the introduction of systematic uncertainties. The systematic uncertainties important to the analysis are discussed below; however, not all those discussed were used in the search and limit setting procedures. The removal of negligibly small systematics is discussed in section 5.13.

5.9.1 Z+jets Background Constraint

In order to account for the sub-optimal residuals present in figure 5.9 and 5.10, normalisation and shape corrections are applied to the Z+jets background. All of the MC background samples are subtracted from the control region data, with the exception of the Z+jets background. The Z+jets background is subsequently scaled to agree with this sample.

The normalisation correction is calculated from the low and high mass control regions separately, and from their combination. The integral of the Z+jets is scaled to that of the combined control region for each of the selection regions, subdivided by lepton flavour. The uncertainty of the correction originates from the finite statistics of the control regions. If the normalisation calculated from the low and high mass control regions are consistent, then the uncertainty on the normalisation applied to the Z+jets background derived purely from the statistical uncertainty. This is the case for the HR and MR. In the instance that the normalisation calculated from the low and high mass control regions differ from each other significantly compared with their statistical uncertainties, the uncertainty on the normalisation applied to the Z+jets sample is taken to be the maximum difference between the applied correction and that derived from the separate low and high mass control regions. This is the case for the LR. Through

these methods of estimating uncertainty, a conservative uncertainty is applied, which is limited by the data statistics in the sideband regions.

The variation in shape is not associated to the leptonic components of the event, so the shape is fitted in three control regions, where the low and high mass sidebands and lepton flavours are combined. A linear shape correction is applied to the invariant mass distribution with the constraint that the normalisation of the Z+jets sample is fixed, so as to maintain independence between the shape and normalisation corrections. The uncertainty of the shape correction is taken to be the fit uncertainty resulting from the statistical uncertainties of the control regions.

A summary of the normalisation and shape corrections applied to the Z+jets samples in each region is given in figure 5.11. The uncertainties of the scaling of the normalisation (referred to as `ZjetsBGModelSlope`) and shape (referred to as `ZjetsBGModel`) of the Z+jets samples are the dominant uncertainties on the background prediction. The fitting of the normalisation and shape of the Z+jets background effectively constrain the background prediction, and so any potential modelling uncertainties on this background are now not applicable. Subsequently, the only remaining uncertainties applicable to the Z+jets background are those derived from the process of fitting the background to the sideband regions.

5.9.2 Electrons

Correction factors are applied to the electron triggers and reconstruction efficiencies as functions of η and E_T, derived from $Z \to ee$ events. Uncertainties are derived for these correction factors (`TRIG`, `RECO`) using the method described in reference [57]. The uncertainty of the energy scale and resolution of the electron candidates is accounted for by applying a smearing to the energy of the electron candidates as a function of η. These scale (`ElecLES`) and resolution (`ElecLER`) uncertainties are found to be 1% and less than 1%, respectively. These uncer-

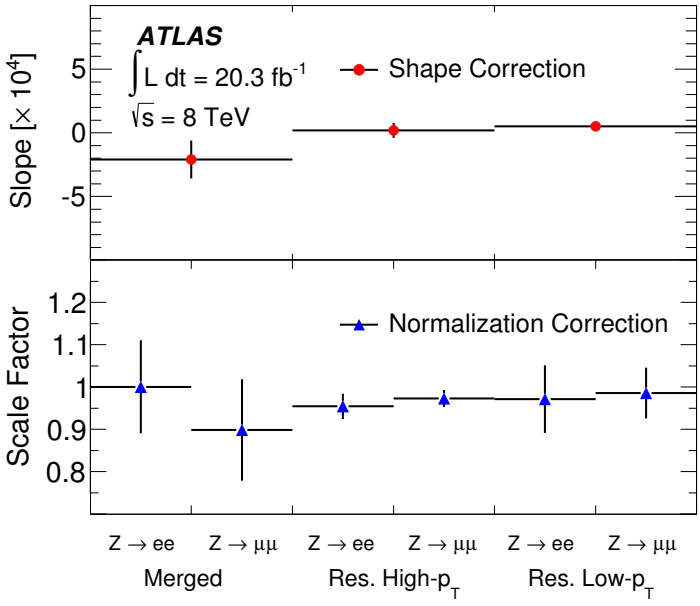

Figure 5.11: The gradient of the linear fit for each of the three control regions (top), and the derived normalisation scale factors for each of the three control regions subdivided by lepton flavour (bottom).

tainties affect the signal and sub-dominant top and diboson background samples.

5.9.3 Muons

Correction factors are applied to the triggers, determined from $Z \to \mu\mu$ events as a function of η and ϕ, as described in reference [90]. A correction factor is applied to the muons reconstructed in MC to account for the reconstruction efficiencies, and is derived from $Z \to \mu\mu$ events. The uncertainty on this correction factor (`MuonID`) is given in reference [91]. The uncertainty on the transverse momentum of the muons is accounted for by applying a smearing to the reconstructed muons, separately in the ID and MS. The combined effect of these uncertainties (`MuonLES`) is approximately 1%, and affects the signal and sub-dominant background samples.

5.9.4 Small-R Jets

The uncertainties associated to the Jet Energy Scale (JES) of the small-R jets used in the LR and HR are determined from the jet response using MC samples [92]. Conditions such as the hadronic shower model are varied, and uncertainties calculated using γ+jets, Z+jets and multi-jet events. There are a large number of systematic uncertainties, which are parametrised into terms that are considered uncorrelated:

Closure: Required for MC samples with detector response modelled by ATLFAST-II [93] to account for the non-closure of the simulation. Non-closure of the sample is defined as the difference present at low p_T between the simulation and unity after JES corrections are applied. (1 parameter: `JESClosure`)

Detector: The uncertainty in the model of the detector and its response. (3 parameters: `JESDetector1`, `JESDetector2`, `JESDetector3`)

η Intercalibration: The uncertainty derived from balancing the momenta of jets recoiling from Z boson production. (2 parameters: `JESEtaInter1`, `JESEtaInter2`)

Flavour Response: The uncertainty in flavour response and composition. (2 parameters: `JESFlavComp`, `JESFlavResp`)

Mixed: The combination of detector, modelling and detector based uncertainties. (2 parameters: `JESMixed1`, `JESMixed2`)

Modelling: The theoretical and modelling uncertainties in the MC. (4 parameters: `JESModelling1`, `JESModelling2`, `JESModelling3`, `JESModelling4`)

Pileup: The uncertainty on the effects of pileup on the jet response. (4 parameters: `JESMuOff`, `JESNPVOff`, `JESPileupPt`, `JESRho`)

Single-hadron: The uncertainty in the single-hadron response at high p_T. (1 parameter: `JESSinglePart`)

Statistical: Due to the statistical uncertainty on the derivation of the energy scale. (3 parameters: `JESStatMeth1`, `JESStatMeth2`, `JESStatMeth3`)

Uncertainties on the Jet Energy Resolution (JER) (`JER`) are determined in-situ using the dijet p_T balance and bisector techniques, which both give consistent results [94]. These uncertainties only affect the LR and HR, in which the small-R jets are used. Due to the constraint placed on the Z+jets sample, the effect on the background prediction is negligible, and the effects on the signal samples are of order 1% or less.

5.9.5 Large-R Jets

Uncertainties on the large-R jets due to JES (`RMDJES`), Jet Mass Scale (JMS) (`RMDJMS`), and momentum balance $\sqrt{y_f}$ (`RMDYS`), are derived through the use of a double ratio method [65]. For a given quantity the average ratio of the track jet to the calorimeter jet is calculated. The comparison of these ratios is made between data and MC. Any deviation from unity is considered a systematic uncertainty. This results in an uncertainty of 2% and 3% on the JES and JMS, and 2% on the momentum balance.

Studies of the W boson mass peak in W+jets data indicate that both the peak location and shape are well described by MC. A similar agreement is seen for the momentum balance resolution in multi-jet events. A 20% uncertainty is applied to the JER (`RMDJER`), Jet Mass Resolution (JMR) (`RMDJMR`) and momentum balance resolution (`RMDYR`) in accordance with recommendations from the jet substructure group [95].

5.9.6 Additional Uncertainties

There exist tile modules in the hadronic calorimeter that are intermittently or permanently unusable due to a range of problems. Corrections are applied to jets that are reconstructed close to these modules, but perform poorly for high p_T jets [96]. The effect is small in the HR, and negligible in the LR and MR. In the HR a 2% uncertainty is applied to the signal acceptance (`BCH`).

The luminosity uncertainty for the 2012 data taking period is estimated to be 2.8% (`Lumi`).

The uncertainty of the signal acceptance due to the PDF (`PDF`) set is determined through the generation of additional signal samples using modified PDF models. The nominal EGM W' boson samples are generated using the `MSTW2008LO` PDF set. The `MSTW2008LO` PDF set contains 20 error sets which parametrise the uncertainty associated with its derivation. The acceptance is compared between the nominal and fluctuated sets, and the maximum variation taken as the acceptance uncertainty. The nominal bulk RS graviton samples are generated using the `CTEQ6L1` PDF, and compared against equivalent samples generated using `MSTW2008LO`, a more recent LO PDF set. The maximum variance of the acceptance between the two PDFs is taken. The total acceptance uncertainty due to the PDF set on the RS graviton samples is taken to be the quadrature sum of the two recorded variances. Dependent on the mass of the signal samples, the effect is found to be between 1% and 2%.

The quantity of Initial and Final State Radiation (ISR/FSR) (`ISRFSR`) is tunable in MC by a number of parameters. Signal samples with varying levels of ISR/FSR are generated using Pythia8. The acceptance of these samples is compared with that of the nominal at truth level. The variation was found to be approximately constant for all mass points and signal regions, and the maximum variation of 5% is taken as a constant uncertainty applied to all signal samples.

At a centre of mass energy of $\sqrt{s} = 8$ TeV, the beam energy was measured to

be $3988 \pm 5(\text{stat}) \pm 26(\text{syst})$ GeV using p-Pb runs in January-February 2013 [97]. Signal samples are generated using a modified beam energy of ± 40 GeV. The effect on the acceptance at truth level is found to be consistent with unity, and an uncertainty of 1% is applied (`LHCBeam`).

5.10 Binning Optimisation

The statistical methods used to analyse the mass spectra are capable of developing instabilities if there are bins which contain no background prediction. In addition, the presence of a large number of bins results in the requirement of large amounts of processor time. To reduce the processor time required, and to avoid the development of instabilities, wider bins may be used. This can be problematic as it results in a reduction in sensitivity. To obtain a suitable binning, advantage was taken of the the fact that, for both the bulk RS graviton model and the EGM model, the resonance width increases with the pole mass. This effect is amplified due to the energy and momentum dependence of the calorimeter and tracker resolutions.

The invariant mass distributions were rebinned following an exponential function to ensure that the peak is always reconstructed within the same number of bins. The reconstructed m_{lljj} (LR and HR) and m_{llJ} (MR) distributions for the RS graviton and EGM W' boson are shown in figure 5.12 for a range of signal pole masses.

To determine the binning, each signal sample is fitted with a Gaussian template. The extracted signal widths are plotted against the resonance pole mass in figure 5.13. From this the bin width w, for a given reconstructed mass m, is given by

$$w = 1.5 \text{ GeV} \times e^{0.0011m \, + \, 2.9}, \tag{5.2}$$

where the bin edges are rounded to the nearest 10 GeV.

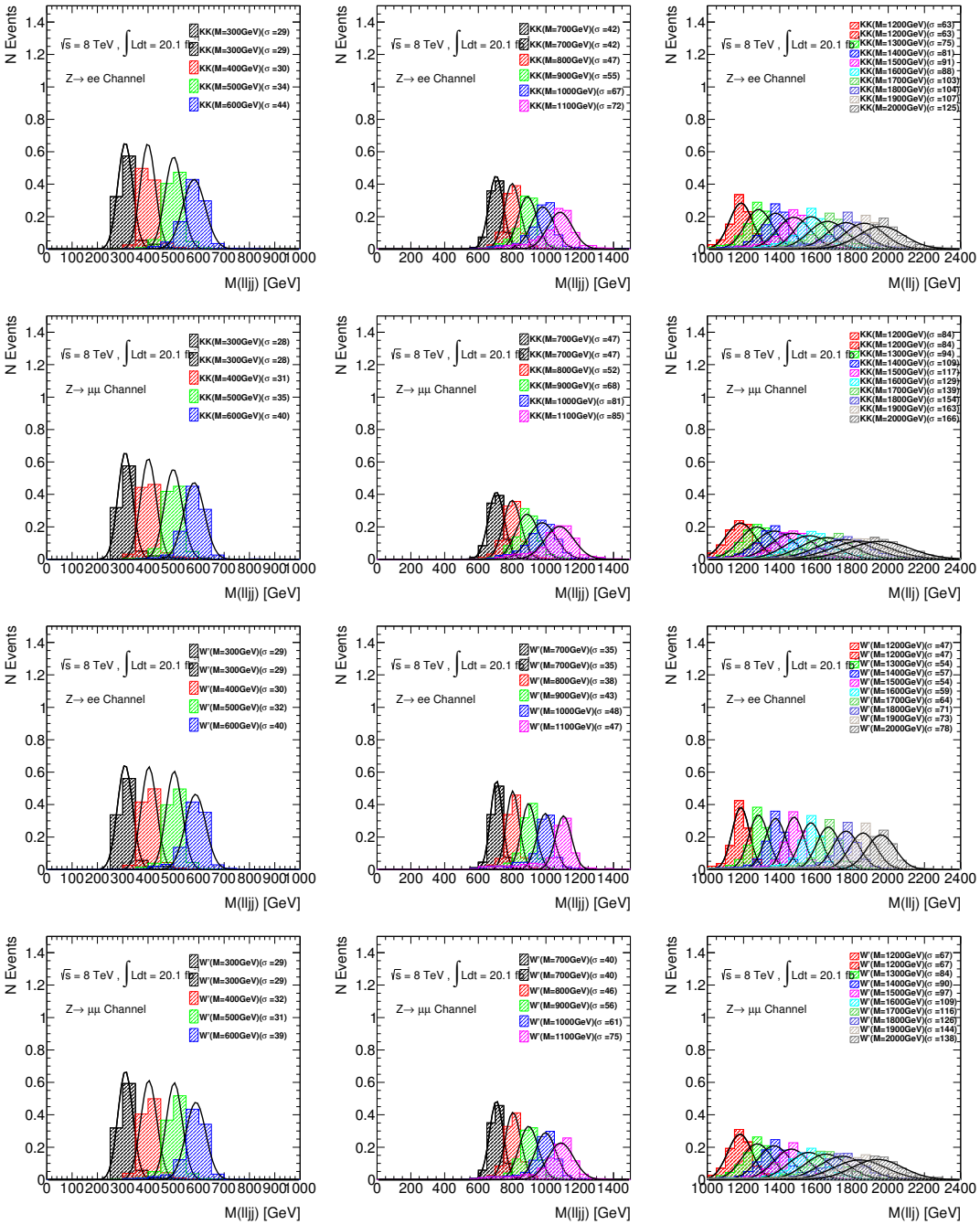

Figure 5.12: The reconstructed mass distribution m_{lljj} for the LR (left) and HR (middle) and m_{llJ} for the MR (right), for the RS graviton (top two rows) and W' boson (bottom two rows).

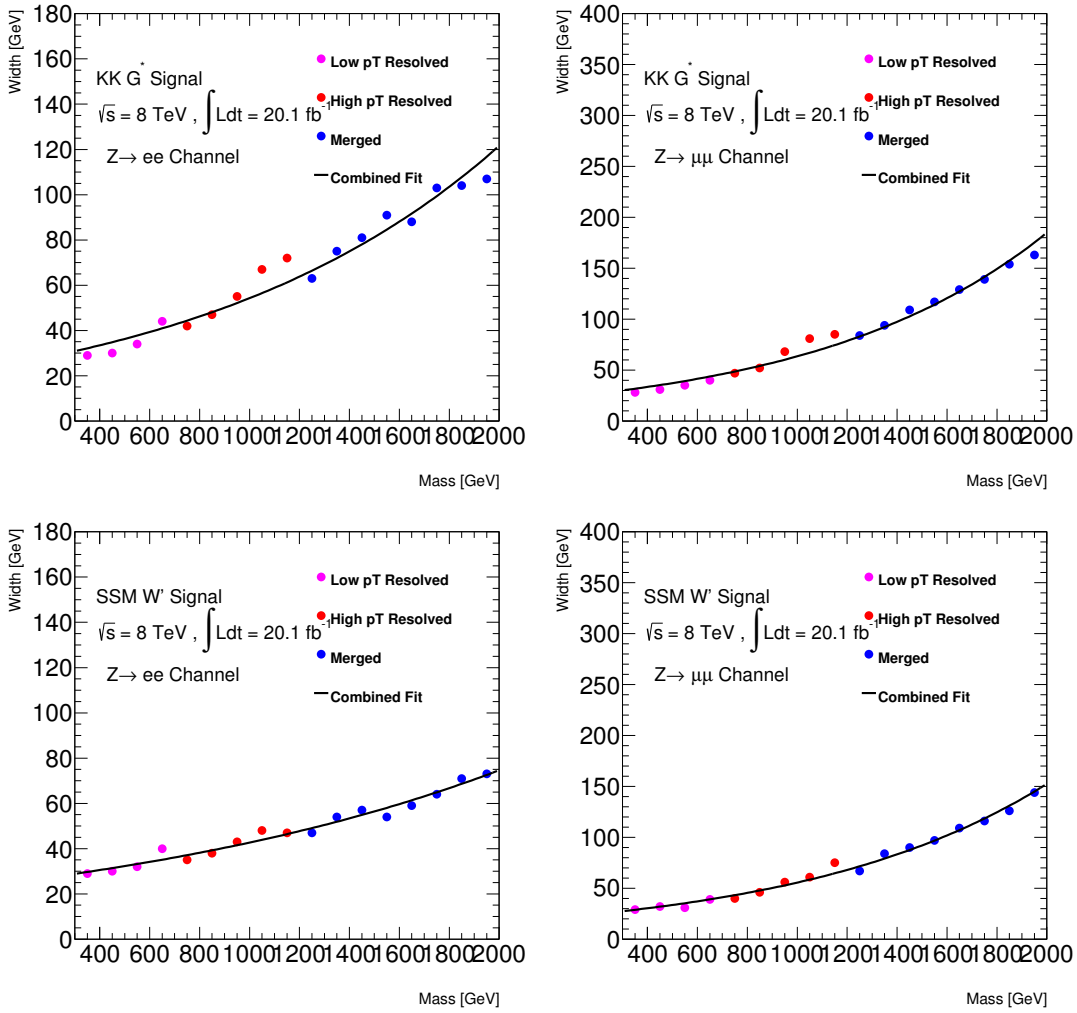

Figure 5.13: The width of a Gaussian fitted to the reconstructed signal mass distribution m_{lljj} (LR and HR) or m_{llJ} (MR) for the RS graviton (top) and W' boson (bottom) in the electron (left) and muon (right) channels.

At high reconstructed masses, the number of background MC events per bin is very small. The exponential binning results in much larger bin widths in the region with the fewest simulated events. In addition, the mass distribution for each region is truncated at high mass and uses an overflow bin. The start of the overflow bin is determined by integrating the mass spectra downwards from 5 TeV until the statistical uncertainty of the summed MC background is less than 60% of the overflow content. An underflow bin is also used, chosen such that the turn on of the signal region is entirely contained within one bin.

This ensures that the bins are everywhere narrow enough to resolve a signal peak, but wide enough the maintain a non-zero background prediction everywhere and minimize the required processor time. Rebinning in this manner has minimal effect on the sensitivity of the extracted results.

5.11 Statistical Procedure

The statistical analysis is performed using binned maximum-likelihood fits to the diboson invariant mass spectra using the standard statistical fitting package RooStats [98].

Systematic uncertainties on the signal and background are accounted for by Nuisance Parameters (NP) in a likelihood function. For each background and signal sample s, a histogram h_s^0, is provided. For a systematic uncertainty p, a pair of histograms, h_{sp}^+ and h_{sp}^-, represent the positive and negative systematic fluctuations. The sample $\eta_{sp}(\alpha_p)$ is defined for the nuisance parameter α_p such that $\eta_{sp}(0) = h_s^0$, and $\eta_{sp}(\pm 1) = h_{sp}^{\pm}$. A Gaussian constraint with mean 0 and width 1 is applied to each nuisance parameter.

The template histograms are based on finite-statistics MC samples, so NP to account for the bin-by-bin statistical uncertainties on the template histograms are introduced using the Barlow-Beeston "lite" method [99]. One nuisance parameter is introduced for each bin in each channel, representing the statistical errors in that bin from each of the components added in quadrature.

5.11.1 Template Morphing

The expected number of events for all values of the NP are interpolated and extrapolated from the nominal and fluctuated histograms provided. A vertical morphing technique is used [100]. The vertical morphing technique is a computationally simple method for interpolating between two binned distributions. Each

bin of the distribution is considered independently, and a parametrisation is created to smoothly change the bin content between the extremal points provided. The same parameter is used for all of the bins, which subsequently transforms the entire distribution. The precise form of this parametrisation is chosen dependent on the application, and can be used to extrapolate beyond the initial distributions.

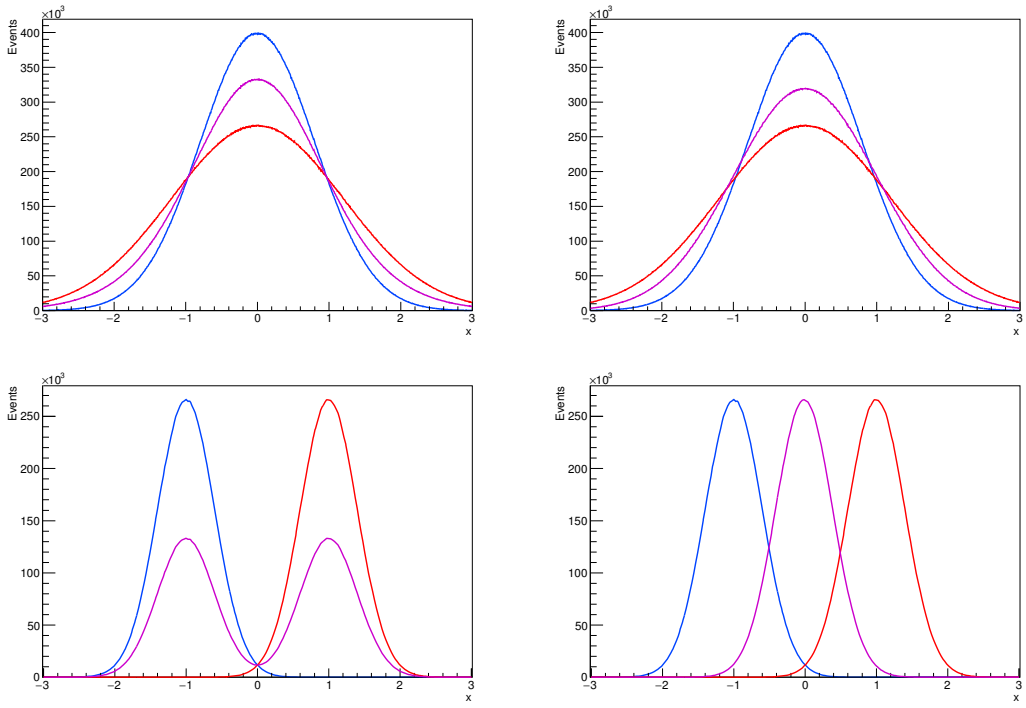

Figure 5.14: Illustration of the behaviour of the linear vertical (left) and integral (right) morphing algorithms with a single nuisance parameter representing either a shape (top) or scale (bottom) uncertainty. The magenta curves are the interpolated distributions half way between the red and blue template distributions. The integral morphing handles both cases correctly, whereas vertical interpolation fails in the instance of a large scale variation.

Vertical morphing is valid for normalisation uncertainties, shape uncertainties, and scale uncertainties with the condition that the scale variation must not be large in comparison to the width of the peak. In the situation where the scale variation is much larger than the peak width, the vertical morphing method is

not valid as shown in figure 5.14. In this instance more sophisticated morphing techniques are necessary, such as integral morphing. Vertical morphing is computationally much quicker than alternative techniques, and for this reason is the preferred choice whenever possible. Within this analysis, all the applied systematic scale uncertainties fall within the region of validity, whereby the horizontal movement is smaller than the reconstructed signal width.

The vertical interpolation method has four possible parametrisations for interpolating and extrapolating the templates: piecewise linear, piecewise exponential, quadratic interpolation with linear extrapolation, and polynomial interpolation with exponential extrapolation [101]. An ideal method for this application must have two features. Firstly, the method must ensure that the expected number of events in each bin is never negative. Secondly, the method must ensure that there are no discontinuities in the first order derivative, as a kink can cause difficulties for certain minimisation packages such as MINUIT [102]. Of the four methods, piecewise linear and quadratic interpolation with linear extrapolation both permit negative values for bin content, and piecewise linear and piecewise exponential methods generally generate kinks at $\alpha_p = 0$. The only remaining method, polynomial interpolation with exponential extrapolation, satisfies both criteria for any input.

Using the polynomial interpolation and exponential extrapolation parametrisation, the expected number of events taking all NP into account is given by

$$\eta_s(\alpha) = \prod_{p \in Systs} I_{poly|exp}\left(\alpha_p; h_s^0, h_{sp}^+, h_{sp}^-\right), \tag{5.3}$$

where α is the set of all NP, and

$$I_{poly|exp}\left(\alpha_p; I^0, I^+, I^-\right) = \begin{cases} \left(I^+/I^0\right)^{\alpha_p} & \alpha_p \geq 1, \\ 1 + \sum_{i=1}^{6} a_i \alpha_p & |\alpha_p| < 1, \\ \left(I^-/I^0\right)^{-\alpha_p} & \alpha_p \leq -1. \end{cases} \tag{5.4}$$

The a_i terms are fixed by requiring $\eta_{sp}\left(\pm 1\right) = h_{sp}^{\pm}$, continuity at $d\eta_{sp}/d\alpha_p|_{\alpha_p=\pm 1}$, and that $d^2\eta_{sp}/d\alpha_p^2|_{\alpha_p=\pm 1}$.

5.11.2 Profile Likelihoods

The quantity of signal above the background prediction can be measured through a test statistic which contains all information from the invariant mass spectra [4]. This discriminant is a likelihood ratio, and for a single bin j, from channel i, with predicted signal s_{ij}, background estimation b_{ij}, and data x_{ij}, takes the form

$$\Lambda(x_{ij}) = \frac{L(s_{ij} + b_{ij}|x_{ij})}{L(b_{ij}|x_{ij})}. \tag{5.5}$$

Taking a_{ij} to represent the total number of expected events (either b or $s + b$), the likelihood L is given by

$$L(a_{ij}|x_{ij}) = \frac{a_{ij}^{x_{ij}} e^{-a_{ij}}}{x_{ij}!}. \tag{5.6}$$

In order to take into account multiple bins within a channel, or multiple orthogonal channels, it is possible to create a combined likelihood by taking the product

$$L(\boldsymbol{a}|\boldsymbol{x}) = \prod_{i}^{channels} \prod_{j}^{bins} L(a_{ij}|x_{ij}). \tag{5.7}$$

To measure or set limits on a signal, it is necessary to know the probability p, of a test statistic exceeding the observed value. This p-value can equivalently

be expressed as a significance, Z. Significance is defined such that a variable distributed as a Gaussian function has a probability p of being greater than Z standard deviations away from its mean. It can be calculated using

$$Z = \Phi^{-1}(1 - p), \tag{5.8}$$

where Φ^{-1} is the quantile of the Gaussian function. It is considered that $Z \geq 3$ is an indication of signal existence, and $Z \geq 5$ constitutes a discovery. Exclusion of signal hypotheses is performed using the threshold $p \geq 0.05$, which for a one-sided distribution corresponds to $Z \leq 1.64$.

A profile likelihood is used to calculate limits on the product of the production cross-section and the branching ratio [103]. A profile likelihood is a variation on likelihood ratios, where the signal region data is used to constrain the systematic uncertainties. To search for positive signal two binned likelihood fits are performed, one in which the signal is allowed to float, and one in which the signal is fixed to zero. The likelihood ratio

$$\lambda(\mu) = \frac{L(\mu, \hat{\hat{\theta}}(\mu))}{L(\hat{\mu}, \hat{\theta})}, \tag{5.9}$$

is calculated. Here μ is the signal strength with $\mu = 0$ corresponding to the background only hypothesis, and $\mu = 1$ the nominal signal hypothesis. The statistical and systematic uncertainties are accounted for by a vector of NP, θ. The vector $\hat{\hat{\theta}}(\mu)$ contains the values of the NP that maximises the likelihood L, for the specified μ (conditional likelihood), $\hat{\mu}$ and $\hat{\theta}$ are the signal strength and nuisance parameter values that maximise L (unconditional likelihood). The fit is performed simultaneously over multiple signal regions. Where a systematic uncertainty affects multiple signal regions, a single nuisance parameter is used.

The value of $\lambda(\mu)$ is used to calculate the test statistic

$$q_0 = \begin{cases} -2\ln\lambda(0) & \hat{\mu} \geq 0, \\ 0 & \hat{\mu} < 0, \end{cases} \tag{5.10}$$

from which a p-value is calculated for each mass point to check for deviation from the SM.

To extract limits a second pair of binned ML fits is performed, one in which the signal is allowed to float and one in which the signal is fixed to zero. The likelihood ratio

$$\tilde{\lambda}(\mu) = \begin{cases} \frac{L(\mu,\hat{\hat{\theta}}(\mu))}{L(\hat{\mu},\hat{\theta})} & \hat{\mu} \geq 0, \\ \frac{L(\mu,\hat{\hat{\theta}}(\mu))}{L(0,\hat{\theta}(0))} & \hat{\mu} < 0, \end{cases} \tag{5.11}$$

is used to calculate the test statistic $\tilde{q}(\mu)$, given by

$$\tilde{q}_\mu = \begin{cases} -2\ln\tilde{\lambda}(\mu) & \hat{\mu} \leq \mu, \\ 0 & \hat{\mu} > \mu, \end{cases} \tag{5.12}$$

To extract limits on the signal, the CL_s method is used [4].

For a given analysis, both of these test statistics are used, first measuring the consistency between background only hypothesis and data using q_0, and subsequently extracting exclusion limits using $\tilde{q}_\mu$. Understanding of these test statistics can be furthered by considering the graphical interpretations of the likelihood curves. Example curves are shown in figure 5.15, with varying values of $\hat{\mu}$. The test statistic q_0 is the value of the curve at the interception with the y-axis. The test statistic $\tilde{q}_\mu$ equals the shown curves for $\mu > \hat{mu}$, and zero otherwise. Limits extracted at the 95% CL correspond to the signal strength for which $\tilde{q}_\mu$ exceeds the value of four, as marked in the figure. Note that the definition of $\tilde{\mu}$ ensures that the signal strength required for exclusion is always greater than zero.

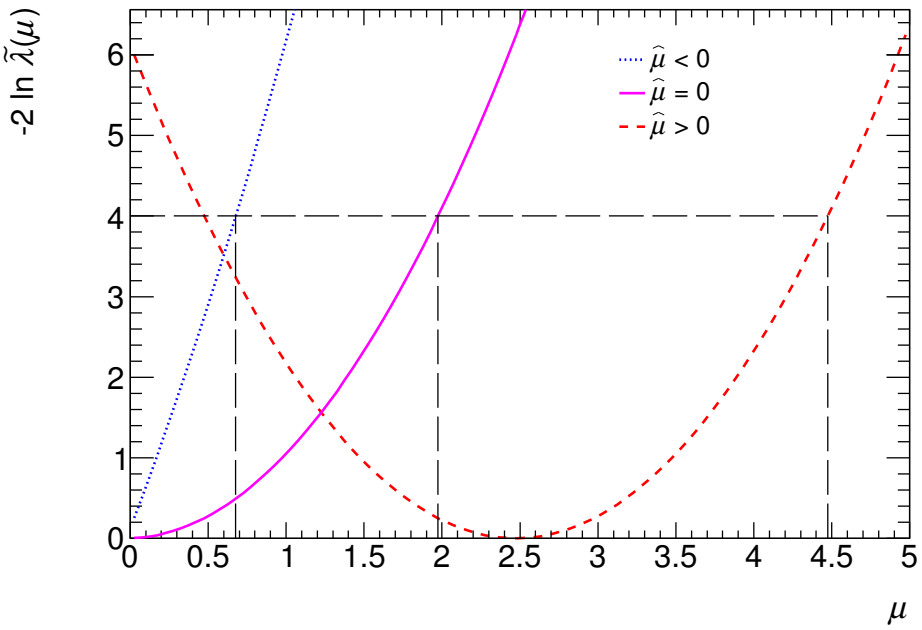

Figure 5.15: Example likelihood curves used to calculate the test statistics described. The black lines are the extracted 95% CL limits.

5.11.3 Asymptotic Method

In order to measure or set limits on a signal, it is necessary to know the probability of a test statistic exceeding the observed value. This p-value is calculated using the Cumulative Distribution Function (CDF) of the statistic. This can be calculated by creating a large number of toy datasets through randomly sampling the NP. This method requires a large amount of computing time and is not always necessary. Instead it is possible to used the Wald approximation

$$-2\ln\lambda(\mu) = \frac{(\mu-\hat{\mu})^2}{\sigma^2} + \mathcal{O}(1/\sqrt{N}), \tag{5.13}$$

where $\hat{\mu}$ follows a Gaussian distribution centred on μ', with standard deviation σ and data sample size N. In the large sample limit, it is possible to calculate the distribution exactly, and the approximation holds for fairly small sample sizes.

5.11.3.1 Discovery

The Wald approximation given in equation 5.13 gives

$$\sigma^2 \approx \frac{(\mu - \mu')^2}{q_\mu}. \tag{5.14}$$

Given that for discovery $\mu = 0$ is tested, this simplifies to

$$\sigma^2 \approx \frac{\mu'^2}{q_0}, \tag{5.15}$$

and the test statistic given in equation 5.10 reduces to

$$q_0 \approx \begin{cases} \hat{\mu}^2/\sigma^2 & \hat{\mu} \geq 0, \\ 0 & \hat{\mu} < 0. \end{cases} \tag{5.16}$$

Using this approximation, the Probability Distribution Function (PDF) of q_0 has the form

$$f(q_0|0) = \frac{1}{2}\delta(q_0) + \frac{1}{2\sqrt{2\pi q_0}} e^{-\frac{q_0}{2}}, \tag{5.17}$$

giving the CDF

$$F(q_0|0) = \Phi(\sqrt{q_0}). \tag{5.18}$$

The p-value for the test statistic can thus be calculated using

$$p_0 = 1 - F(q_0|0), \tag{5.19}$$

or equivalently, converting to significance

$$Z_0 = \Phi^{-1}(1 - p_0) = \sqrt{q_0}. \tag{5.20}$$

5.11.3.2 Exclusion

As in the case of the discovery test statistic, the Wald approximation in equation 5.13 gives

$$\sigma^2 \approx \frac{(\mu - \mu')^2}{\tilde{q}_\mu}. \tag{5.21}$$

Given that for exclusion, $\mu' = 0$ is tested, this simplifies to

$$\sigma^2 \approx \frac{\mu^2}{\tilde{q}_\mu}, \tag{5.22}$$

and the test statistic given in 5.12 reduces to

$$\tilde{q}_\mu \approx \begin{cases} \frac{\mu^2}{\sigma^2} - \frac{2\mu\hat{\mu}}{\sigma^2} & \hat{\mu} < 0, \\ \frac{(\mu-\hat{\mu})^2}{\sigma^2} & 0 \leq \hat{\mu} \leq \mu, \\ 0 & \hat{\mu} > \mu. \end{cases} \tag{5.23}$$

Using this approximation, the PDF of $\tilde{q}_\mu$ has the form

$$f(\tilde{q}_\mu|\mu) = \frac{1}{2}\delta(\tilde{q}_\mu) + \begin{cases} \frac{1}{2\sqrt{2\pi\tilde{q}_\mu}} e^{-\frac{\tilde{q}_\mu}{2}} & 0 < \tilde{q}_\mu \leq \mu^2/\sigma^2, \\ \frac{1}{2\sqrt{2\pi}(\mu/\sigma)} e^{-\frac{\left(\tilde{q}_\mu + \mu^2/\sigma^2\right)^2}{8(\mu/\sigma)^2}} & \tilde{q}_\mu > \mu^2/\sigma^2. \end{cases} \tag{5.24}$$

giving the CDF

$$F(\tilde{q}_\mu|\mu) = \begin{cases} \Phi\left(\sqrt{\tilde{q}_\mu}\right) & 0 < \tilde{q}_\mu \leq \mu^2/\sigma^2, \\ \Phi\left(\frac{\tilde{q}_\mu + \mu^2/\sigma^2}{2\mu/\sigma}\right) & \tilde{q}_\mu > \mu^2/\sigma^2. \end{cases} \tag{5.25}$$

The p-value for the test statistic can thus be calculated using

$$p_\mu = 1 - F(\tilde{q}_\mu|\mu). \tag{5.26}$$

To set limits at a confidence level of $1-\alpha$, the substitution $p_\mu = \alpha$ is made, and equation 5.26 is solved for μ, giving

$$\mu_{\text{up}} = \hat{\mu} + \sigma\Phi^{-1}(1-\alpha). \tag{5.27}$$

5.12 Signal Region Selection

The profile likelihood is performed simultaneously over multiple signal regions, however not all of the regions are sensitive for each signal mass point. A signal region is only used if it contributes more than 5% of the total signal acceptance. The signal regions used for each mass point of the bulk RS graviton and the EGM W' boson are shown in table 5.3.

The expected limits on cross-section for the low-p_T, high-p_T and merged selection regions and their contributions to the combined limit are shown in figure 5.16, where only statistical uncertainties have been considered.

5.13 Nuisance Parameter Selection

Systematics that are deemed to have a negligible effect on the mass spectra are removed from the statistical analysis. Removing surplus NP reduces the calculation complexity and increases the fit stability. To determine if an uncertainty is significant, two tests are performed. A normalisation uncertainty, p, is only kept for a sample if the normalisation of either h^+_{sp} or h^-_{sp} differs from that of the nominal sample h^0_s, by greater than 0.5 σ, where σ is the statistical uncertainty of the nominal. For shape uncertainties a Kolmogorov-Smirnov (KS) test [104] is performed between the nominal and systematically shifted sample. A shape uncertainty is kept for a particular sample if

$$\min\left[\text{KS}\left(h^0_s, h^+_{sp}\right), \text{KS}\left(h^0_s, h^-_{sp}\right)\right] < 0.1. \tag{5.28}$$

Table 5.3: Selection regions used for each graviton and W' boson mass point in the statistical analysis.

Signal Mass [GeV]	Graviton signal region selection	EGM signal region selection
300	low-p_T	low-p_T
350	low-p_T	-
400	low-p_T	low-p_T
450	low-p_T	-
500	low-p_T	low-p_T
550	low-p_T, high-p_T	-
600	low-p_T, high-p_T	low-p_T, high-p_T
650	low-p_T, high-p_T	-
700	low-p_T, high-p_T	low-p_T, high-p_T
750	low-p_T, high-p_T	-
800	low-p_T, high-p_T, merged	low-p_T, high-p_T
850	low-p_T, high-p_T, merged	-
900	high-p_T, merged	low-p_T, high-p_T, merged
950	high-p_T, merged	-
1000	high-p_T, merged	high-p_T, merged
1100	high-p_T, merged	high-p_T, merged
1200	high-p_T, merged	high-p_T, merged
1300	high-p_T, merged	high-p_T, merged
1400	high-p_T, merged	high-p_T, merged
1500	high-p_T, merged	high-p_T, merged
1600	high-p_T, merged	high-p_T, merged
1700	high-p_T, merged	high-p_T, merged
1800	high-p_T, merged	high-p_T, merged
1900	merged	high-p_T, merged
2000	merged	high-p_T, merged

A summary of the systematics that pass each of these selection criteria is given in table 5.4.

5.14 Effects of Including Systematics

The introduction of systematics to the limit calculation leads to a decreased sensitivity. The degradation in expected sensitivity due to the inclusion of a specific systematic can be calculated in the following way. Initially the expected limit on cross-section when all systematics are applied, σ_{all}, is calculated. The calculation is repeated, omitting the systematic of interest to obtain the expected cross-

Table 5.4: A summary of the systematic uncertainties used in the statistical analysis after small uncertainties have been neglected. A systematic uncertainty that is used as a normalisation uncertainty for at least one background or signal sample is labelled with an *N*, and similarly shape uncertainties that are used for at least one signal or background sample are labelled with an *S*. Systematic uncertainties that were found to not contribute a significant shape or normalisation uncertainty to any signal or background samples are omitted from the table.

Source of	Electron			Muon		
Systematic	LR	HR	MR	LR	HR	MR
ZjetsBGModel	*N*	*N*	*N*	*N*	*N*	*N*
ZjetsBGModelSlope	*S*	*S*	*S*	*S*	*S*	*S*
TRIG	*N*	*N*	*N*	*N*	*N*	*N*
RECO	-	-	-	-	*N*	-
ElecLES	*N*	*N*	*N*	-	-	-
MuonID	-	-	-	-	-	*N*
JER	*NS*	*NS*	-	*NS*	*NS*	-
JESClosure	*N*	-	-	*N*	-	-
JESDetector1	*N*	*NS*	-	*N*	*NS*	-
JESEtaInter1	*N*	*N*	-	*N*	*N*	-
JESFlavComp	*NS*	*NS*	-	*NS*	*NS*	-
JESFlavResp	*NS*	*NS*	-	*NS*	*NS*	-
JESModelling1	*NS*	*N*	-	*NS*	*N*	-
JESModelling2	*N*	-	-	-	-	-
JESRho	*N*	-	-	*N*	*N*	-
RMDJER	-	-	*NS*	-	-	*NS*
RMDJES	-	-	*NS*	-	-	*NS*
RMDJMR	-	-	*N*	-	-	*N*
RMDJMS	-	-	*N*	-	-	*N*
RMDYR	-	-	*N*	-	-	*N*
RMDYS	-	-	*N*	-	-	*N*
BCH	-	*N*	-	-	*N*	-
Lumi	*N*	*N*	*N*	*N*	*N*	*N*
PDF	-	*N*	-	-	-	-
ISRFSR	*N*	*N*	*N*	*N*	*N*	*N*
LHCBeam	-	*N*	-	-	*N*	-

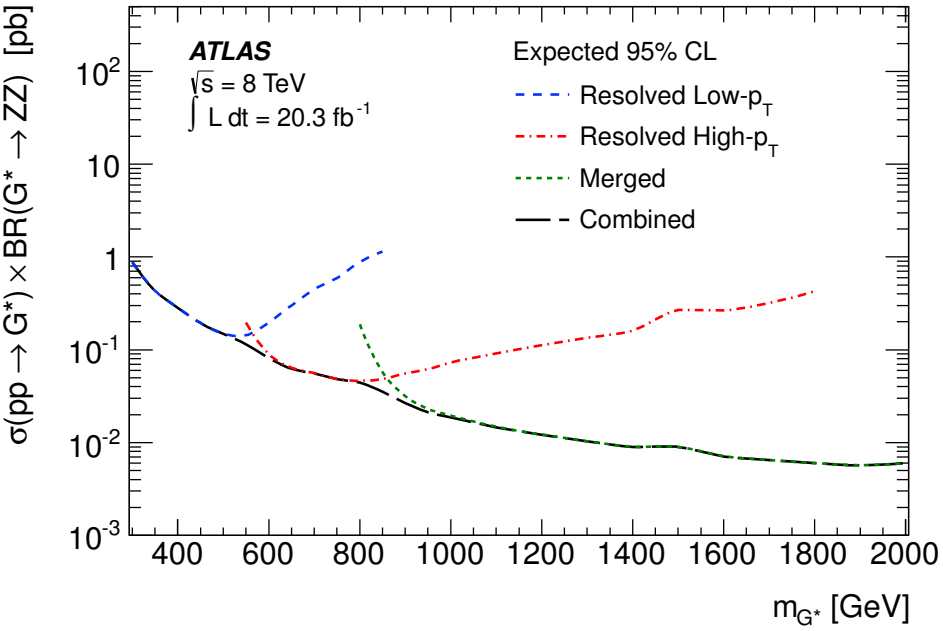

.

Figure 5.16: The expected limit considering only statistical uncertainties for the low-p_T, high-p_T and merged signal regions, and the combination of all three regions. The expected limits of the component signal regions are only displayed for the signal masses where they contribute to the combined limit, as given in table 5.3.

section limit, $\sigma_{\text{all-syst}}$. The effect on the cross-section limit due to this systematic $\Delta\sigma$, is calculated from the subtraction in quadrature

$$\Delta\sigma = \sqrt{\sigma^2_{\text{all}} - \sigma^2_{\text{all-syst}}}. \tag{5.29}$$

The effect of the inclusion of each of the systematic uncertainties considered in this search are shown in figure 5.17, where the sensitivity degradation is defined as $\Delta\sigma/\sigma_{\text{all}}$. The sensitivity degradation resulting from the inclusion of all systematics varies as a function of pole mass between 2% and 18%, and is dominated by the uncertainties related to the modelling of the Z+jets background.

The LR is the most sensitive signal region for 300 GeV test masses. The HR becomes the most sensitive signal region at 600 GeV, and above 900 GeV the

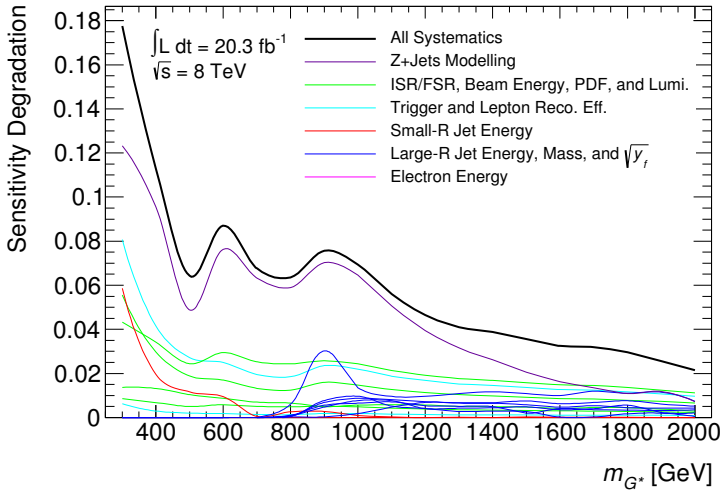

Figure 5.17: The fractional degradation of sensitivity in the expected upper limit on production cross-section times branching ratio of the bulk RS graviton model resulting from the inclusion of systematic uncertainties. Some systematics have been subdivided into multiple lines, each representing an independent component.

MR becomes the most sensitive signal region. At both of the transition regions, when a new signal region becomes dominant, the sensitivity degradation due to the inclusion of systematics increases. In particular this is due to the Z+jets normalisation uncertainty and the large-R jet JES uncertainty.

5.15 Results

5.15.1 Unblinded Signal Region

After using MC to optimise the analysis search strategy, the data in the signal region are unblinded, and consistency is checked between the data and simulated background. The comparison of the invariant mass spectra for the electron and muon channels in the low-p_T, high-p_T and merged regions are shown in figure 5.18 and table 5.5. There are no significant deviations observed above the background prediction that cannot be attributed to statistical or systematic fluctuations.

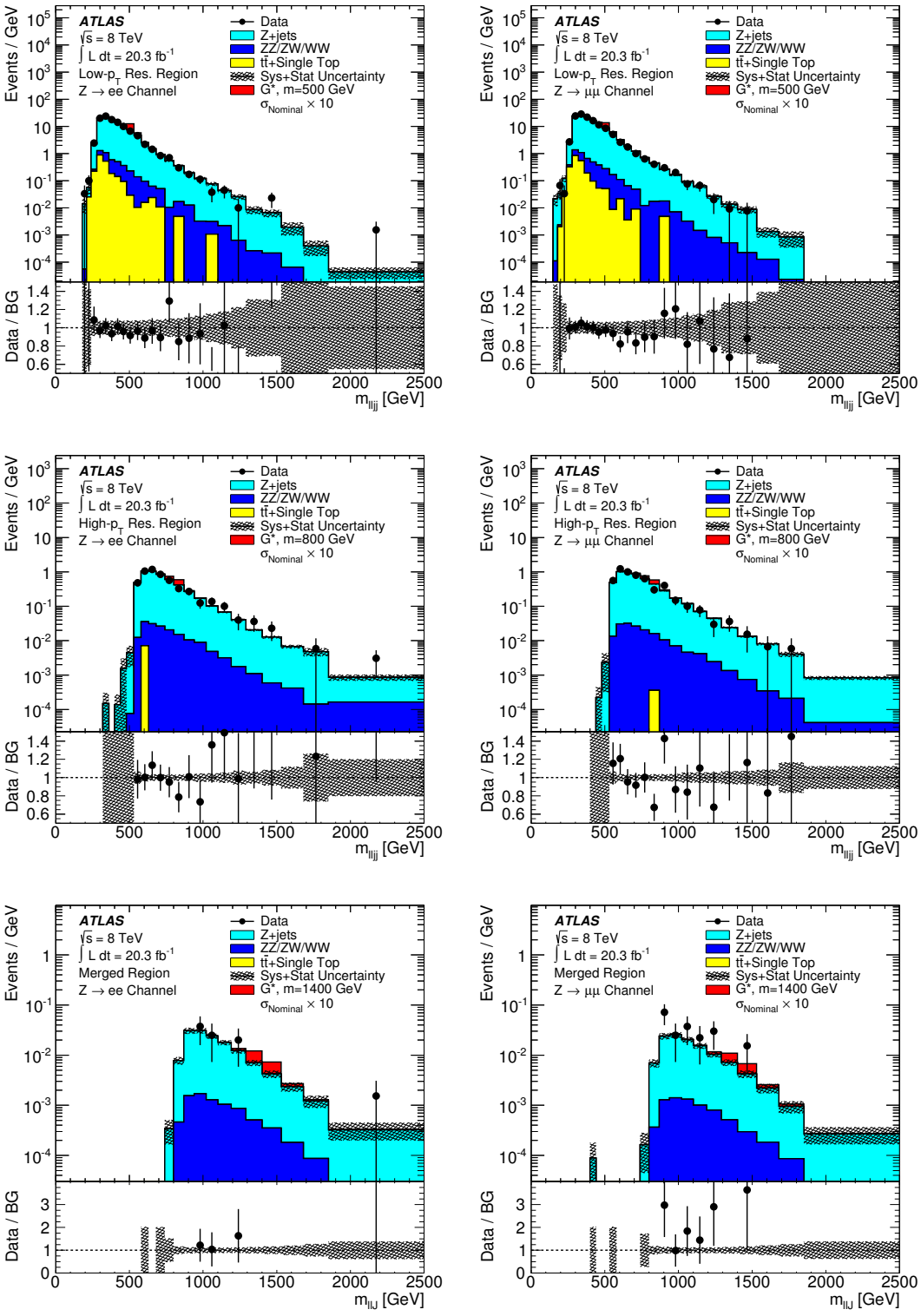

Figure 5.18: Comparison of data and background prediction for the m_{lljj} spectra for the low-p_T (top) and high-p_T (middle) resolved regions, and the m_{llJ} spectra for the merged region (bottom) for both electrons (left) and muons (right). The shaded band depicts the combined statistical and systematic uncertainty.

Table 5.5: The event yields in the signal regions for data, expected background, bulk RS graviton and EGM W' boson signal samples. The signal points correspond to 400 GeV (low-p_T), 800 GeV (high-p_T), 1600 GeV (merged). Uncertainties are given as two components, statistical and systematic respectively, except for the total background where the combined uncertainty including correlations and constraints from profiling to data is given.

Sample	LR	HR	MR
Z+jets	9460 ± 40 ± 660	591 ± 4 ± 15	20.9 ± 0.3 ± 2.3
$WW/WZ/ZZ$	234 ± 4 ± 22	20.6 ± 0.3 ± 1.4	1.38 ± 0.02 ± 0.13
$t\bar{t}$ + Single t	175.3 ± 9.2 ± 9.9	-	-
Total (unconstrained)	9870 ± 690	612 ± 17	22.3 ± 2.5
Total (constrained)	9730 ± 30	609 ± 6.1	22.32 ± 0.97
Data	9728	619	25
G^* Signal	1097 ± 17 ± 63	14.27 ± 0.19 ± 0.76	0.0995 ± 0.0013 ± 0.0059
W' Signal	1950 ± 40 ± 140	145.0 ± 2.3 ± 8.1	3.64 ± 0.06 ± 0.31

5.15.2 Validation of Statistical Analysis

The validity of the use of ML, and the treatment of the NP is tested. It is important that NP do not display large unexpected correlations to each other, as this is an indication that the likelihood ratio is behaving poorly. The asymptotic method chosen is more robust under correlations between NP than similar alternative techniques [103]. It is important that the NP are not drawn too far away from their nominal values, as this is indicative of the data being poorly modelled; and that they are not over constrained by the data, as this indicates that systematic uncertainties are over estimated. A small number of strong correlations, or a large number of moderate correlations can lead to unexpected behaviour in the mass distribution under simultaneous morphing of multiple parameters [100]. The measured NP pulls and correlations for the conditional ML, performed simultaneously over all signal regions, are shown in figures 5.19 and 5.20, respectively. The largest constraints and pulls on NP are present for the data driven uncertainties on the normalisation and shape of the Z+jets background. These uncertainties

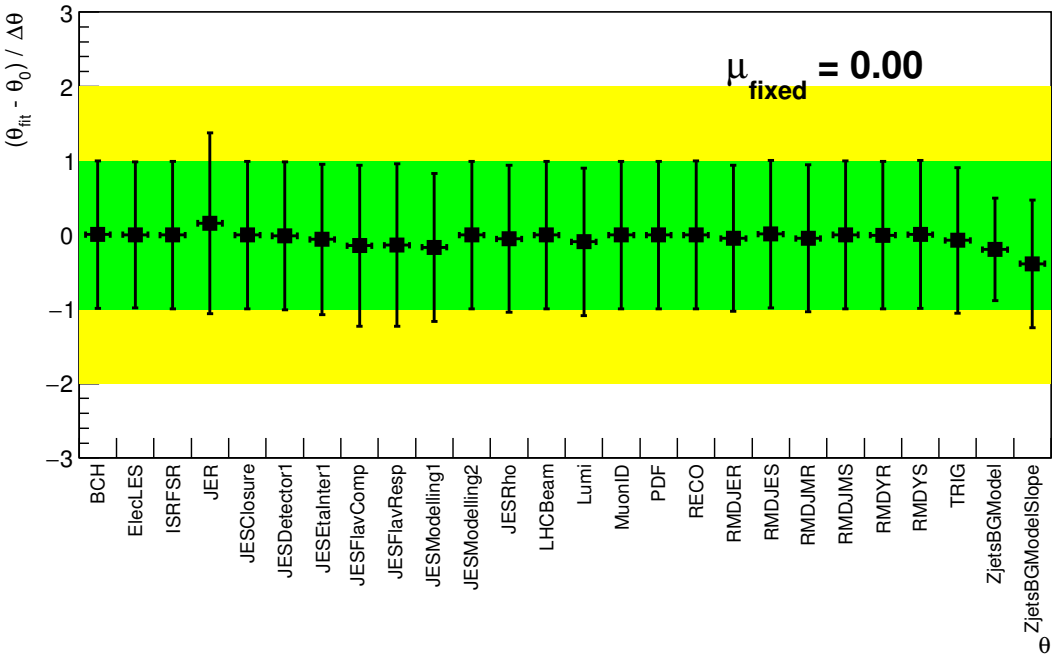

Figure 5.19: The pulls of the NP derived from the conditional ML fit simultaneously over all of the signal regions.

are derived from the statistical uncertainty of the data in the control regions, and are conservatively estimated. It is therefore to be expected that the signal regions are capable of constraining these uncertainties. These pulls and constraints are not sufficiently large as to raise major concerns and all correlations are small and below 20%.

5.15.3 Results of Statistical Analysis

A good agreement is observed between the data and the background prediction. The p-value ranges between 0.98 and 0.1 for both the bulk RS graviton and EGM W' boson, as shown in figure 5.21. The local significance only exceeds one standard deviation for a graviton with a pole mass of 350 GeV.

In the absence of a significant excess, upper limits are set at the 95% CL on the product of the cross-section and branching ratio for both models, shown

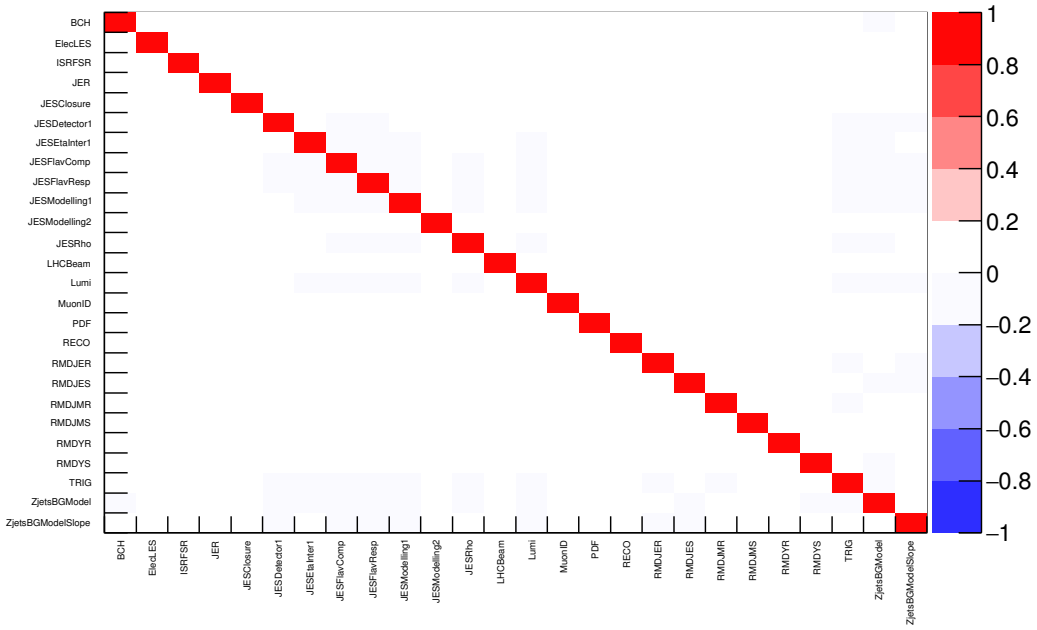

Figure 5.20: The correlations of the NP derived from the conditional ML fit simultaneously over all of the signal regions. An index of the names of the systematic uncertainties is given in the appendix.

in figure 5.22, with values given in table 5.6. For both models the limits range from $\approx$ 1 pb at 300 GeV to $\approx$ 10 fb at 2 TeV. From the cross-section limits, the observed (expected) lower mass limits are extracted for the bulk RS graviton with $k/\bar{M}_{\mathrm{Pl}} = 1.0$ at 740 GeV (700 GeV), and for the NNLO EGM W' boson with $c = 1$ at 1590 GeV (1540 GeV).

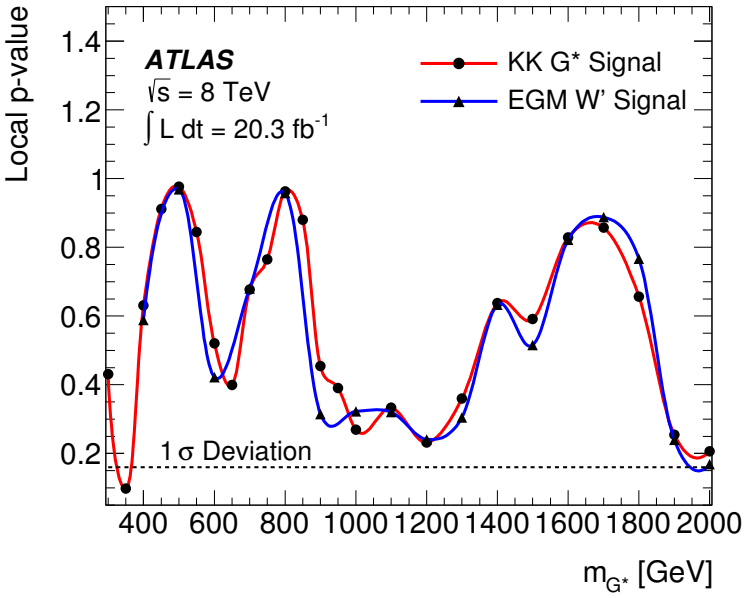

Figure 5.21: The local p-value calculated from the combination of signal regions for the bulk RS graviton and W' signal models.

Table 5.6: Expected and observed upper limits on the product of the production cross-section and the branching ratio for the bulk RS and EGM models, set at the 95% CL.

Mass	$\sigma(pp \to G^\star) \times \mathrm{BR}(G^\star \to ZZ)$ [pb]		$\sigma(pp \to W') \times \mathrm{BR}(W' \to ZW)$ [pb]	
[GeV]	Expected	Observed	Expected	Observed
300	1.18×10^{0}	1.73×10^{0}	-	-
400	3.61×10^{-1}	4.21×10^{-1}	7.30×10^{-1}	8.65×10^{-1}
500	1.63×10^{-1}	9.57×10^{-2}	3.36×10^{-1}	2.06×10^{-1}
600	8.38×10^{-2}	8.43×10^{-2}	1.47×10^{-1}	1.60×10^{-1}
700	5.65×10^{-2}	4.75×10^{-2}	1.07×10^{-1}	8.99×10^{-2}
800	4.48×10^{-2}	2.74×10^{-2}	9.88×10^{-2}	5.70×10^{-2}
900	2.92×10^{-2}	2.94×10^{-2}	5.61×10^{-2}	6.27×10^{-2}
1000	2.03×10^{-2}	2.44×10^{-2}	4.61×10^{-2}	5.20×10^{-2}
1100	1.56×10^{-2}	1.90×10^{-2}	3.71×10^{-2}	4.55×10^{-2}
1200	1.34×10^{-2}	1.73×10^{-2}	3.23×10^{-2}	4.17×10^{-2}
1300	1.10×10^{-2}	1.34×10^{-2}	2.70×10^{-2}	3.57×10^{-2}
1400	9.33×10^{-3}	8.87×10^{-3}	2.38×10^{-2}	2.38×10^{-2}
1500	9.42×10^{-3}	8.78×10^{-3}	1.95×10^{-2}	1.95×10^{-2}
1600	7.37×10^{-3}	6.06×10^{-3}	1.91×10^{-2}	1.57×10^{-2}
1700	6.73×10^{-3}	5.29×10^{-3}	1.83×10^{-2}	1.34×10^{-2}
1800	6.25×10^{-3}	5.88×10^{-3}	1.62×10^{-2}	1.44×10^{-2}
1900	5.94×10^{-3}	6.69×10^{-3}	1.67×10^{-2}	2.01×10^{-2}
2000	5.99×10^{-3}	7.11×10^{-3}	1.55×10^{-2}	2.00×10^{-2}

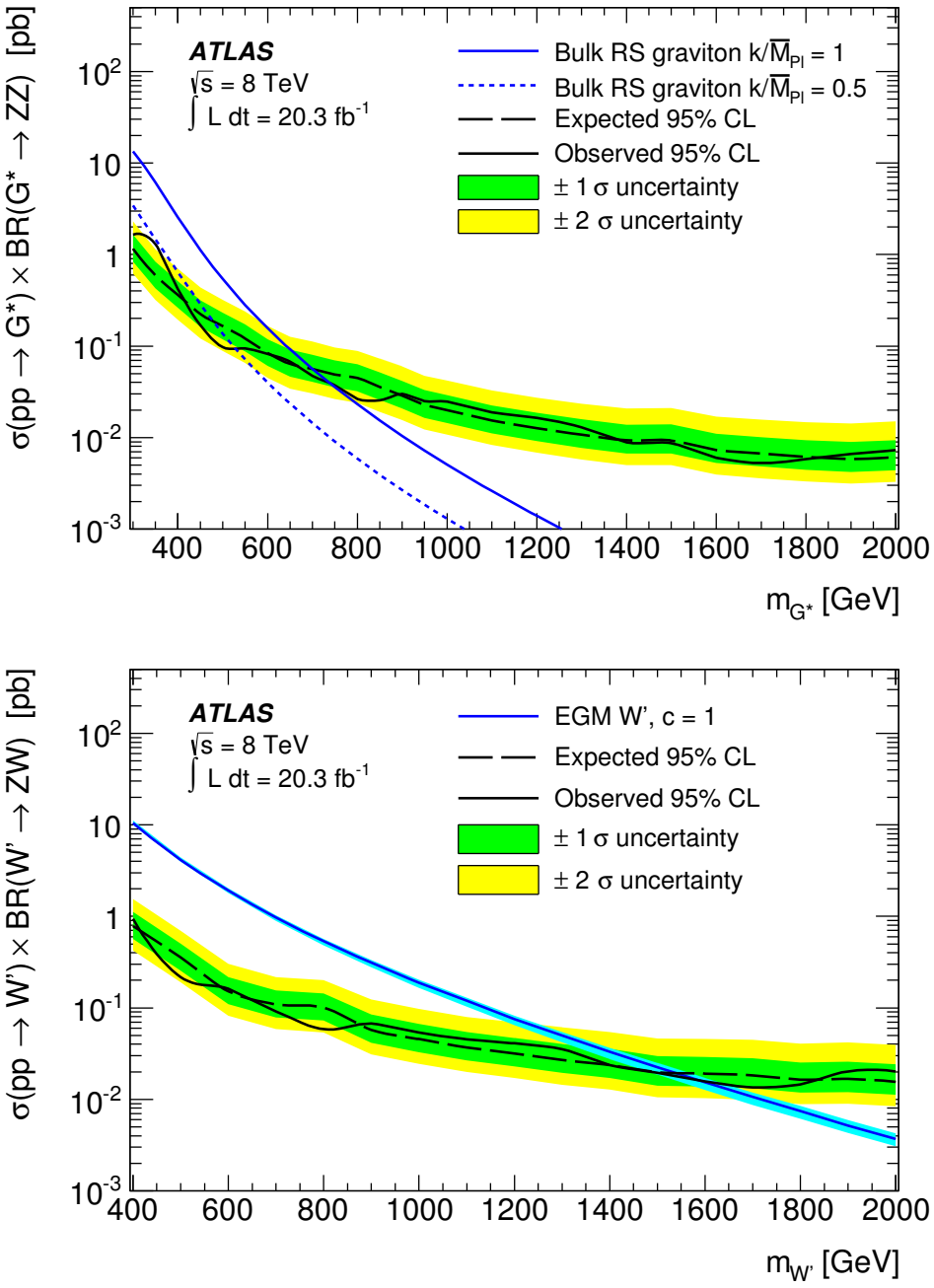

Figure 5.22: The expected and observed 95% CL upper limit on the product of the production cross-section and branching ratio as a function of pole mass for the bulk RS graviton signal (top) and EGM W' boson (bottom). The band around the W' boson cross-section is due to the theoretical uncertainties in the NNLO calculation.

6

Diboson Resonance Search Combination

6.1 Introduction

The ATLAS Collaboration have performed a number of analyses searching for the bulk RS graviton and EGM W' boson, decaying to VV, where V represents either a W or Z boson. A summary of these analyses is given in table 6.1.

Table 6.1: A summary of the diboson resonance searches performed by ATLAS with the Run 1 dataset. An X represents either a bulk RS graviton or EGM W' boson.

Analysis	7 TeV	8 TeV
$G^* \to ZZ \to \ell\ell\ell'\ell'$	5.1 fb^{-1} [105]	-
$G^* \to WW \to \ell\nu\ell'\nu'$	5.1 fb^{-1} [106]	-
$W' \to WZ \to \ell\nu\ell'\ell'$	5.1 fb^{-1} [107]	20.3 fb^{-1} [71]
$X \to ZV \to \ell\ell qq$	5.1 fb^{-1} [105]	20.3 fb^{-1} [2]
$X \to WV \to \ell\nu qq$	5.1 fb^{-1} [108]	20.3 fb^{-1} [73]
$X \to VV \to qqqq$	-	20.3 fb^{-1} [74]

To improve the sensitivity to exotic resonances, the four analyses performed with data collected with $\sqrt{s} = 8$ TeV, $\ell\nu\ell'\ell'$, $\ell\ell qq$, $\ell\nu qq$ and the $qqqq$, are combined. The fully hadronic analysis is also referred to as the JJ analysis, as it uses large-R jets exclusively. The result of the combination is interpreted using

the EGM W' boson with $c = 1$, and the bulk RS graviton with $k/\bar{M}_{\mathrm{Pl}} = 1.0$.

The diboson resonances have similar branching ratios to $\ell\nu qq$, $\ell\ell qq$, and $\ell\nu\ell'\ell'$ as shown in figure 6.1. The leptonic and semi-leptonic analyses have similar background sources present, and use similar MC techniques to model the backgrounds. The fully hadronic analysis contends with a much higher level of QCD background, and so uses a data driven technique to model the background distribution. Theses analyses have comparable sensitivities through a large mass range.

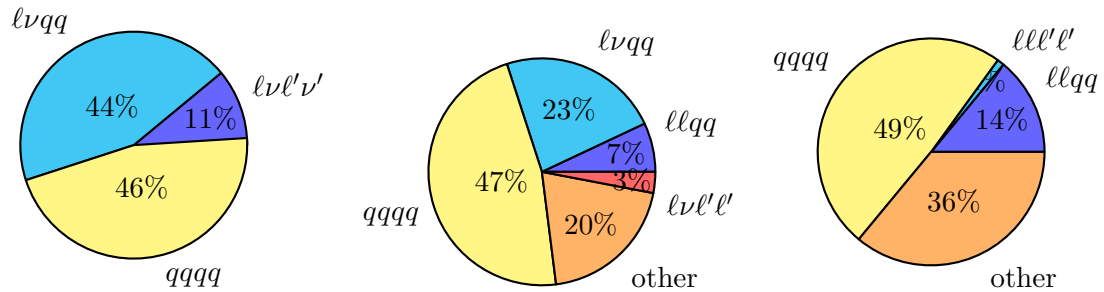

(a) WW (b) WZ (c) ZZ

Figure 6.1: The branching ratios for WW (left), WZ (middle) and ZZ (right) decays. Channels where at least one Z boson decays to invisible products are grouped as 'other'.

6.2 Analysis Channels

The analyses which are used for this combination each select a different number of leptons. In general the lepton selection criteria are different in each analysis. In order to ensure that all of the signal regions used in the combination are statistically independent, a common set of loose lepton selection criteria is defined for the purposes of vetoing, as described in section 5.4.

6.2.1 Three Lepton

The three lepton analysis, $\ell\nu\ell'\ell'$, uses several signal regions in order to optimise sensitivity over a large signal mass range [71]. The selection regions share the same nomenclature as the $\ell\ell qq$ channel, and are referred to as the LR and HR, which are both subdivided into four selection regions based on how many of the final state leptons are electrons. The background expectation is generated from MC, and is dominated by SM WZ production. The theoretical uncertainty for the prediction of the WZ background is the dominant systematic, and is approximately 10%. For the HR, the background prediction is extrapolated to very high mass by fitting two power-law functions to the simulated background. The first fit is performed to the SM WZ background, and the second is fitted to the remaining sub-dominant backgrounds. The predicted and observed mass spectra for the two selection regions are shown in figure 6.2.

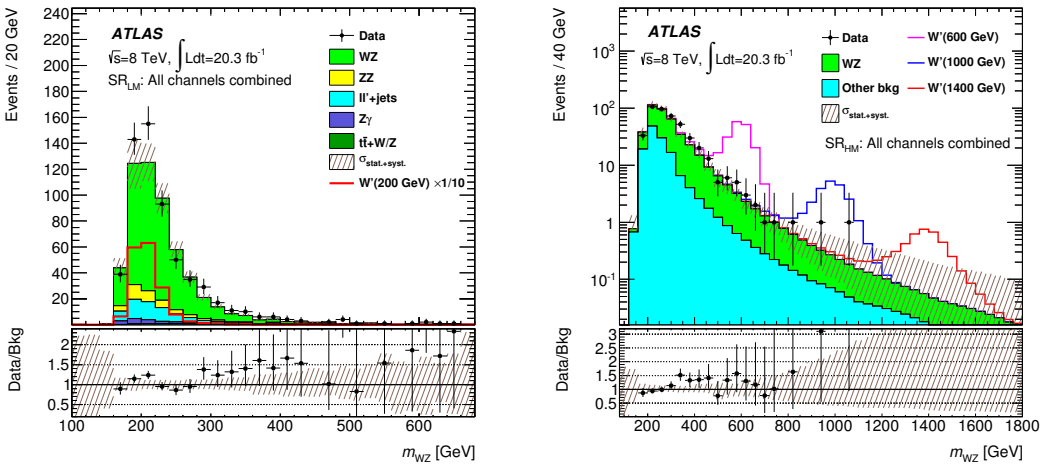

Figure 6.2: The predicted and observed $\ell\nu\ell'\ell'$ invariant mass spectra for the LR (left) and HR (right), summed over all lepton flavour combinations. The uncertainty bands shown account for the MC statistical uncertainties and all background systematic uncertainties.

No significant excess is observed and mass limits are extracted using a profile likelihood method using the $\tilde{q}_\mu$ test statistic. For the production of the EGM

W' boson, expected and observed mass limits are set at 1.49 TeV and 1.52 TeV respectively. The corresponding limit on the production times cross-section obtained is shown in figure 6.3. Due to the limited amount of data, particularly in the high mass tail, this analysis uses toys to extract limits in preference to asymptotics. This method, coupled with the lack of events at high mass, results in the absence of negative error bands on the expected limit. Due to the charged final state, this search is not sensitive to the neutral RS graviton resonance.

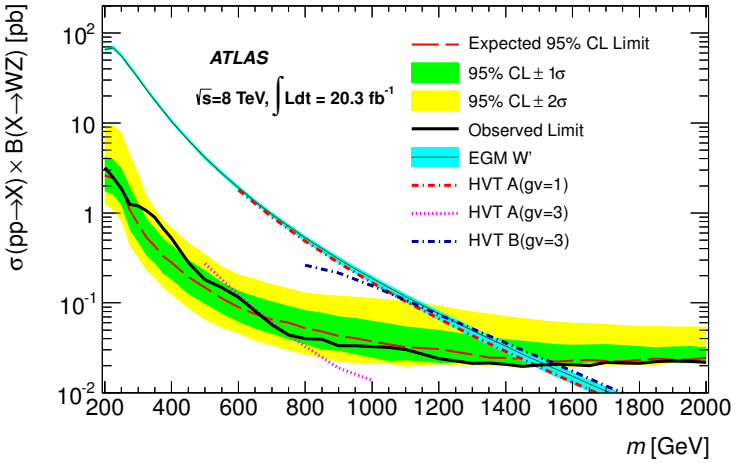

Figure 6.3: The expected and observed 95% CL upper limits on the product of the production cross-section and branching ratio as a function of pole mass of the EGM W' boson for the $\ell\nu\ell'\ell'$ channel. The band around the EGM cross-section is due to the theoretical uncertainty in the NNLO calculation.

6.2.2 One Lepton

The one lepton analysis for the $\ell\nu qq$ final state, uses several signal regions to optimise the sensitivity over a large signal mass range [73]. These regions share the same nomenclature as the $\ell\ell qq$ channel, namely LR, HR and MR, with each region being subdivided by lepton flavour. Both the LR and HR regions select two resolved hadron jets, with more stringent p_T requirements placed on both the leptonic and hadronic sides of the event in the HR. The hadronic side of an

event in the MR comprises a single large-R jet which uses the BDRS-A filtering algorithm. The dominant background is V+jets, and the dominant uncertainty is due to the normalisation of this background. The normalisation of the V+jets background in each selection region is derived from a fit to the E_T^{miss} distributions in control region data, independently for both lepton flavours. The uncertainty on this normalisation ranges from 3% to 4% in the LR and HR, and 15% to 18% in the MR. The expected and observed $\ell\nu jj$ and $\ell\nu J$ mass spectra for the selection regions are shown in figure 6.4.

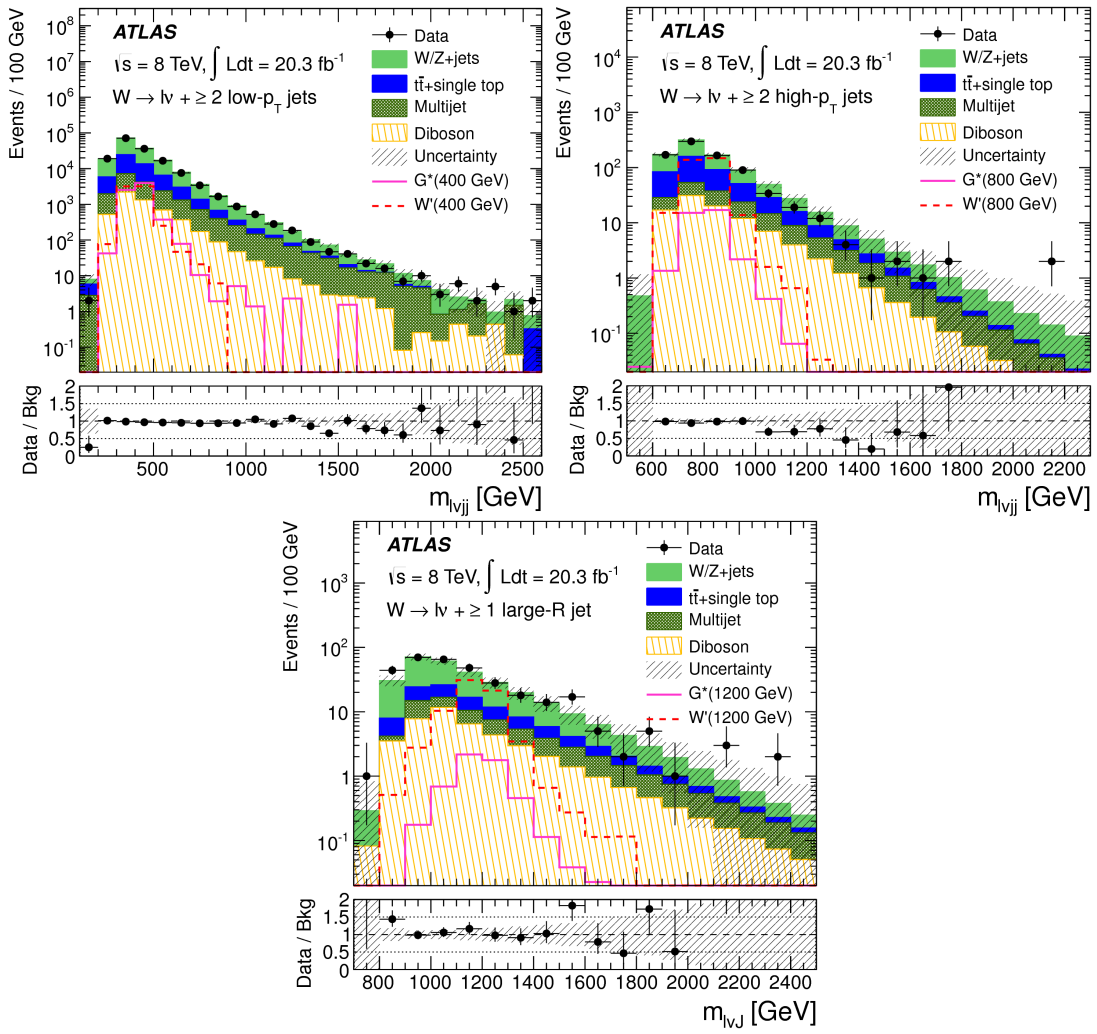

Figure 6.4: The predicted and observed $\ell\nu jj$ and $\ell\nu J$ invariant mass spectra for the LR (top left), HR (top right) and MR (bottom).

No significant excess is observed, and mass limits are set using a profile like-

lihood method using the $\tilde{q}_\mu$ test statistic. Mass limits for the production of the EGM W' boson and bulk RS graviton are found to be 1490 GeV and 700 GeV respectively. The corresponding limits on the production times cross-section obtained is shown in figure 6.5.

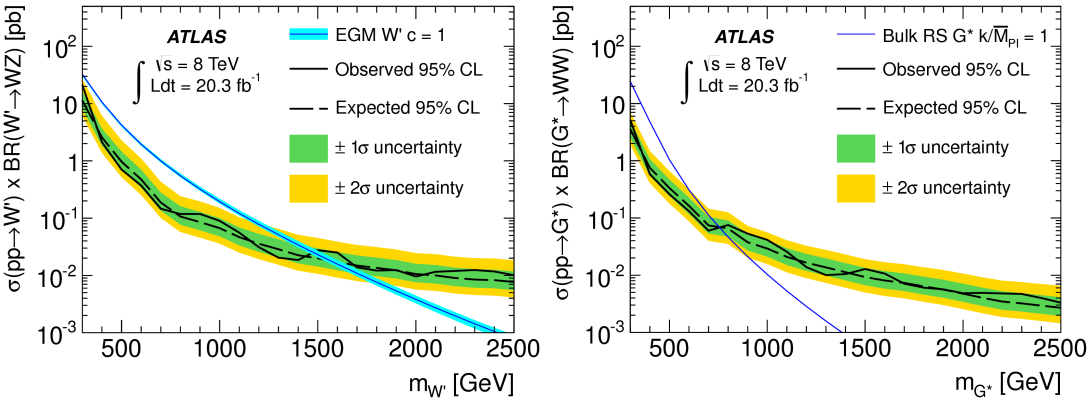

Figure 6.5: The expected and observed 95% CL upper limits on the product the of production cross-section and branching ratio as a function of pole mass of the EGM W' boson (left) and RS graviton (right) for the $\ell\nu qq$ channel. The band around the EGM cross-section is due to the theoretical uncertainty in the NNLO calculation.

6.2.3 Fully Hadronic

The fully hadronic channel, $qqqq$, selects two large-R jets with BDRS-A filtering [74]. These jets are required to have < 30 tracks associated to them, prior to the application of the grooming process described in section 4.5.3. This requirement is the source of the dominant uncertainty. The masses of the large-R jets are required to satisfy $|m_{JJ} - m_V| < 13$ TeV. This creates the three signal regions, WW, WZ and ZZ, which are not statistically independent.

The background dijet mass distribution is modelled by the smoothly falling function

$$\frac{dn}{dx} = p_1 \, (1-x)^{p_2 - \zeta p_3} \, x^{p_3}, \tag{6.1}$$

where $x = m_{JJ}/\sqrt{s}$, p_1 is the normalisation, p_2 and p_3 are dimensionless shape

parameters, and ζ is a dimensionless quantity chosen after fitting which minimises the correlation between p_2 and p_3. This functional form is chosen as it is capable of modelling a wide range of smooth, monotonically decreasing distributions, while being incapable of accommodating resonances. The ML fit is performed in the range 1.05 TeV $< m_{JJ} <$ 3.55 TeV, which ensures that the trigger is fully efficient for the boson tagged jets and that the entirety of the high energy tail is included.

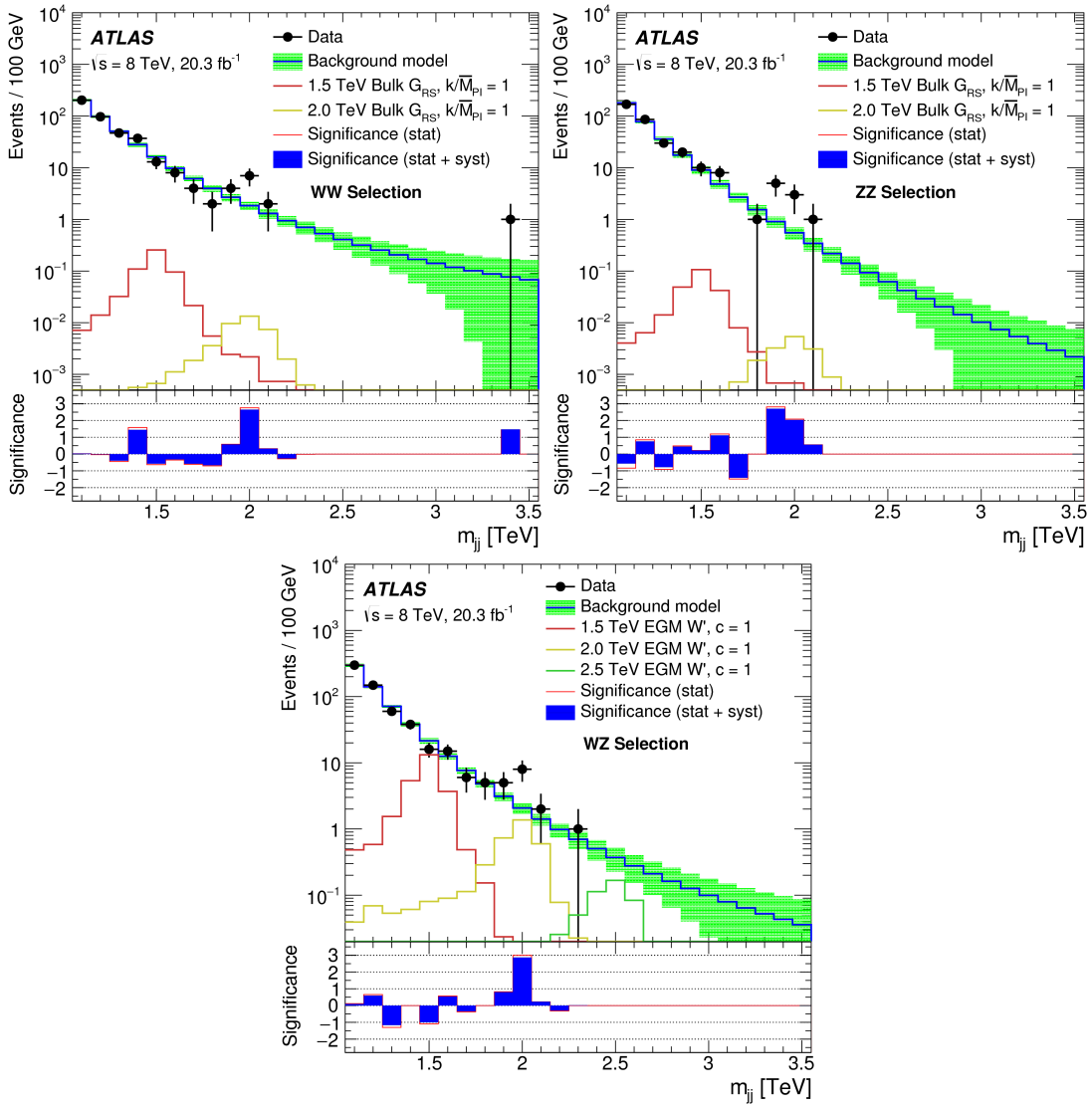

Figure 6.6: The data and fitted dijet mass spectra for the WW (top left), ZZ (top right), and WZ (bottom) signal regions.

The mass distributions shown in figure 6.6 show an excess at 2 TeV. The

largest excess is found in the WZ signal region, with a significance of 3.4 σ as shown in figure 6.7.

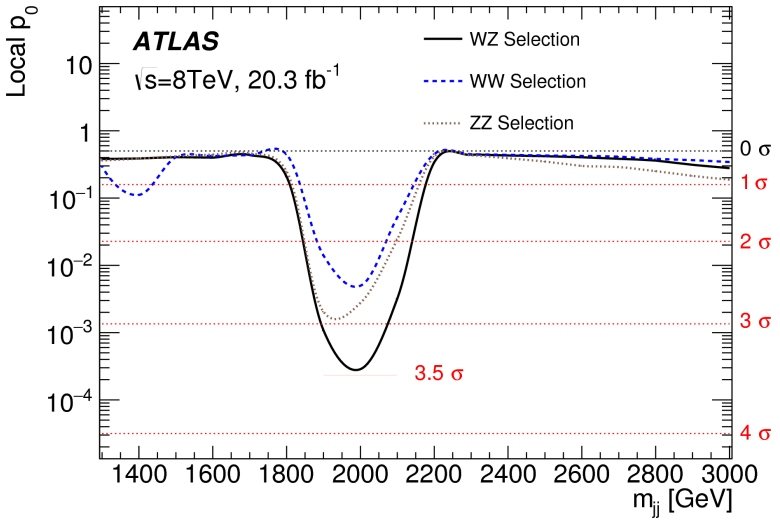

Figure 6.7: The observed p-value for the fully hadronic channel. The largest excess is found for the WZ channel with a significance of 3.4 σ.

Limits are set on the product of the production cross-section and branching ratio for $W' \to WZ$, $G^* \to WW$ and $G^* \to ZZ$ using a profile likelihood method using the q_μ test statistic as shown in figure 6.8.

6.3 Combination Strategy

This analysis is composed of a total of 21 signal regions when lepton flavour is accounted for. All of the channels are ensured to be statistically independent by vetoing on the number of leptons passing loose lepton requirements which are common to all four analyses. Statistical independence is ensured between the signal regions contained within each analysis, meaning that all of the signal regions considered for the combination are in turn independent. This allows for a search to be performed and limits set simultaneously over all of the signal regions using q_0 and $\tilde{q_\mu}$ profile likelihood test statistics respectively as described in section 5.11.

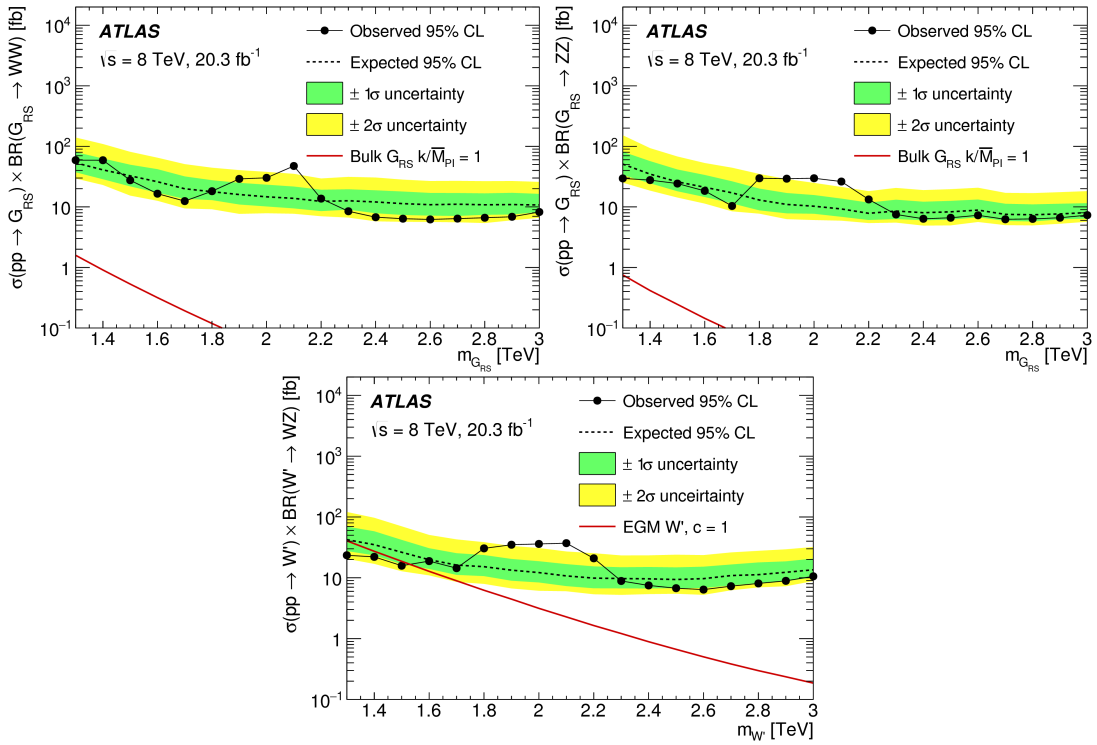

Figure 6.8: The expected and observed 95% CL upper limits on the product of the production cross-section and branching ratio as a function of pole mass for $G^* \to WW$ (top left), $G^* \to ZZ$ (top right) and $W' \to WZ$ (bottom) for the $qqqq$ channel. Note that the cross-sections shown for the EGM W' use a LO calculation.

The leptonic and semi-leptonic analyses do not observe excesses comparable to that seen in the fully hadronic analysis. For this reason, the combination is initially performed for the EGM W' boson only, using the leptonic and semi-leptonic final states.

6.4 Modifications to Analysis Channels

Where possible the analyses have remained unaltered from their published forms. In some instances it is necessary to apply modifications in order to perform the combination.

The analyses contained within the combination use two possible decay channels of the RS graviton; the $l\nu qq$ channel searches for $G^* \to WW$ decay, and the

$\ell\ell qq$ channels searches for $G^* \to ZZ$ decay. The $qqqq$ channel searches separately for the WW and ZZ decay channels, using statistically interdependent datasets. The combination sets limits on the $G^* \to VV$ decay, and so the union of the WW and ZZ selection criteria is taken in the fully hadronic channel.

Setting limits on the decay into VV introduces a model dependency due to the relative branching ratio of the $G^* \to ZZ$ and $G^* \to WW$ decays. The values of these branching ratios as a function of the graviton pole mass are shown in figure 6.9.

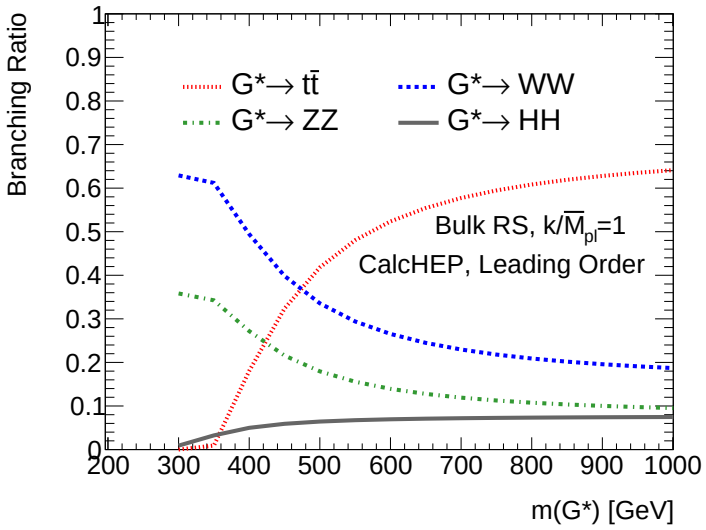

Figure 6.9: The branching ratios of the four largest bulk RS graviton decay paths against graviton pole mass.

In the leptonic and semi-leptonic analyses, a NNLO k-factor is applied to the W' production cross-section. At high resonant mass the value of the k-factor fluctuates greatly [83]. The fully hadronic analysis, which probes masses higher than the other analyses, uses the LO cross-section. For the combination, the cross-section is reverted to that of the LO calculation in all channels.

The signal pole mass range over which limits are set is changed to optimise the effect of the combination. The mass ranges used for both the EGM W' boson and the bulk RS graviton samples in the individual analyses are noted in table 6.2.

For the $\ell\nu\ell'\ell'$ and $\ell\ell qq$ channels, the signal mass range is extended to 2500 GeV, and signal masses above 2500 GeV used in the $qqqq$ channel are discarded.

Table 6.2: The signal pole mass ranges used in the component analyses and the combination.

Analysis	Initial mass range	Combination mass range
$\ell\nu\ell'\ell'$	200 GeV $\rightarrow$ 2000 GeV	200 GeV $\rightarrow$ 2500 GeV
$\ell\ell qq$	300 GeV $\rightarrow$ 2000 GeV	300 GeV $\rightarrow$ 2500 GeV
$\ell\nu qq$	300 GeV $\rightarrow$ 2500 GeV	300 GeV $\rightarrow$ 2500 GeV
$qqqq$	1200 GeV $\rightarrow$ 3000 GeV	1200 GeV $\rightarrow$ 2500 GeV

The combination can only be performed for signal mass points which are common to all four analyses. The $\ell\nu\ell'\ell'$ channel uses the finest mass spacing 50 GeV, and both the $\ell\nu qq$ and $qqqq$ analyses used 100 GeV. The $\ell\ell qq$ channel used a combination of 50 GeV below 1000 GeV, and 100 GeV above. The combination must use the coarsest granularity of the component analyses, and so 100 GeV is used.

The $\ell\nu\ell'\ell'$ channel suffers with an instability in the limit setting procedure caused by having very low numbers of expected background events in some bins of the $\ell\nu\ell'\ell'$ mass distribution. This results in multiple mass points failing to converge on a limit. None of the problematic mass points are adjacent, and so the fine granularity allows an interpolation between the limits of the neighbouring mass points to be performed. In the coarser granularity regime of the combination this is not a feasible possibility. The background is rebinned, removing the low event counts present in the background prediction. An exponential binning is introduced to the LR, and the HR is truncated slightly to ensure the turn on is contained within a single bin as shown in figure 6.10.

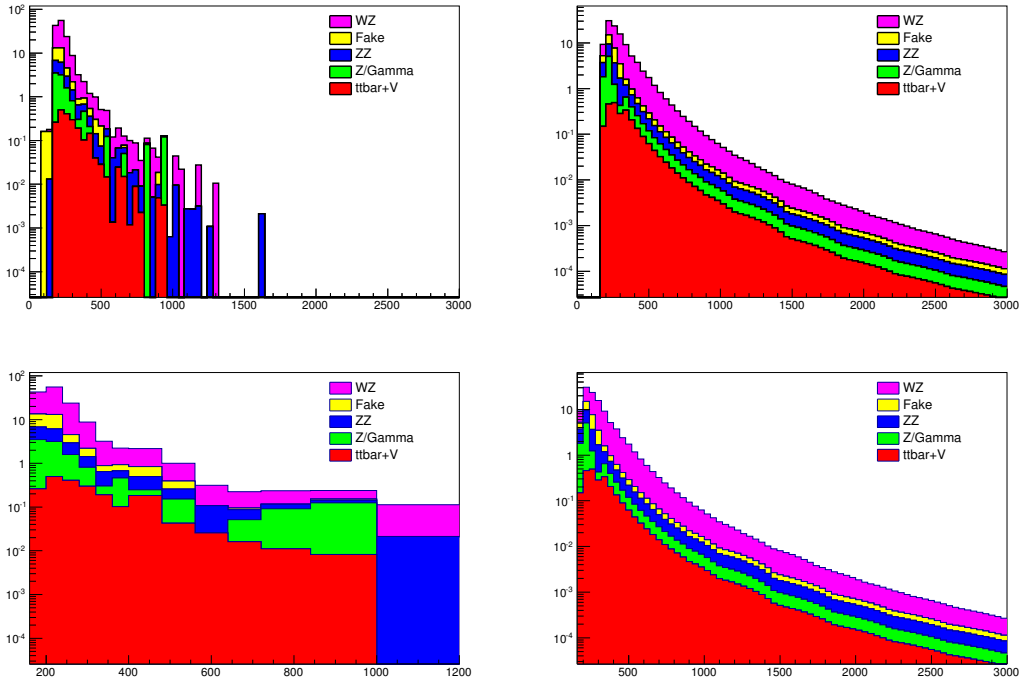

Figure 6.10: The mass distributions for the $\ell\nu\ell'\ell'$ channel in the LR (left) and HR (right), for both before (top) and after (bottom) the application of the modified binning.

6.5 Systematic Uncertainties

In addition to the systematic uncertainties described in section 5.9, there are a number of uncertainties introduced into the combination. In the $\ell\nu qq$ channel, an uncertainty is applied to the b-tagging efficiency (`BTAG_EFF`). Each of the background components of the $\ell\nu qq$ channel has two uncertainties applied accounting for the normalisation and shape independently. The naming of these uncertainties follows the for `LVQQ_`*sample*`_`*region*, where *sample* represents one of QCD (`QCD`), top quark (`TOP`), V+jets (`VJETS`), or SM diboson (`VV`), and *region* represents the LR (`LRR`), HR (`HRR`) or MR (`MR`).

The $\ell\nu\ell'\ell'$ channel introduces uncertainties on the predictions of the SM diboson background (`WZShape`, `WZTheo`, `WZXSection`, and `ZZXSection`), the top quark background (`TtbarvXSection`) and the fake lepton background (`Fake`). One further uncertainty is introduced due to the fit performed on the background

distribution in the HR (`Fit`).

Additional uncertainties are applied to account for the electron trigger and reconstruction (`ElecTrig`, `ElecReco`, `ElecIDSF`, `ElecIsoIPSF` and `ElecLSF`). The electron energy scale is parametrised as three independent parameters: `ElecLESPS`, ElecLESR12, and `ElecLESZeeAll`, the last of which replaces `ElecLES`, referred to in the previous chapter.

Three additional scale factor uncertainties are applied to account for muon reconstruction (`MuonIsoIPSF`, `MuonReco` and `MuonTrig`), and one uncertainty as a result of the MS (`MuonMS`).

Two systematic uncertainties are introduced to model the Missing Transverse Energy (MET) scale (`METSoftScale`) and resolution (`METSoftReso`).

Additional parameters are included in the $\ell\nu qq$ and $\ell\nu\ell'\ell'$ channels to account for the small-R jet JES (`JESBase0`, `JESBase1`, `JESBase2`, `JESBase3`, `JESBase4`, `JESBase5`, and `JESBjet`). This is not independent to the parametrisation used in the $\ell\ell qq$ analysis; however, correlations are sufficiently small between parameters to not impact the analysis.

The $qqqq$ analysis introduces an uncertainty on the number of tracks associated to large-R jets (`trk`).

Where possible systematics that are common to multiple channels are parametrised by a single nuisance parameter. Table 6.3 shows the NP that are used in multiple channels. Due to different parametrisations of the small-R JES, there are several NP that are unique to the $\ell\ell qq$ channel. These are intrinsically correlated to the complementary set of NP used in the $\ell\nu qq$ and $\ell\nu\ell'\ell'$ channels; however, no two parameters have sufficiently high correlation to impact the analysis.

The dominant background in the $\ell\nu\ell'\ell'$ channel is SM WZ diboson production. The normalisation and shape uncertainties on this background are the dominant systematics uncertainties in the combination for signal masses < 1 TeV. The $V+$jets background is dominant in the $\ell\nu qq$ channel. For ≈ 1 TeV signal masses,

Table 6.3: Uncertainties that are applied to multiple channels in the combination. These are considered fully correlated between channels, and share common parameters in the likelihood fits. Systematics that are present only in one channel are omitted from this table.

Systematic	$\ell\nu\ell'\ell'$	$\ell\ell qq$	$\ell\nu qq$	$qqqq$
ISRFSR		✓	✓	
Lumi	✓	✓	✓	
PDF		✓	✓	
METSoftReso	✓		✓	
METSoftScale	✓		✓	
ElecLER	✓	✓	✓	
ElecLESPS	✓		✓	
ElecLESR12	✓		✓	
ElecLESZeeAll	✓	✓	✓	
ElecReco	✓	✓		
ElecTrig	✓	✓	✓	
MuonID	✓	✓	✓	
MuonLES	✓	✓	✓	
MuonReco	✓	✓		
MuonTrig	✓	✓	✓	
RMDJER		✓	✓	✓
RMDJES		✓	✓	✓
RMDJMR		✓	✓	
RMDJMS		✓	✓	✓
RMDYR		✓	✓	
RMDYS		✓	✓	
JER	✓	✓	✓	
JESBase0	✓		✓	
JESBase1	✓		✓	
JESBase2	✓		✓	
JESBase3	✓		✓	
JESBase4	✓		✓	
JESBase5	✓		✓	
JESClosure	✓	✓	✓	
JESEtaInter1	✓	✓	✓	
JESEtaInter2	✓	✓	✓	
JESFlavComp		✓	✓	
JESFlavResp		✓	✓	
JESMuOff	✓	✓	✓	
JESNPVOff	✓	✓	✓	
JESPileupPt	✓	✓	✓	
JESRho	✓	✓	✓	
JESSinglePart	✓	✓	✓	

the uncertainty of the V + jets background normalisation in the MR of the $\ell\nu qq$ channel is the dominant systematic uncertainty. In the combination for signal masses > 2 TeV, the shape uncertainty of the V + jets background in the MR of the $\ell\nu qq$ channel is the dominant systematic uncertainty. The systematics which produce the largest sensitivity degradations are shown in figure 6.11.

6.6 Signal Region Selection

Not all of the signal regions are sensitive to all signal masses, in particular the fully hadronic channel which uses only large-R jets has little sensitivity at low mass. For this reason not all of the signal regions are used to set limits on each signal mass point. The signal regions used for the EGM W' boson are shown in table 6.4.

6.7 Validation of Statistical Analysis

The validity of the use of ML, and the treatment of the NP is tested. These checks were previously performed in the respective analyses of the component channels, and where large correlations or pulls were observed, the NP were investigated and the cause understood. For this reason only correlations, strong pulls or pull constraints arising from the combination of the analyses are considered as a concern. There is no signal mass for which all signal regions are used, and so two test signal masses, 600 GeV and 1200 GeV, are chosen to verify the validity of the statistical analysis.

It is important that nuisance parameters do not display unexpected correlations to each other, as this could lead to poor behaviour of the likelihood ratio. The correlation matrices for the 600 GeV and 1200 GeV W' boson are shown in figure 6.12 and 6.13, respectively. There are a small number of moderate corre-

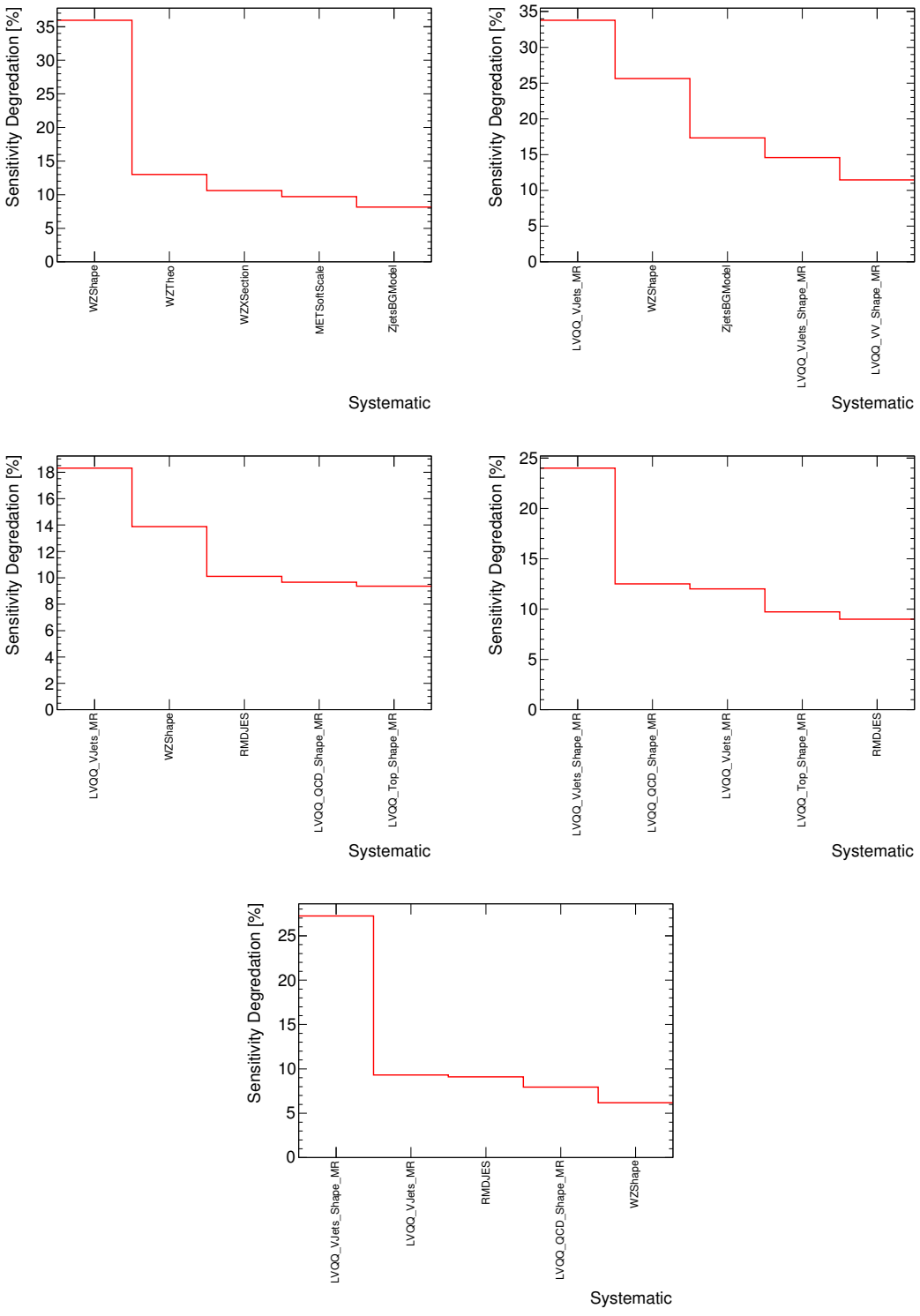

Figure 6.11: The dominant systematics and the resulting sensitivity degradation on the upper limits extracted for a W' boson of mass 500 GeV (top left), 1000 GeV (top right), 1500 GeV (middle left), 2000 GeV (middle right) and 2500 GeV (bottom).

Table 6.4: Selection regions used in the statistical analysis for each of the W' boson signal mass points.

Signal Mass [TeV]	$qqqq$	$\ell\nu qq$	$\ell\ell qq$	$\ell\nu\ell'\ell'$
0.2	-	-	-	LR, HR
0.3	-	LR	LR	LR, HR
0.4	-	LR	LR	LR, HR
0.5	-	LR	LR	LR, HR
0.6	-	LR, HR	LR, HR	LR, HR
0.7	-	LR, HR	LR, HR	LR, HR
0.8	-	LR, HR, MR	LR, HR	LR, HR
0.9	-	HR, MR	LR, HR, MR	LR, HR
1.0	-	HR, MR	HR, MR	LR, HR
1.1	-	HR, MR	HR, MR	LR, HR
1.2	MR	MR	HR, MR	LR, HR
1.3	MR	MR	HR, MR	LR, HR
1.4	MR	MR	HR, MR	LR, HR
1.5	MR	MR	HR, MR	LR, HR
1.6	MR	MR	HR, MR	LR, HR
1.7	MR	MR	HR, MR	LR, HR
1.8	MR	MR	HR, MR	LR, HR
1.9	MR	MR	HR, MR	LR, HR
2.0	MR	MR	HR, MR	HR
2.1	MR	MR	HR, MR	HR
2.2	MR	MR	HR, MR	HR
2.3	MR	MR	HR, MR	HR
2.4	MR	MR	HR, MR	HR
2.5	MR	MR	HR, MR	HR

lations, and a single strong correlation between the NP related to the V + jets modelling in the LR of the $\ell\nu qq$ channel. The systematics associated to these NP affect only the $\ell\nu qq$ channel, and the correlation is understood in the respective analysis. No new large correlations are generated due to the combination procedure.

The pulls of the nuisance parameters from the nominal values, and the constraints applied by the data are evaluated to ensure the systematics accurately represent the data. In figures 6.14 and 6.15, large constraints are present for the Z + jets normalisation uncertainty in the $\ell\ell qq$ channel, and the top quark shape uncertainty for the LR of the $\ell\nu qq$ channel. The systematics associated

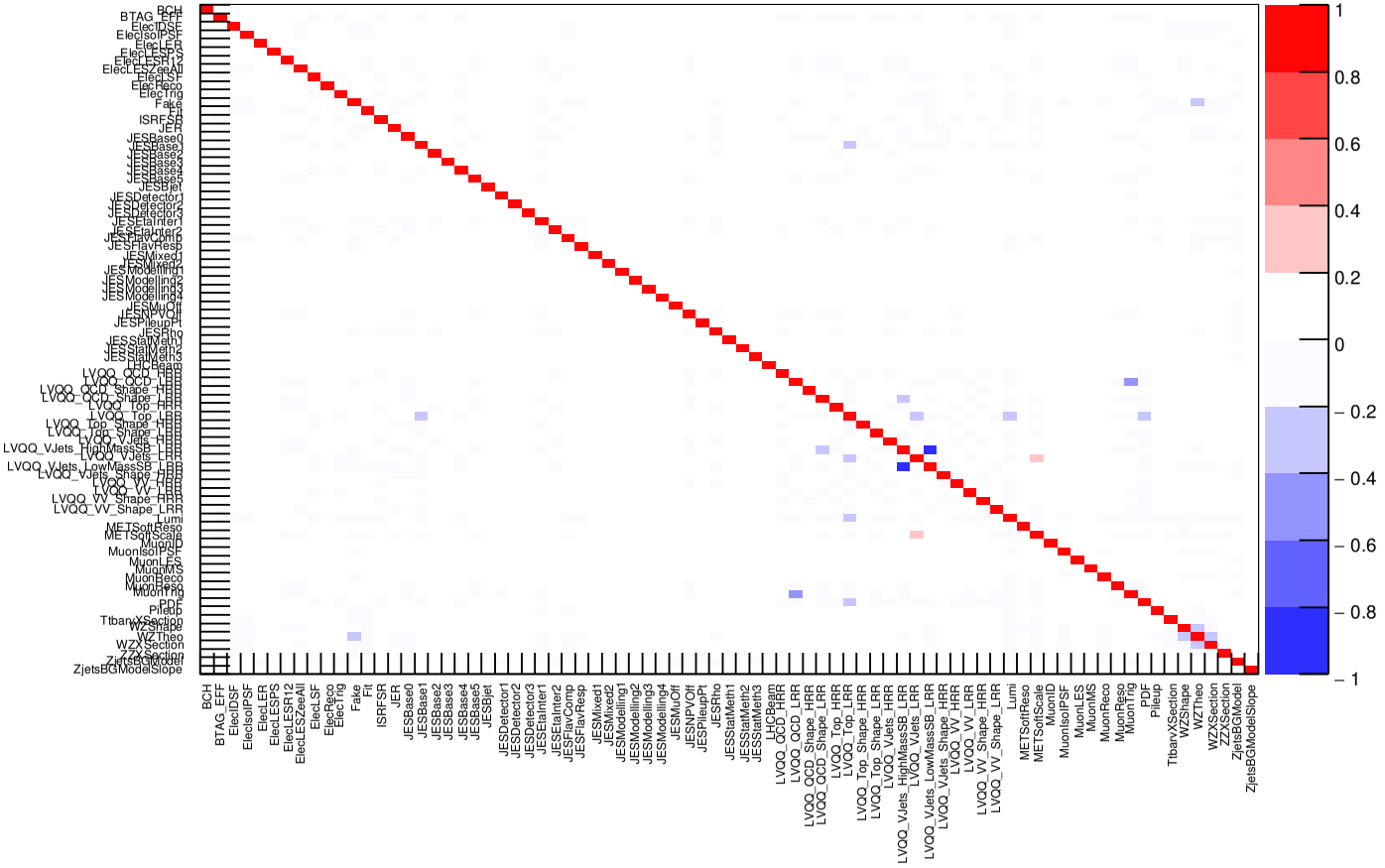

Figure 6.12: The correlations of the nuisance parameters derived from the conditional ML, fit simultaneously over the signal regions used to search for a 600 GeV W' boson.

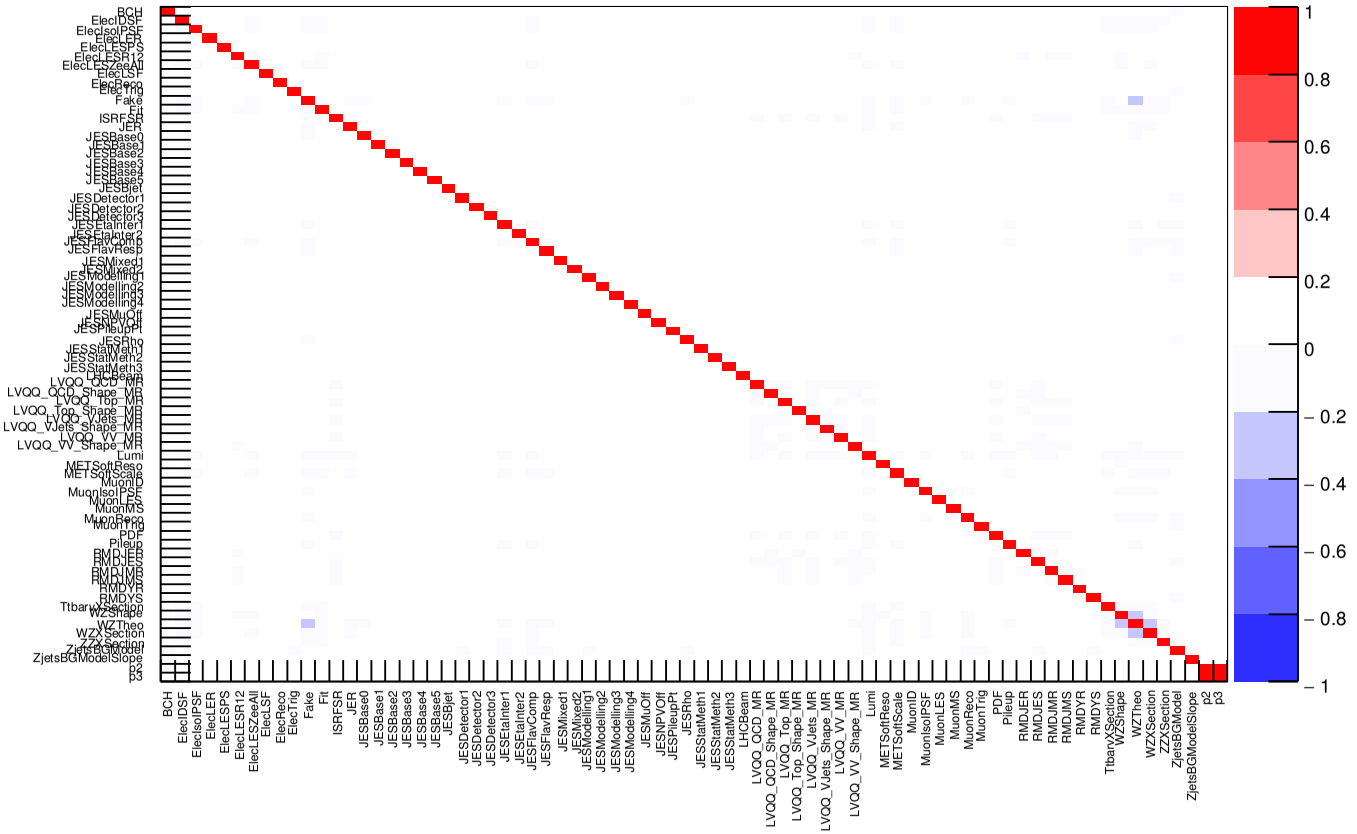

Figure 6.13: The correlations of the nuisance parameters derived from the conditional ML, fit simultaneously over the signal regions used to search for a 1200 GeV W' boson.

to these NP each only affect one channel, and the constraints were observed and understood in the individual analyses. No new strong pulls or constraints are generated through the combination procedure.

6.8 Results of Statistical Analysis

The expected sensitivities of the individual channels for the EGM W' boson are shown in figure 6.16. Initially the leptonic and semi-leptonic final states are combined, followed by the full combination of all four channels.

6.8.1 Leptonic Combination

The test statistic q_0 is used to quantify the deviation between the data and background prediction for the combination of the leptonic and semi-leptonic final states. The p-value for the test statistic has a maximum deviation of 2.2 σ at 300 GeV. At 2 TeV, where the fully hadronic analysis observed an excess, the data are consistent with the background only hypothesis within 1 σ.

Limits are extracted at the 95% CL on the production of the EGM W' boson for the combination of the leptonic and semi-leptonic channels, as shown in figure 6.17. Expected and observed mass limits are extracted to be 1770 GeV and 1830 GeV, respectively.

6.8.2 Full Combination

The p-values are derived from the q_0 test statistic for the combination of the signal regions from all four channels is shown in figure 6.18. The largest deviation from the background only hypothesis is observed at 2 TeV. For the EGM W' boson and RS graviton, the deviations are 2.5 σ and 1.8 σ, respectively. These deviations significantly reduced from the 3.4 σ observed in the fully hadronic analysis.

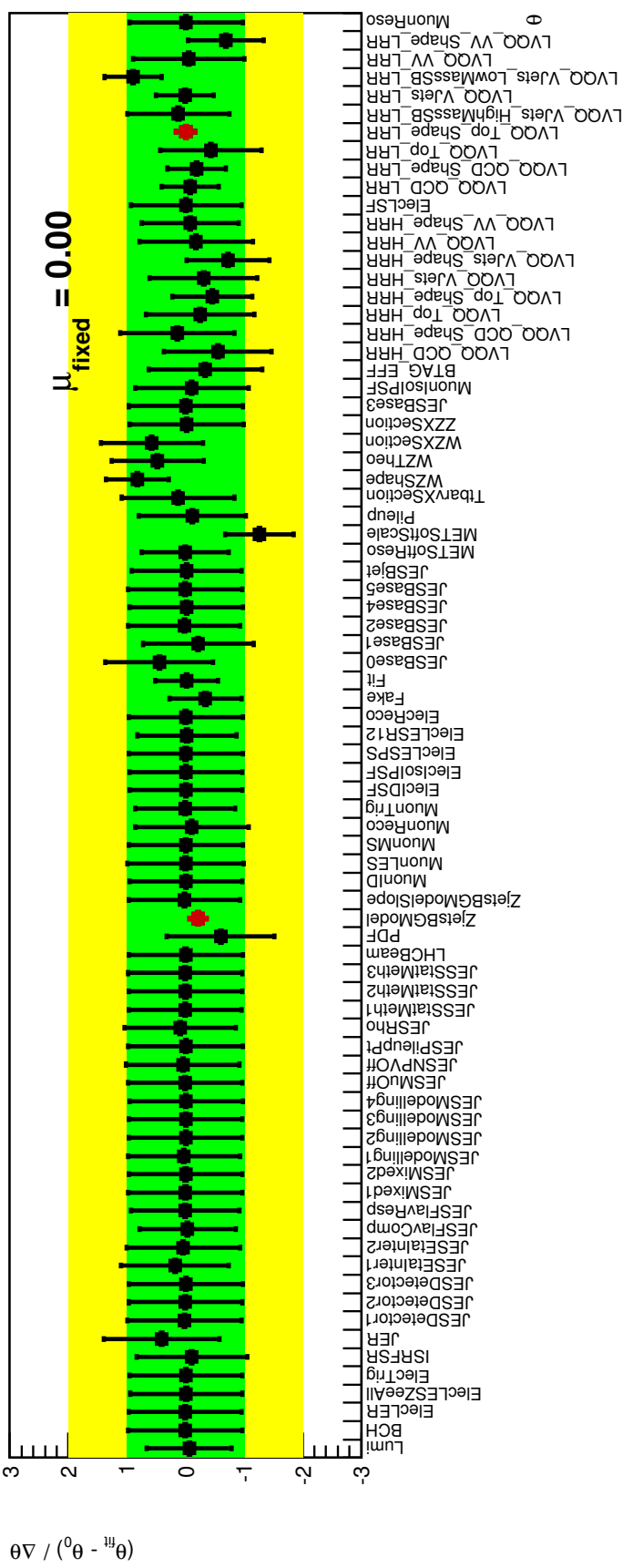

Figure 6.14: The pulls of the nuisance parameters derived from the conditional ML, fit simultaneously over the signal regions used to search for a 600 GeV W' boson.

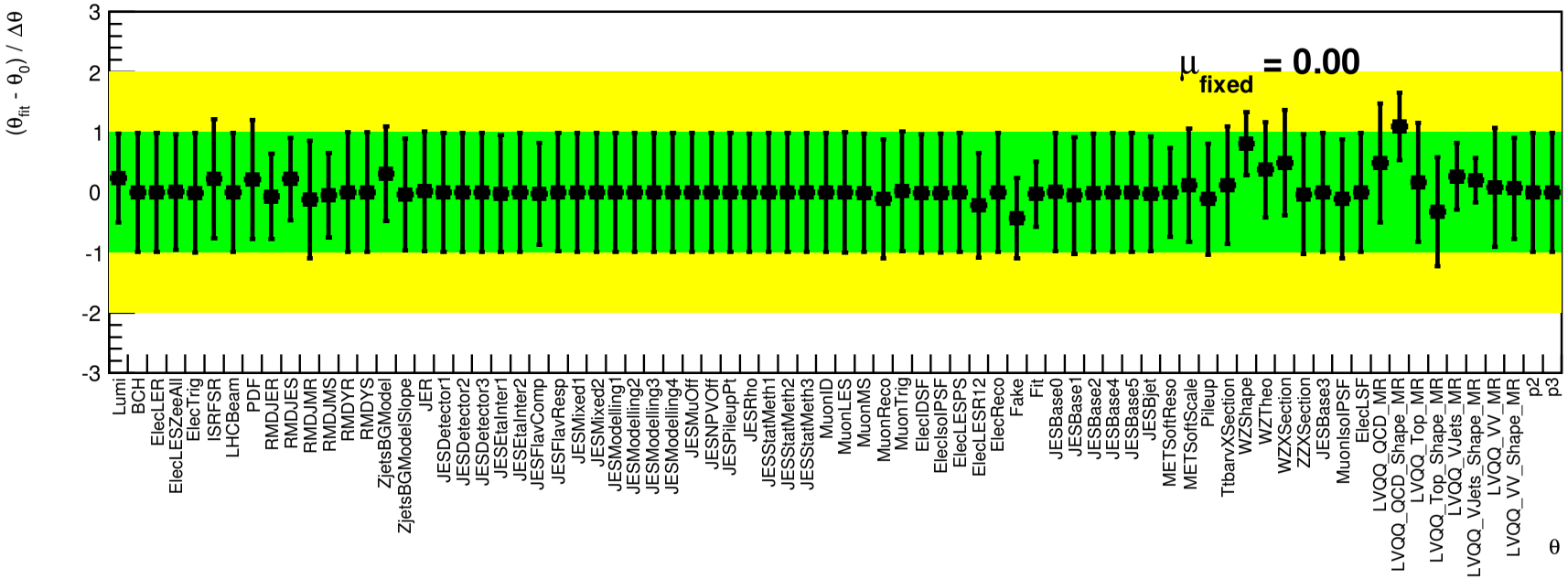

Figure 6.15: The pulls of the nuisance parameters derived from the conditional ML, fit simultaneously over the signal regions used to search for a 1200 GeV W' boson.

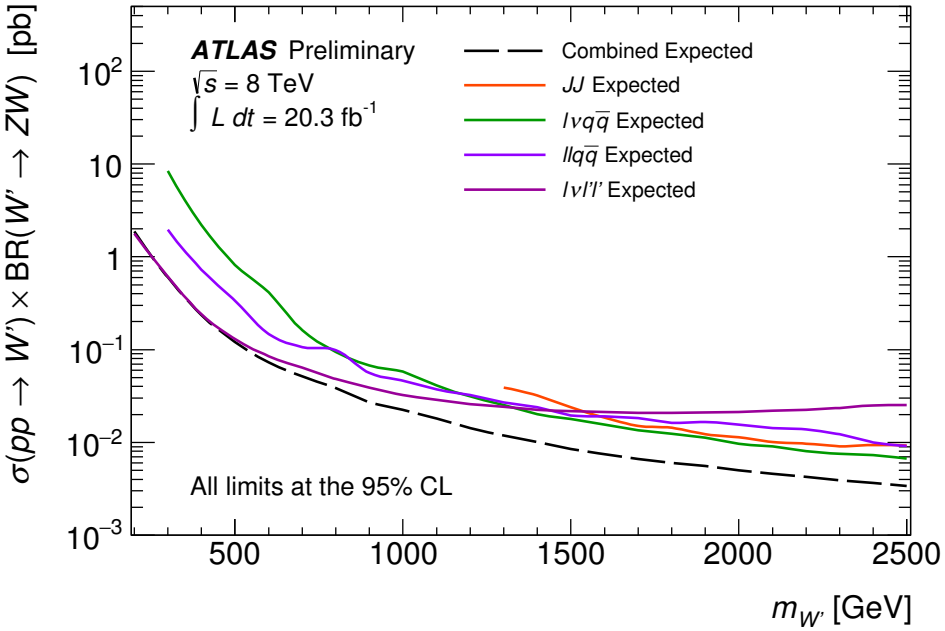

Figure 6.16: The expected 95% CL upper limit on the product of the production cross-section and branching ratio as a function of pole mass for the EGM W' boson for the $\ell\nu\ell'\ell'$, $\ell\ell qq$, $\ell\nu qq$, $qqqq$ channels individually and their combination.

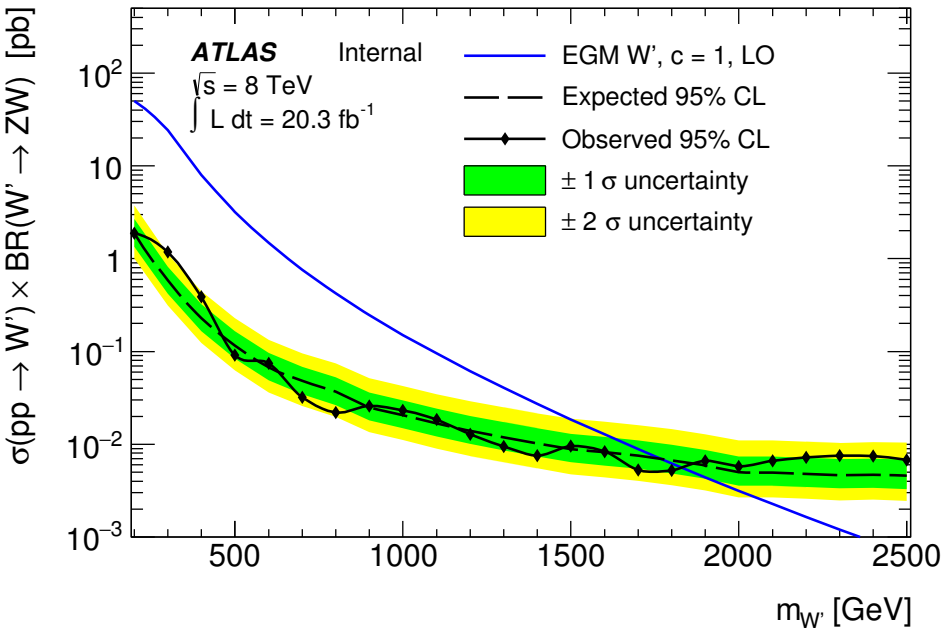

Figure 6.17: The expected and observed 95% CL upper limit on the product of the production cross-section and branching ratio as a function of pole mass for the EGM W' boson for the combination of the $\ell\nu\ell'\ell'$, $\ell\ell qq$ and $\ell\nu qq$ channels.

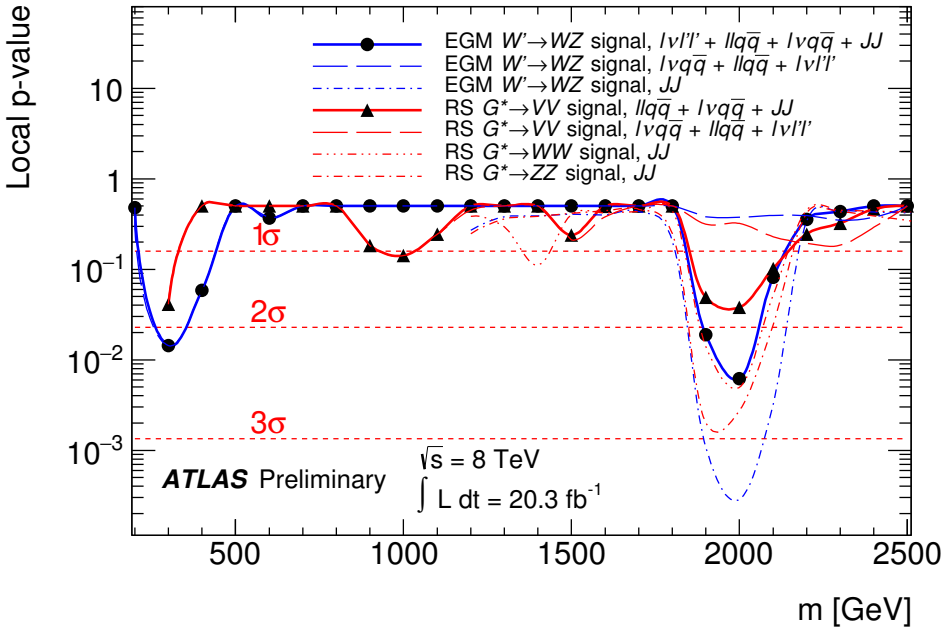

Figure 6.18: The local p-value calculated from the combination of the $\ell\nu\ell'\ell'$, $\ell\ell qq$, $\ell\nu qq$ and $qqqq$ channels for the bulk RS graviton and EGM W' boson signal models.

The limits set at the 95% CL for the combination of all four channels for the bulk RS graviton and the EGM W' boson are shown in figure 6.19. The EGM W' boson has expected and observed mass limits set at 1800 GeV and 1810 GeV, respectively, and the bulk RS graviton has expected and observed mass limits set at 790 GeV and 810 GeV respectively.

6.8.3 Leptonic and Hadronic Result Consistency

The likelihood distributions for each of the analyses are shown in figure 6.20. To quantify the consistency of the channels a new test statistic is defined. In this statistic the unconditional ML allows the signal strength to be different in each channel. The statistic is given as

$$\bar{q}_\mu = -2 \ln \bar{\lambda}(\mu), \tag{6.2}$$

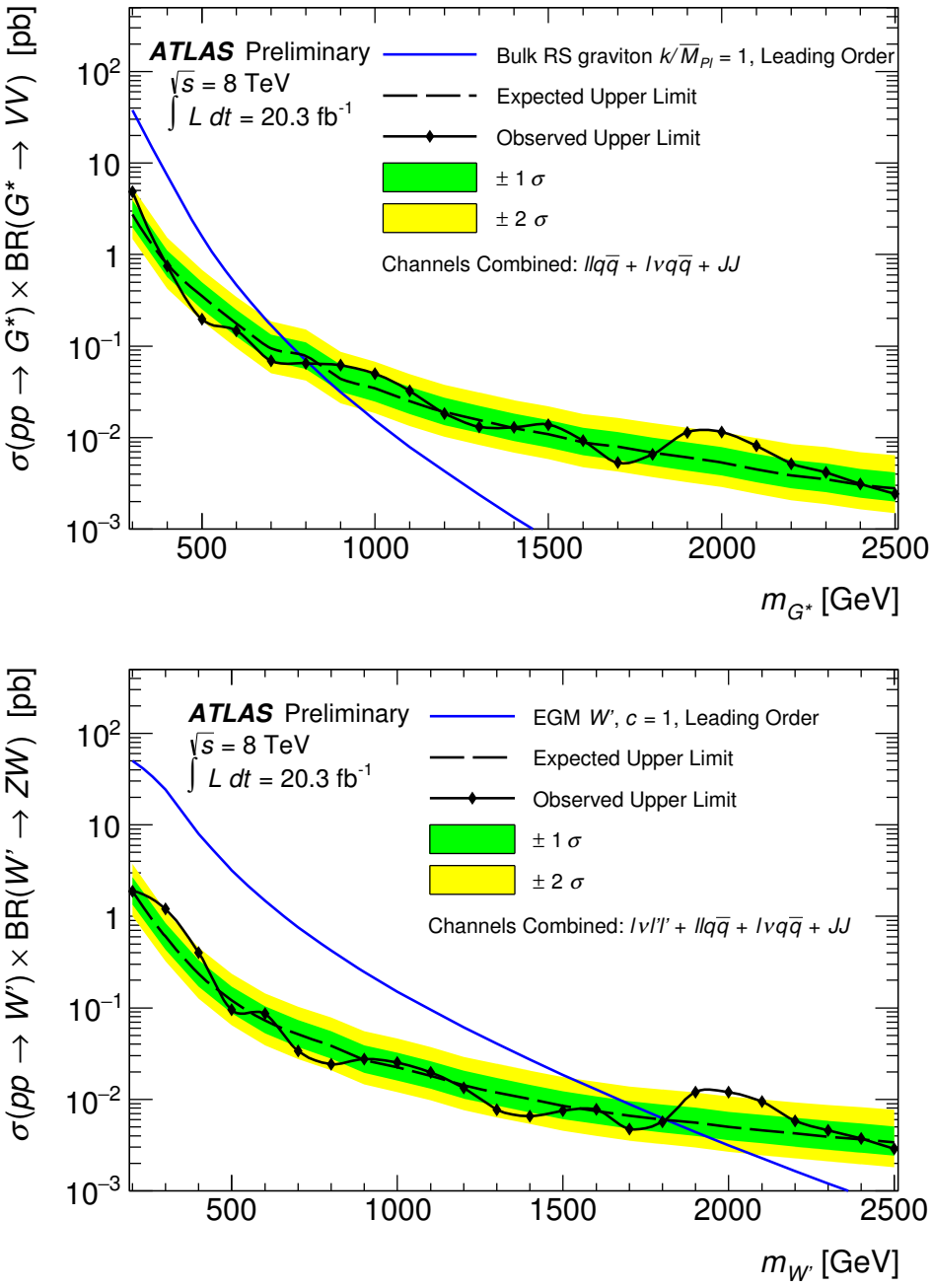

Figure 6.19: The expected and observed 95% CL upper limit on the product of the production cross-section and branching ratio as a function of pole mass for the bulk RS graviton signal (top) and EGM W' boson (bottom) for the combination of the $\ell\nu\ell'\ell'$, $\ell\ell qq$, $\ell\nu qq$ and $qqqq$ channels.

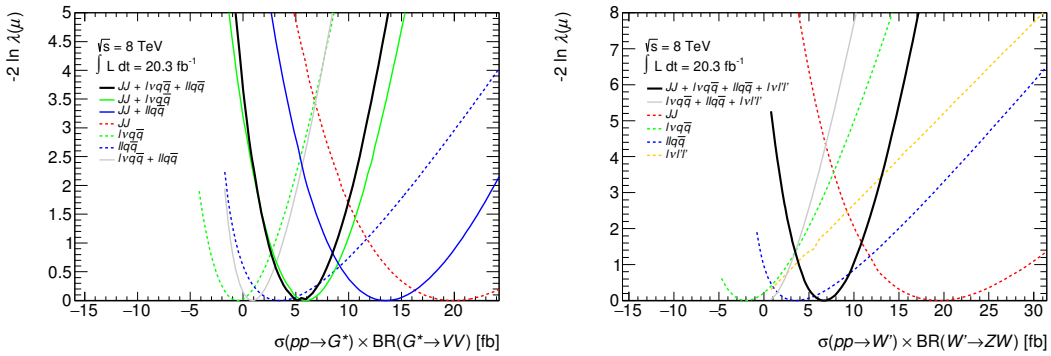

Figure 6.20: Comparison of the negative log likelihood curves for each of the component channels, the combination of the leptonic channels, and the full combination for a RS graviton (left) and EGM W' boson (right) with a mass of 2 TeV, as a function of signal cross-section.

where the likelihood ratio $\bar{\lambda}(\mu)$ is given by

$$\bar{\lambda}(\mu) = \frac{L\left(\mu, \hat{\hat{\theta}}(\mu)\right)}{L\left(\hat{\mu}, \hat{\theta}\right)}, \tag{6.3}$$

where $\hat{\mu}$ is the set of signal strengths which maximise the likelihood for multiple channels. If for two different channels i and j, $\theta_i \cap \theta_j = \emptyset$, then the channels can be considered independently and the likelihood can be decomposed into

$$\bar{\lambda}(\mu) \;=\; \prod_{i}^{\text{channels}} \frac{L\left(\mu, \hat{\hat{\theta}}_i(\mu)\right)}{L\left(\hat{\mu}_i, \hat{\theta}_i\right)}, \tag{6.4}$$

and so

$$\bar{\lambda}(\mu) = \prod_{i}^{\text{channels}} \lambda_i(\mu). \tag{6.5}$$

The test statistic can thus be rewritten as

$$\bar{q}_\mu = \sum_{i}^{\text{channels}} q_\mu^i. \tag{6.6}$$

In the case of this combination the sets of NP applicable to the leptonic

and hadronic channels, θ_{lep} and θ_{had} are not independent. However, it has been shown that there are no large pulls or correlations on the NP introduced due to the combination, so the form of $\bar{q}_\mu$ given in equation 6.6 is a good approximation.

The new test statistic is shown in figure 6.21 for a 2 TeV signal mass, where the signal strength has been scanned independently in the leptonic and hadronic channels. The contours shown in this plot are given for one degree of freedom, which means that they provide the correct coverage when a projection is taken, for instance along $\mu_{\text{lep}} = \mu_{\text{had}}$ which results in the combined likelihoods given in figure 6.20 with the addition of a constant; or along the red curve, which results in the likelihoods shown in figure 6.22.

The p-values for the hadronic and leptonic channels being consistent are 0.0047 and 0.0019 for the RS graviton and EGM W' boson respectively, as shown in figure 6.22. The hadronic channel, which observes an excess with a local p-value of 0.00029 for a 2 TeV W' boson is thus displaying a level of tension with the leptonic channels, though this tension is insufficient to indicate that a separate signal parameter is required to describe the leptonic and hadronic channels separately.

There are several theories beyond the SM that predict the existence of resonances at the TeV scale; however, these hypotheses cannot account for an excess in a single channel. The tension seen between the leptonic and hadronic channels thus suggests that the excess observed in the hadronic channel is due to a statistical fluctuation.

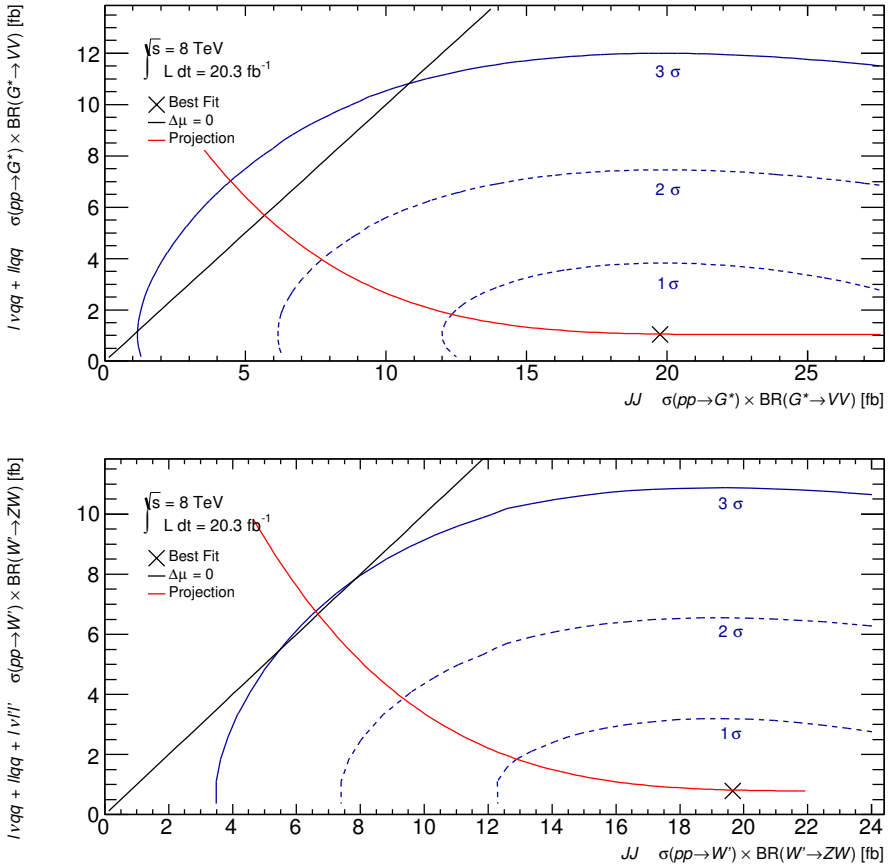

Figure 6.21: The signal cross-section is treated as uncorrelated between the hadronic channel and the leptonic channels. The two parameter negative log likelihood is shown for the RS graviton (top) and EGM W' boson (bottom) with mass 2 TeV. The blue ellipses denote the standard deviations of the likelihood.

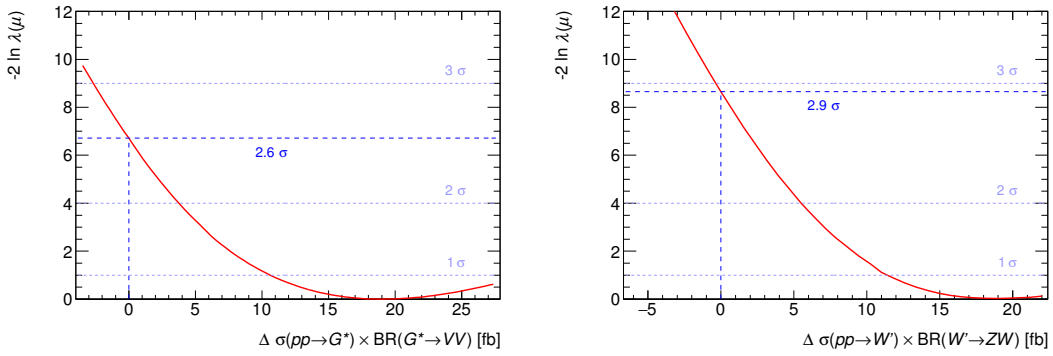

Figure 6.22: Projections of the two parameter negative log likelihoods shown in figure 6.21, taken along the red curves for a 2 TeV RS graviton (left) and EGM W' boson (right).

7

Conclusion

Several theories have been proposed to extend the Standard Model. Two such models, the bulk Randall-Sundrum (RS) model and the Extended Gauge Model (EGM), predict the production of narrow resonances with masses close to the TeV scale. In this thesis, searches for such exotic diboson resonances close to the TeV scale are performed, using the bulk RS graviton and the EGM W' boson as benchmark models. The dataset used has an integrated luminosity of 20.3 fb^{-1}, collected by the ATLAS detector in proton-proton collisions at a centre of mass energy of $\sqrt{s} = 8$ TeV.

New techniques for reconstructing the decay products of vector bosons in boosted topologies are applied. The reconstruction efficiency of leptonically decaying Z bosons with transverse momenta $p_T > 1$ TeV is significantly increased with the development of dilepton isolation criteria. Merged jets are used to reconstruct hadronically decaying vector bosons, increasing the acceptance significantly for bosons with $p_T > 250$ GeV.

A search is performed in the $\ell\ell qq$ final state. The results have been published in reference [2]. Backgrounds are modelled using MC techniques and control regions are used to constrain the dominant background prediction. The dominant uncertainties in this analysis are a result of this constraint. Profile likelihood

methods are employed to quantify the agreement of the data with the background prediction, and no significant excess is observed. Limits are set at the 95% CL on the product of cross-section and branching ratio for the production of the EGM W' boson (NNLO) and bulk RS graviton. Observed mass limits are extracted, excluding the W' boson and the graviton below a mass of 1590 GeV and 740 GeV, respectively.

In addition, a combination of the $\ell\nu\ell'\ell'$, $\ell\ell qq$, $\ell\nu qq$ and $qqqq$ final states is performed. Preliminary results of this combination have been published [3]. The combination of these channels leads to a significantly improved sensitivity as the individual channels are similarly sensitive to the benchmark models. The analyses are each statistically independent, and where systematic uncertainties affect multiple channels, the effects are correlated. The dominant systematic uncertainties affecting the combined sensitivity are those associated to the dominant background predictions in the $\ell\nu\ell'\ell'$ channel for low signal masses, and the $\ell\nu qq$ channel for high signal masses. The $qqqq$ analysis observes a 3.4 σ excess at a resonance mass of 2 TeV. No excess is observed in the one, two and three lepton analyses. The combination of the leptonic and semi-leptonic channels is performed, with no excess observed. The fully hadronic channel is shown to be consistent with the combination of the leptonic and semi-leptonic channels within 3 σ. The leptonic, semi-leptonic and fully hadronic channels are combined to set limits at the 95% CL on the product of the cross-section and branching ratio for the EGM W' boson (LO) and bulk RS graviton. Mass limits are extracted, excluding a W' boson below a mass of 1810 GeV and a graviton below a mass of 810 GeV.

The combination presented here concludes the searches for exotic diboson resonance performed in ATLAS with the Run 1 dataset. The sensitivity to these resonances can be expected to be increased with a combination of early Run 2 analyses due to the increased centre of mass energy of 13 TeV.

References

[1] ATLAS Collaboration, Search for resonant ZZ production in the $ZZ \leftarrow \ell\ell qq$ channel with the ATLAS detector using 7.2 fb^{-1} of $\sqrt{s} = 8$ TeV pp collision data, ATLAS-CONF-2012-150.

[2] The ATLAS Collaboration, Search for resonant diboson production in the $\ell\ell q\bar{q}$ final state in pp collisions at $\sqrt{s} = 8$ TeV with the ATLAS detector, Eur. Phys. J. C **75** (2015), arXiv:1409.6190.

[3] The ATLAS Collaboration, D. Adams *et al.*, Search for WW, WZ, and ZZ resonances in pp collisions at $\sqrt{s} = 8$ TeV with the ATLAS detector, (2015), ATLAS-CONF-2015-045.

[4] Particle Data Group, K. A. Olive *et al.*, Review of Particle Physics, 2014-2015, Chin. Phys. C **38**, 090001 (2014).

[5] M. E. Peskin and D. V. Schroeder, *An introduction to quantum field theory* (Westview Press Reading (Mass.), Boulder (Colo.), 1995).

[6] The ATLAS Collaboration, Status of the Standard Model at ATLAS, `https://atlas.web.cern.ch/Atlas/GROUPS/PHYSICS/CombinedSummaryPlots/SM/ATLAS_a_SMSummary_TotalXsect/history.html`.

[7] Planck, Planck 2015 results. I. Overview of products and scientific results, (2015), 1502.01582.

[8] L. Randall and R. Sundrum, A large mass hierachy from a small extra-dimension, Phys. Rev. Lett. **83**, 3370 (1999), arXiv:hep-ph/9905221.

[9] L. Randall and R. Sundrum, An alternative to compactification, Phys. Rev. Lett. **83**, 4690 (1999), arXiv:hep-th/9906064.

[10] K. Agashe, H. Davoudiasl, G. Perez, and A. Soni, Warped gravitons at the CERN LHC and beyond, Phys. Rev. D **76**, 036006 (2007), arXiv:hep-ph/0701186.

[11] H. Davoudiasl, J. Hewett, and T. Rizzo, Experimental probes of localized gravity: On and off the wall, Phys. Rev. D **63**, 075004 (2001), arXiv:hep-ph/0006041.

[12] A. V. Kisselev, Physical models within the framework of the Randall-Sundrum scenario, (2014), hep-th/1403.5469.

[13] G. Altarelli, B. Mel, and M. Ruiz-Altaba, Searching for new heavy vector bosons in $p\bar{p}$ colliders, Z. Phys. C **45**, 109 (1989).

[14] M. H. Seymour and M. Marx, Monte Carlo Event Generators, in *Proceedings, 69th Scottish Universities Summer School in Physics : LHC Phenomenology (SUSSP69)*, pp. 287–319, 2013, 1304.6677.

[15] S. Agostinelli *et al.*, Geant4—a simulation toolkit, Nuclear Instruments and Methods in Physics Research Section A: Accelerators, Spectrometers, Detectors and Associated Equipment **506**, 250 (2003).

[16] O. S. Brüning *et al.*, *LHC design report, Volume 1* (CERN, Geneva, 2004).

[17] O. S. Brüning *et al.*, *LHC design report, Volume 2* (CERN, Geneva, 2004).

[18] The CMS Collaboration, The CMS experiment at the CERN LHC, J. Instrum. **3**, S08004 (2008).

[19] The ALICE Collaboration, The ALICE experiment at the CERN LHC, J. Instrum. **3**, S08002 (2008).

[20] The LHCb Collaboration, The LHCb Detector at the LHC, J. Instrum. **3**, S08005 (2008).

[21] The ATLAS Collaboration, The timeline of the Large Hadron Collider, `http://timeline.web.cern.ch/timelines/The-Large-Hadron-Collider`.

[22] The ATLAS Collaboration, Letter of intent for the phase-II upgrade of the ATLAS experiment, (2012), CERN-LHCC-2012-022.

[23] The ATLAS Collaboration, Physics at a High-Luminosity LHC with ATLAS (Update), (2012), ATL-PHYS-PUB-2012-004.

[24] O. S. Brüning *et al.*, *LHC design report, Volume 3* (CERN, Geneva, 2004).

[25] E. J. N. Wilson, Fifty years of synchrotrons, Conf. Proc. **C960610**, 135 (1996), [,135(1996)].

[26] L. Evans and P. Bryant, LHC machine, J. Instrum. **3**, S08001 (2008).

[27] C. Lefvre, The CERN accelerator complex. Complexe des acclrateurs du CERN, (2008), CERN-DI-0812015.

[28] The ATLAS Collaboration, The ATLAS experiment at the CERN Large Hadron Collider, J. Instrum. **3**, S08003 (2008).

[29] The ATLAS Collaboration, *ATLAS detector and physics performance: Technical design report, 1* (CERN, Geneva, 1999).

[30] The ATLAS Collaboration, *ATLAS detector and physics performance: Technical design report, 2* (CERN, Geneva, 1999).

[31] The ATLAS Collaboration, Letter of intent for the phase-I upgrade of the ATLAS experiment, (2011), CERN-LHCC-2011-012.

[32] The ATLAS Collaboration, Vertex reconstruction performance of the ATLAS detector at $\sqrt{s} = 13$ TeV, (2015), ATL-PHYS-PUB-2015-026.

[33] V. Lacuesta, Track and vertex reconstruction in the ATLAS experiment, J. Instrum. **8**, C02035 (2013).

[34] F. Hugging, The ATLAS pixel detector, IEEE Trans. Nucl. Sci. **53**, 1732 (2006).

[35] R. Wigmans, *Calorimetry: Energy measurement in particle physics* (Clarendon Press, 2000).

[36] The ATLAS Collaboration, Atlas calorimeter photos, `http://www.atlas.ch/photos/calorimeters-combined-barrel.html`.

[37] The ATLAS Collaboration, *Expected performance of the ATLAS experiment: detector, trigger and physics* (CERN, Geneva, 2009), arXiv:0901.0512.

[38] A. L. Maslennikov, Test beam results of the ATLAS electromagnetic calorimeter prototype modules, Nucl. Instr. and Meth. Phys. Res. A **494**, 346 (2002).

[39] The ATLAS Collaboration, C. Meyer, The ATLAS tile calorimeter calibration and performance, EPJ Web Conf. **60**, 20051 (2013), ATL-TILECAL-PROC-2013-008, 1310.2945.

[40] The ATLAS Collaboration, T. Barillari, The ATLAS liquid argon hadronic end-cap calorimeter: construction and selected beam test results, Nuc. Phys. B - Proc. Suppl. **150**, 102 (2006), Proceedings of the 9th Topical Seminar on Innovative Particle and Radiation Detectors.

[41] The ATLAS Collaboration, D. Dannheim, Commissioning and performance of the ATLAS liquid argon calorimeters, ATL-LARG-PROC-2008-001.

[42] D. E. Groom, N. V. Mokhov, and S. I. Striganov, Muon stopping power and range tables 10-MeV to 100-TeV, Atom. Data Nucl. Data Tabl. **78**, 183 (2001).

[43] P. Jenni and M. Nessi, The ATLAS LUCID Collaboration, (2004), CERN-LHCC-2004-010. LHCC-I-014, revised version number 1 submitted on 2004-03-22 14:56:11.

[44] The ATLAS LUCID Collaboration, F. Lasagni Manghi, LUCID upgrade - ATLAS luminosity monitor for the 2015 LHC, Proc. Sci. **TIPP2014**, 317 (2014).

[45] The ATLAS Collaboration, A. Mapelli *et al.*, Development of a detector (ALFA) to measure the absolute LHC luminosity at ATLAS, (2007), ATL-LUM-PUB-2007-006.

[46] The ATLAS Collaboration, H. Stenzel, Luminosity calibration from elastic scattering, (2006), ATL-LUM-PUB-2007-001.

[47] W. Buttinger, The ATLAS level-1 trigger system, JPCS **396**, 012010 (2012).

[48] The ATLAS Collaboration, R. Spiwoks *et al.*, The ATLAS Level-1 Central Trigger Processor (CTP), (2005), ATL-DAQ-CONF-2005-030.

[49] C. Gabaldon, Performance of the ATLAS trigger system, J. Instrum. **7**, C01092 (2012), ATL-DAQ-PROC-2011-042.

[50] The ATLAS Collaboration, A. Dos Anjos, The DAQ/HLT system of the ATLAS experiment, (2009), ATL-DAQ-PROC-2009-006.

[51] The ATLAS Collaboration, Luminosity results, https://twiki.cern.ch/twiki/bin/view/AtlasPublic/LuminosityPublicResults.

[52] C. Kourkoumelis and S. Vourakis, HYPATIA—an online tool for ATLAS event visualization, Phys. Educ. **49**, 21 (2014).

[53] The ATLAS Collaboration, Performance of the ATLAS silicon pattern recognition algorithm in data and simulation at $\sqrt{s} = 7$ TeV, (2010), ATLAS-CONF-2010-072.

[54] The ATLAS Collaboration, Performance of primary vertex reconstruction in proton-proton collisions at $\sqrt{s}$ =7 TeV in the ATLAS experiment, (2010), ATLAS-CONF-2010-069.

[55] The ATLAS Collaboration, Performance of the ATLAS inner detector track and vertex reconstruction in the high pile-up LHC environment, (2012), ATLAS-CONF-2012-042.

[56] The ATLAS Collaboration, Electron and photon energy calibration with the ATLAS detector using LHC Run 1 data, Eur. Phys. J. C **74** (2014), CERN-PH-EP-2014-153, arXiv:1407.5063.

[57] The ATLAS Collaboration, Electron reconstruction and identification efficiency measurements with the ATLAS detector using the 2011 LHC protonproton collision data, Eur. Phys. J. C **74** (2014).

[58] The ATLAS Collaboration, Electron identification criteria, https://twiki.cern.ch/twiki/bin/viewauth/AtlasProtected/TechnicalitiesForMedium1.

[59] R. Nicolaidou *et al.*, Muon identification procedure for the ATLAS detector at the LHC using Muonboy reconstruction package and tests of its performance using cosmic rays and single beam data, JPCS **219**, 032052 (2010).

[60] The ATLAS Collaboration, Staco muon quality definition, https://twiki.cern.ch/twiki/bin/viewauth/AtlasProtected/QualityDefinitionStaco.

[61] The ATLAS Collaboration, W. Lampl *et al.*, Calorimeter clustering algorithms: Description and performance, (2008), ATL-LARG-PUB-2008-002. ATL-COM-LARG-2008-003.

[62] M. Cacciari, G. P. Salam, and G. Soyez, The anti-k_t jet clustering algorithm, J. High Energy Phys. **2008**, 063 (2008), arXiv:0802.1189.

[63] Y. L. Dokshitzer, G. D. Leder, S. Moretti, and B. R. Webber, Better jet clustering algorithms, J. High Energy Phys. **08**, 001 (1997), CAVENDISH-HEP-97-06, hep-ph/9707323.

[64] S. D. Ellis and D. E. Soper, Successive combination jet algorithm for hadron collisions, Phys. Rev. D **48**, 3160 (1993), CERN-TH-6860-93, hep-ph/9305266.

[65] The ATLAS Collaboration, D. L. Adams *et al.*, High-pT boson jet tagging with the ATLAS detector, (2013), ATL-COM-PHYS-2013-899.

[66] The ATLAS Collaboration, Missing E_T utility, `https://twiki.cern.ch/twiki/bin/viewauth/AtlasProtected/MissingETUtility`.

[67] The ATLAS Collaboration, Missing E_T calibration, `https://twiki.cern.ch/twiki/bin/view/AtlasProtected/EtMissRefFinal`.

[68] D0, Search for a resonance decaying into WZ boson pairs in $p\bar{p}$ collisions, Phys. Rev. Lett. **104**, 061801 (2010), FERMILAB-PUB-09-609-E, 0912.0715.

[69] D0, Search for resonant WW and WZ production in $p\bar{p}$ collisions at $\sqrt{s} =$ 1.96 TeV, Phys. Rev. Lett. **107**, 011801 (2011), FERMILAB-PUB-10-485-E, 1011.6278.

[70] CDF, Search for high-mass resonances decaying into ZZ in $p\bar{p}$ collisions at $\sqrt{s} = 1.96$ TeV, Phys. Rev. D **85**, 012008 (2012), FERMILAB-PUB-11-613-E, CDF-PUB-EXOTICS-PUBLIC-10603, 1111.3432.

[71] The ATLAS Collaboration, Search for WZ resonances in the fully leptonic channel using pp collisions at with the ATLAS detector, Phys. Lett. B **737**, 223 (2014), CERN-PH-EP-2014-094, arXiv:1406.4456.

[72] The CMS Collaboration, Search for new resonances decaying via WZ to leptons in proton-proton collisions at $\sqrt{s} = 8$ TeV, Phys. Lett. B **740**, 83 (2015), arXiv:1407.3476.

[73] The ATLAS Collaboration, Search for production of WW/WZ resonances decaying to a lepton, neutrino and jets in pp collisions at $\sqrt{s} = 8$ TeV with the ATLAS detector, Eur. Phys. J. C **75** (2015), arXiv:1503.04677.

[74] The ATLAS Collaboration, Search for high-mass diboson resonances with boson-tagged jets in protonproton collisions at $\sqrt{s} = 8$ TeV with the ATLAS detector, (2015), arXiv:1506.00962.

[75] The CMS Collaboration, Search for massive resonances in dijet systems containing jets tagged as W or Z boson decays in pp collisions at $\sqrt{s} = 8$ TeV, J. High Energy Phys. **2014** (2014), arXiv:1405.1994.

[76] The ATLAS Collaboration, Preliminary results on the muon reconstruction efficiency, momentum resolution, and momentum scale in ATLAS 2012 pp collision data, (2013), ATLAS-CONF-2013-088, ATLAS-COM-CONF-2013-096.

[77] The ATLAS Collaboration, Muon calorimeter corrections, `https://twiki.cern.ch/twiki/bin/viewauth/AtlasProtected/MuonCalorimeterCorrections`.

[78] The ATLAS Collaboration, Jet energy scale and its systematic uncertainty for jets produced in proton-proton collisions at $\sqrt{s} = 7$ TeV and measured with the ATLAS detector, (2010), ATLAS-CONF-2010-056.

[79] The ATLAS Collaboration, Jet energy resolution in proton-proton collisions at $\sqrt{s} = 7$ TeV recorded in 2010 with the ATLAS detector, Eur. Phys. J. **C73**, 2306 (2013), CERN-PH-EP-2012-191, 1210.6210.

[80] The ATLAS Collaboration, Jet cleaning, `https://twiki.cern.ch/twiki/bin/view/Sandbox/EgammaPhysCalib`.

[81] A. Belyaev, N. D. Christensen, and A. Pukhov, CalcHEP 3.4 for collider physics within and beyond the Standard Model, Comput. Phys. Commun. **184**, 1729 (2013), PITT-PACC-1209, 1207.6082.

[82] T. Sjstrand *et al.*, An Introduction to PYTHIA 8.2, Comput. Phys. Commun. **191**, 159 (2015), LU-TP-14-36, MCNET-14-22, CERN-PH-TH-2014-190, FERMILAB-PUB-14-316-CD, DESY-14-178, SLAC-PUB-16122, 1410.3012.

[83] The ATLAS Collaboration, D. L. Adams *et al.*, Search for new heavy gauge bosons in the charged lepton plus missing transverse energy final state using pp collisions at $\sqrt{s} = 8$ TeV in the ATLAS detector, (2012), ATL-COM-PHYS-2012-1771.

[84] T. Gleisberg *et al.*, Event generation with SHERPA 1.1, JHEP **02**, 007 (2009), FERMILAB-PUB-08-477-T, SLAC-PUB-13420, ZU-TH-17-08, DCPT-08-138, IPPP-08-69, EDINBURGH-2008-30, MCNET-08-14, 0811.4622.

[85] S. Frixione, F. Stoeckli, P. Torrielli, B. R. Webber, and C. D. White, The MCaNLO 4.0 Event Generator, (2010), CAVENDISH-HEP-10-12, CERN-TH-2010-216, IPPP-10-62, DCPT-10-124, 1010.0819.

[86] G. Corcella *et al.*, HERWIG 6: An Event generator for hadron emission reactions with interfering gluons (including supersymmetric processes), JHEP **01**, 010 (2001), CAVENDISH-HEP-99-03, CERN-TH-2000-284, RAL-TR-2000-048, 0011363.

[87] J. M. Butterworth, J. R. Forshaw, and M. H. Seymour, Multiparton interactions in photoproduction at HERA, Z. Phys. **C72**, 637 (1996), CERN-TH-96-82, M-C-TH-96-05, UCL-HEP-96-02, 9601371.

[88] B. P. Kersevan and E. Richter-Was, The Monte Carlo event generator AcerMC versions 2.0 to 3.8 with interfaces to PYTHIA 6.4, HERWIG 6.5 and ARIADNE 4.1, Comput. Phys. Commun. **184**, 919 (2013), TPJU-6-2004, 0405247.

[89] M. Aliev *et al.*, HATHOR - HAdronic Top and Heavy quarks crOss section calculatoR, Comput. Phys. Commun. **182**, 1034 (2011), arXiv:1007.1327.

[90] The ATLAS Collaboration, Muon trigger correction factors, `https://twiki.cern.ch/twiki/bin/viewauth/Atlas/MuonTriggerPhysicsTriggerRecommendations`.

[91] The ATLAS Collaboration, Muon reconstruction efficiency in reprocessed 2010 LHC proton-proton collision data recorded with the ATLAS detector, (2011), ATLAS-CONF-2011-063.

[92] The ATLAS Collaboration, Jet uncertainty recomendations 2012, `https://twiki.cern.ch/twiki/bin/view/AtlasProtected/JetUncertainties2012`.

[93] The ATLAS Collaboration, W. Lukas, Fast Simulation for ATLAS: Atlfast-II and ISF, Journal of Physics: Conference Series **396**, 022031 (2012).

[94] G. Romeo, A. Schwartzman, R. Piegaia, T. Carli, and R. Teuscher, Jet energy resolution from in-situ techniques with the ATLAS detector using proton-proton collisions at a center of mass energy $\sqrt{s} = 7$ TeV, (2011), ATL-COM-PHYS-2011-240.

[95] The ATLAS Collaboration, Jet substructure recommendations, `https://twiki.cern.ch/twiki/bin/viewauth/AtlasProtected/JetSubstructureRecommendations`.

[96] The ATLAS Collaboration, BCH cleaning tool, `https://twiki.cern.ch/twiki/bin/view/AtlasProtected/BCHCleaningTool`.

[97] J. Wenninger, Energy calibration of the LHC beams at 4 TeV, (2013), CERN-ATS-2013-040.

[98] L. Moneta *et al.*, The RooStats Project, Proc. Sci. **ACAT2010**, 057 (2010), 1009.1003.

[99] J. S. Conway, Incorporating nuisance parameters in likelihoods for multi-source spectra, (2011), arXiv:1103.0354.

[100] W. Verkerke, Guide to parameterized likelihood analyses, `https://twiki.cern.ch/twiki/pub/AtlasProtected/ATLASStatisticsFAQ/pllguide_draft.pdf`, 2012.

[101] ROOT Collaboration, K. Cranmer, G. Lewis, L. Moneta, A. Shibata, and W. Verkerke, HistFactory: A tool for creating statistical models for use with RooFit and RooStats, (2012), CERN-OPEN-2012-016.

[102] F. James, MINUIT reference manual, CERN Program Library Long Writup **D506**.

[103] G. Cowan, K. Cranmer, E. Gross, and O. Vitells, Asymptotic formulae for likelihood-based test of new physics, Eur. Phys. J. C **71** (2011), arXiv:1007.1727.

[104] B. Roe, *Probability and Statistics in Experimental Physics*Undergraduate Texts in Contemporary Physics (Springer New York, 2001).

[105] The ATLAS Collaboration, Search for new particles decaying to ZZ using final states with leptons and jets with the ATLAS detector in $\sqrt{s} = 7$ TeV proton-proton collisions, Phys. Lett. B **712**, 331 (2012), CERN-PH-EP-2012-026, 1203.0718.

[106] The ATLAS Collaboration, Search for new phenomena in the WW to $\ell\nu\ell'\nu'$ final state in pp collisions at $\sqrt{s} = 7$ TeV with the ATLAS detector, Phys. Lett. B **718**, 860 (2013), CERN-PH-EP-2012-197, 1208.2880.

[107] ATLAS, Search for resonant WZ production in the $WZ \to \ell\nu\ell'\ell'$ channel in $\sqrt{s} = 7$ TeV pp collisions with the ATLAS detector, Phys. Rev. D **85**, 112012 (2012), CERN-PH-EP-2012-063, 1204.1648.

[108] The ATLAS Collaboration, Search for resonant diboson production in the $WW/WZ \to \ell\nu jj$ decay channels with the ATLAS detector at $\sqrt{s} = 7$ TeV, Phys. Rev. D **87**, 112006 (2013), CERN-PH-EP-2012-296, 1305.0125.